MULTI-SCALE AND MULTI-APPROCH INVESTIGATIONS OF PETROPHYSICAL PROPERTIES AND FLUID FLOW IN NATURAL ROCKS

By

Qiming Wang

DISSERTATION

Submitted in partial fulfillment of the requirements

for the degree of Doctor of Philosophy at

The University of Texas at Arlington

May 2022

Arlington, Texas

Supervising Committee:

Dr. Qinhong Hu, Supervising Professor

Dr. John S Wickham

Dr. Majie Fan

Dr. Jiechao Jiang

Dr. Xinbao Yu

Abstract

Multi-scale and multi-approach investigations of petrophysical properties and fluid flow in natural rocks

Qiming Wang, Ph.D.

The University of Texas at Arlington. 2022

Supervising Professor: Qinhong Hu

Natural rock is one of the most important geological attributes on the Earth that have been widely related to human daily life in various aspects. Rocks are usually utilized with respect to their petrophysical properties and performance within the context of building & construction, petroleum recovery, carbon sequestration, geothermal energy utilization, nuclear waste storage and repositories, and contamination remediation.

Contrary to the well-studied rocks such as sandstone and carbonate rocks, the fluid storage and migration in the tight rock (e.g., shale matrix) is more complex and still poorly understood. Due to the low porosity, extremely low permeability, complex mineral composition, and high degree of spatial heterogeneity of petrophysical properties, the study of shale has been recently attracting an increasing attention. Some studies point out that the fluid flow in shale is strongly restricted by their microfracture-pore structure, spatial heterogeneity of pore structure, and wettability. Limited by the research methodologies, most of previous studies of microfracture-pore structure and fluid flow only focus on one aspect with rare studies of integrated analyses. Furthermore, due to the size limitation of samples that can be analyzed in the laboratory, traditional characterization methods for pore structure and mineral composition are restricted to using μm to centimeter-sized samples at the cost of spatial heterogeneity, and versatile

methodologies that can interrogate larger-sized samples are urgently needed for fundamental understanding of the scaling effect of petrophysical properties, such as sample size-dependent effective porosity. Therefore, it is necessary to employ multiple and complementary approaches to investigate the microfracture-pore system at multiple sample scales, and use the test results and observations to provide more information for the study of fluid flow in natural rocks both spatially and temporally.

This dissertation is comprised of five chapters: the first one serves as a brief introduction about the following three chapters, the second chapter is a published paper, the third chapter a manuscript under review, the fourth chapter as a peer-reviewable manuscript for a possible publication, and the last chapter presents the conclusions.

ACKNOLEDGMENTS

Since I joined the UTA in 2017, I received a tremendous help and encouragement for my research works and daily life. It is a genuine pleasure to express my deep sense of thanks and gratitude to those people.

I would like to thank my advisor Dr. Qinhong Hu for his constant and patient guidance, support, and encouragement in both my Master and Ph.D. programs. During the past five years, I've learned professional skills from him, in addition to being motivated and inspired by his working ethics. Thanks to him, I was able to finish my Ph.D. successfully.

Thanks also go to Drs. John Wickham, Majie Fan, Jiechao Jiang, Xinbao Yu, Merlynd Nestell, Heyong-Moo Shin, Arne Winguth, and Cornelia Winguth at UTA for their teaching and helps in my research. Special thanks to Dr. Jan Ilvasky at ANL, Dr. Markus Bleuel at NIST, and Dr. Wei-Ren Chen at ORNL for their help and support in X-ray and neutron scattering work.

I am also grateful to the following friends and colleagues: Dr. Yi Shu, Dr. Xiaoming Zhang, Dr. Xiang Lin, Dr. Yang Wang, Prince Oware, Tristan Tom, Dr. Yuxiang Zhang, Hepeng Tian, Dr. MD Golam Kibria, Dr. Nyujia Peng, Dr. Zeynep Doner, Dr. Puloma Chakrbarty, Nabil Mzee, Ashley Chang, Christina Muñoz, Chad Larson, Ryan Jones, Samuel Beaker, A.K. Gan, Xiaoqing Yuan, Xuewei Ning, Gang Lei, Tao Zhang, Hasnian Iltaf, Xiaoguang Yang, Jingyi Wang, Longhui Bai, Xianglong Fang, and Ogo Azike. It was great studying and working with all of them. Happy lab time!

Lastly, I wish to express my thank to Chen Zhao, Dexi Wang, Jinfeng Zhang, and my other family members for their constant love, support, and encouragements.

Dedication

To Dr. Hu

To Chen Zhao

To my parents and other family members

Table of Contents

List of Tables

Chapter II

Chapter III

Chapter IV

List of Figures

Chapter II

Chapter III

Chapter IV

CHAPETER I

INTRODUCTION

This research presents muti-scale and multi-approach investigation of petrophysical properties and fluid flow behaviors in natural rocks. The rock samples such as sandstone, carbonate rocks, and shale were collected from both outcrop and wells across Texas and Oklahoma, USA. The research of pore structure is presented in Chapter II, the spatial heterogeneity is presented in Chapter III, and the fluid flow is presented in Chapter IV.

Chapter II includes a study of mineral compositions, sedimentary textures, pore structure, and water-rock interactions of eight Eagle Ford Formation core plugs from three counties across Texas. Laboratory-based techniques such as X-ray diffraction (XRD), total organic carbon (TOC), pyrolysis, petrographic microscopy, scanning electron microscopy (SEM), mercury intrusion porosimetry (MIP), nitrogen physisorption (NP), water vapor sorption (WVS), and spontaneous imbibition (SI) were used in this study.

Chapter III studies the mineral composition and pore structure heterogeneity on dm-sized Eagle Ford Shale. The 4-inch (10.2 cm) outcrop core sample were scanned by micro-X-ray fluorescence (μ-XRF) and small angle X-ray scattering to study the heterogeneity of elemental distribution, sedimentary textures, pore structure, and mineral types at dm-scales. Several subsamples were cut from the large samples to investigate the heterogeneity of mineral compositions, organic matter, and maturity at cm to mm scales.

Chapter IV covers fluid flow behaviors in sandstone, carbonate rocks, and shale. Both spontaneous imbibition and vapor sorption of water were used to determine the water flow behavior in these porous rocks. Combined with pore structure, wettability, and mineral compositions, the influencing factors on water fluid behavior were discussed.

CHAPTER II

Microfracture-pore structure characterization and water-rock interaction in three lithofacies of the Lower Eagle Ford Formation

Qiming Wang[a], Qinhong Hu[a*], Chad Larsen[a], Chen Zhao[a], Mengdi Sun[b], Yuxiang Zhang[a], and Tao Zhang[c]

[a] Department of Earth and Environmental Sciences, the University of Texas at Arlington, TX 76019, USA

[b] Key Laboratory of Tectonics and Petroleum Resources, Ministry of Education, China University of Geosciences, Wuhan, 430074, China

[c] Shandong Provincial Key Laboratory of Deep Oil and Gas, China University of Petroleum (East China), Qingdao, 266580, China.

Engineering Geology

Corresponding author: maxhu@uta.edu

Keywords: microfractures, pore structure, fluid flow pathways, water vapor physisorption, Eagle Ford formation

Abstract

The microfracture-pore structures and water-rock interactions of eight samples of three typical lithofacies (three limestone, three wackestone, and two mudstone) from the Lower Eagle Ford Formation have been investigated using an integrated methodology. The methods used were X-ray diffraction (XRD), total organic carbon (TOC) content, pyrolysis, thin-section petrography, scanning electron microscopy (SEM), mercury intrusion porosimetry (MIP), spontaneous water imbibition, and water vapor & nitrogen physisorption. Petrophysical properties such as organic richness, maturity, mineral composition, types and patterns of microfractures and pores, porosity, pore-throat size distribution, pore size distribution, pore connectivity, water adsorption and desorption behavior were determined from these methods, and the results compared among the three lithofacies. For example, the three limestone EAS samples and three wackestone DM samples show a low porosity range from 2.02-3.35%, whereas the two mudstone VRU samples exhibit a much large average porosity of 11.7% by MIP results. Nitrogen physisorption results show that pore size distributions have a good similarity in N_2 adsorption volume for the samples with similar lithology. Microfractures are morphologically divided into seven types, with their definitions & pictorial examples presented and possible formation mechanisms proposed. In addition, the water vapor physisorption behavior and their controlling factors are discussed. The water adsorption capacity shows a positive relationship (R^2=0.90) with clay content and a negative relationship (R^2=0.99) with carbonate content. In general, this integrated study of microfracture-pore structure characterization and water-rock interaction provides some insights of water vapor adsorption behavior in different lithofacies and whether microfractures could be an important pathway for fluid flow.

1. Introduction

Understanding water-rock interactions in porous geological materials is important in various engineering and energy geology fields, such as fluid flow studies in geothermal energy utilization, shale petroleum recovery, nuclear waste disposal, and evaluation of physical properties and performance of construction materials (Hudec, 1989; Shang et al., 1995; Hu et al., 2001; Pavlík et al., 2012; Keppert et al., 2016; Tang et al., 2017; Wang et al., 2019; Sun et al., 2020; Yang et al., 2020). Water vapor has been recognized as the dominant aqueous phase in some geothermal reservoirs (White, 1970; Shang et al., 1995; Gruszkiewicz et al., 2001). Water adsorption studies attracted more attention after the BET model (Brunauer, Emmet, and Teller; Brunauer et al., 1938) was successfully applied to the characterization of rock properties (Hsieh, 1980; Hsieh and Ramey, 1983). An understanding of the properties and water-rock interactions of geological materials has been improved by the development of analytical methods in other scientific fields such as scanning electron microscopy, water vapor physisorption, and spontaneous imbibition, which have then been effectively utilized in engineering geosciences (Hu, 2020).

The Eagle Ford Formation is currently a target of petroleum production (U.S. Energy Information Administration, 2014), but it is less well known as one of the formations that the tunnel for the Superconducting Super Collider penetrated (Duan and Mrugala, 1993; Hsu and Nelson, 2002). This formation is interbedded with thick layers of mudstone & marl and thin layers of brittle limestone (Frebourg et al., 2016; Lehrmann et al., 2019). It has been widely reported that the change of engineering property of clayey rock formation is sensitive to water, which could often lead to rock failures (Hsu and Nelson, 2002; Youn and Tonon, 2010; Lyu et al., 2018; Liu and Sheng, 2019; Liu et al., 2020) and serious civil engineering problems such as landslide, slope failure, and shale embankment failures (Bryson et al., 2012; Gu and Huang,

2016; Khan et al., 2017). The engineering and geological properties of rock such as pore structure, mineral composition, water saturation and retention characteristics control the water-rock interaction (e.g., freeze-thaw, weathering, and deterioration processes) (Bednarik et al., 2014; Kock et al., 2017; Liu et al., 2020).

In previous research, pore structure characterization and water-rock interaction studies have focused on the shale & marl layers (Mullen, 2010; Morsy et al., 2014; Ko et al., 2017), while the interbed limestones have attracted much less attention (Jiang and Mokhtari, 2019). Moreover, the differences in pore structures, water flow properties, and water vapor physisorption among these three lithofacies of limestone, wackestone, and mudstone are still not clear. Water-rock interaction consists of two major processes in rocks, namely fluid flow in the pore-microfracture system and water vapor physisorption in the rock matrix (Hu et al., 2001; Gensterblum et al., 2015; Keppert et al., 2016; Wang et al., 2021a). Microfractures are defined as cracks occur in the rock matrix ranging up to several mm in length and several μm in width. They attract more attention as a type of pore space due to their relatively large scale in length and various mechanisms of formation. Previous publications have characterized and interpreted microfractures in different ways (Zeng et al., 2010; Anders et al., 2014; Gale et al., 2014; Loucks and Reed, 2016; Hooker et al., 2018; Zhou et al., 2018). For example, Zeng et al. (2010) classified microfractures in sandstones as tectonic-, overpressure-, and diagenetic-related types. Zhou et al. (2018) concluded that microfracture types in carbonate rocks include tectonic fracture, grain breakage fractures, microstylolites, and micro-corrosion fractures. Loucks and Reed (2016) pointed out that desiccation microfractures and devolatilization microfractures usually occur in mudstone (shale). In addition, some post-coring artificial microfractures often occur in clay-rich samples. These literature studies and interpretation of microfractures are

reasonable and provide valuable information. However, their interpretations are usually based on some vague definitions without pictorial description. As a result, biased or incorrect interpretations may occur, caused by the misunderstanding of the definitions.

Microfractures are often interpreted as providing preferential pathways for fluid flow (Capuano, 1994; Apaydin et al., 2012; Zhou et al., 2018). One issue in previous microfracture studies is uncertainty over whether the microfractures are interconnected over a large rock volume, and hence if they have the ability to provide accessible pathways for macro-scale fluid flow (Loucks and Reed, 2016; Sun et al., 2013). Furthermore, how the rock matrix transports and stores water vapor influences the permeability and strength of the rock formation (Zhang et al., 2012; 2014; Keppert et al., 2016; Li et al., 2016). The water vapor physisorption of mudstone and other clay-rich geological materials has been reported (Zolfaghari et al., 2017a-b; Tang et al., 2017; Lin et al., 2020; Yang et al., 2020), but carbonate-rich rocks have attracted less attention. As a result, the water vapor physisorption behavior of carbonate-rich rocks, and the controlling factors, still unclear.

In this study, we used integrated analyses of pore and microfracture structures method such as petrography thin section, Scanning electron microscopy (SEM), mercury intrusion porosimetry (MIP), and nitrogen physisorption (NP), water-rock interaction studies by water vapor physisorption (WVP) and spontaneous imbibition (SI) of water for three limestones, three wackestone, and two mudstones from the lower Eagle Ford formation in Texas. Morphology description, interpretation, and classification of microfractures are presented based on image analyses using petrographic microscopy and SEM. Basic information such as mineral composition, organic richness, and maturity were determined by X-ray diffraction (XRD), total organic carbon content (TOC), and pyrolysis. By integrating the petrographic and petrophysical

results, the influence of microfractures on fluid flow is discussed, and the impact of between pore structure and mineral composition on water vapor adsorption ability in these three different lithofacies is also assessed. The results and findings in this study could provide valuable information (such as pore and microfracture structures, and water-rock interaction) for both geologists and engineers working on the Lower Eagle Ford Formation, either for petroleum production or the construction of underground facilities.

2. Samples and Methods

2.1 Sample selection and preparation

Eight core plugs were selected from three well locations in the Lower Eagle Ford Formation, south Texas. Three limestone samples were collected from the EAS well in Gonzales County, three wackestone were selected from the DM well in McMullen county, and two mudstones from the VRU well in Brazos county (Fig. 1). Samples with dimensions of 1 cm^3 and 5 mm × 1 cm^2 were cut from standard cylindrical core plugs for MIP, SI, and SEM tests. Due to the limited core sample mass and poor sample integrity, 1 cm^3 cubes were sometimes not available for the MIP and SI tests of water. When they are not available, the 5 mm × 1 cm^2 samples are used instead. A rock fragment was used to prepare petrographic thin sections for optical microscopy, and the remaining material was crushed to granular sizes at 20-35 mesh for nitrogen and water vapor physisorption, as well as powders (<200 mesh) for the XRD, TOC, and pyrolysis tests.

2.2 XRD, TOC, and pyrolysis analyses

Mineral composition, organic richness, and maturity were determined by XRD, TOC, and pyrolysis methods, respectively. Mineral composition analysis was carried out on Shimadzu

MaximaX XRD-7000. In the X-ray diffractometer, the 2θ was determined at the range of 2 to 70 degrees with a radiation rate of 6 revolutions per minute.

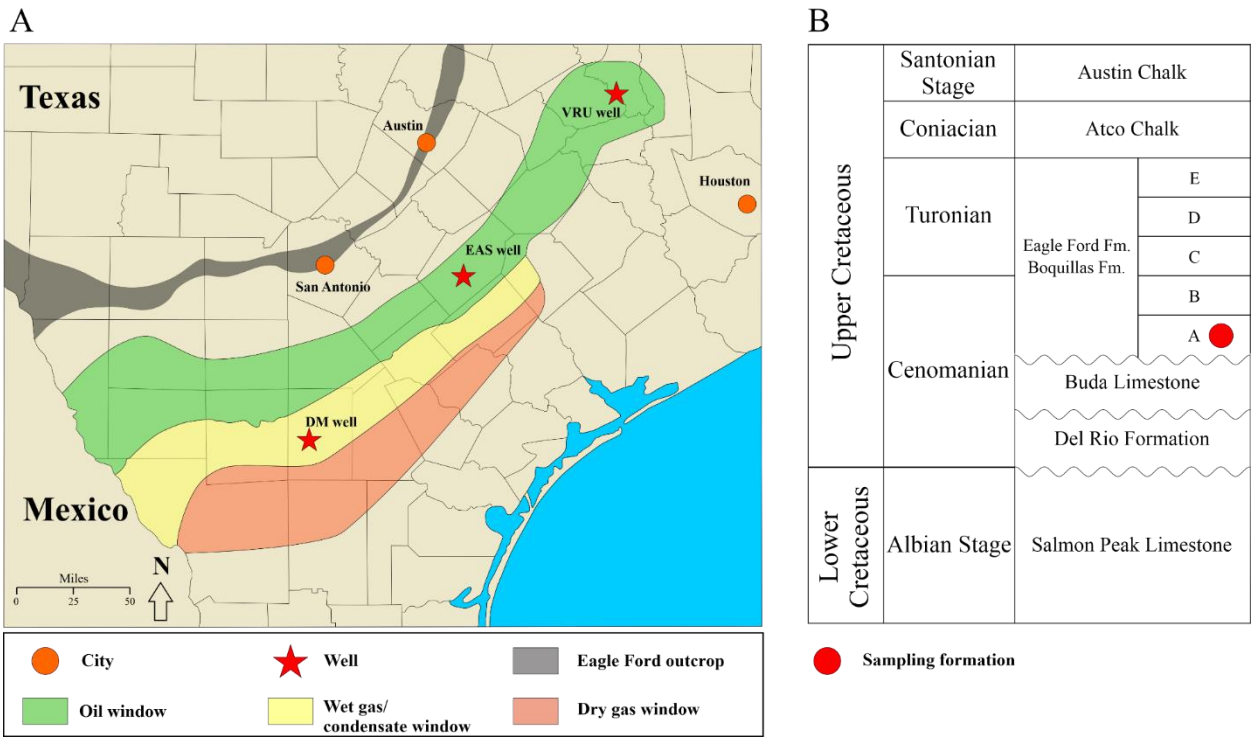

Figure 1(A) Regional map and sampling-well locations (modified from U.S. Energy Information Administration, 2014). (B) Stratragraphy column of southern Texas.

The samples for TOC analyses were pretreated with concentrated hydrochloric acid to remove all inorganic carbon. Then samples were oven-dried after water rinsing and filtering. Oven-dried samples were analyzed by a LECO C230 Carbon Analyzer.

To determine the source rock maturity and hydrocarbon generation potential, a programmed HAWK pyrolysis was conducted on powdered samples. The S1 peak (sometimes referred to as the free oil content, mg HC/g rock) was generated at 300 ^{o}C for 3 minutes. The S2 peak (remaining generation potential, mg HC/g rock) was produced when the oven temperature was increased by 25^{o}C /min from 300 to 650^{o}C. S3 (organic carbon dioxide yield, mg CO_2/g rock) is

the sum of CO_2 released from the sample under 300 to 400°C. T_{max} is the temperature corresponding to the maximum of the S2 peak.

2.3 Petrographic microscopy and scanning electron microscopy

Standard thin sections of 30 μm thickness were made with blue dye impregnation. The Leica DM 750 P polarizing microscope was then used to capture thin section images. The SEM work was conducted on half cubes of 0.5 cm (thick) × 1 cm^2 (cross-sectional area). Samples were first polished gradually with a range of sandpapers (200, 400, 800, 1200, 2000, and 3000 grit) to reduce the surface roughness. The sample was then ion milled by a Hitachi IM4000Plus Ion Milling System, first at 6 keV for 20 min and then 4 keV for 40 min. After ion-milling, the samples were directly imaged with a Hitachi 4800 SEM to investigate the pores at a pore size resolution of ~10 nm over a sample scale of 1 cm.

2.4 Mercury intrusion porosimetry (MIP)

MIP is a cost-effective approach to generating pore structure information such as porosity, pore-throat diameter distribution, and permeability (Gao and Hu, 2013; Hu et al., 2020). A 1cm^3 whole-rock sample was analyzed on a Micromeritics AutoPore IV 9520 with a pressure range of 0.5 to 60,000 psi (0.003 to 413.5 MPa) to obtain the intruded volume of mercury at each pressure step.

2.5 Nitrogen physisorption (NP) and water vapor physisorption (WVP)

The NP tests of granular samples at 20-35 mesh were conducted with a Quantachrome ASiQwin system. The pore diameter size distribution and pore volume were calculated from adsorption-desorption isotherms using the Barrett-Joyner-Halenda (BJH) model (Barrett et al., 1951). After finishing the NP test, the samples were oven-dried at 60°C for 48 h and used for the WVP test.

A dynamic water vapor adsorption test, using a Quantachrome Aquadyne DVS-2, was carried out to determine the sample weight change during water vapor adsorption and desorption processes. The test was conducted under relative humidity (RH) ranges from 0.2 to 95.0% at a constant temperature of 25°C. The sample weight changes were automatically recorded every minute by a high precision balance (at a resolution of 0.1 μg).

2.6 Spontaneous imbibition (SI) of water

The SI tests were conducted in the laboratory with four-side epoxied 1cm^3 cubes at a constant temperature of 23°. The detailed experimental procedure and data processing followed Hu et al. (2001) and Wang et al. (2021b). The sample mass change vs. time was automatically recorded by a high precision balance at a resolution of 0.01 mg (Rad Wag AS 60/220. R2). The 1 cm^3 cubic sample was covered with quick-cure epoxy on all the sides except for two opposing sides, and then hung under a balance with a sample holder. Two beakers of water were placed inside the imbibition chamber to boost the relative humidity and reduce the evaporation from the sample. When an imbibition test was started, an adjustable jack was used to raise the deionized water reservoir till the bottom 1mm of the sample was submerged in the water.

3. Results

3.1 Organic geochemistry

The TOC and pyrolysis results are shown in Table 1. All of the limestone (well EAS) and wackestone (well DM) samples are very low in TOC content (< 0.5%) and have no potential to generate petroleum. T_{max} values are unreliable due to the small S2 peaks. However, Fig. 1 suggests that the Eagle Ford in the EAS well is in the oil window, whereas in the DM well it is in the wet gas/condensate window. The two clayey mudstones (well VRU) samples are organic-rich

with an average TOC content of 2.47%. The high T_{max} and S2 values indicate that the VRU samples are in the late oil window but still have some residual petroleum generation potential, since the hydrogen indices (HI = 100×S2/TOC) are ~160 (Table. 1).

Table 1 TOC and pyrolysis results.

Sample ID	TOC (wt.%)	S1 (mg HC/g)	S2 (mg HC/g)	S3 (mg CO_2/g)	T_{max} (°C)	Hydrogen Index
EAS-A	0.31	0.22	0.29	0.28	431	94
EAS-B	0.18	0.13	0.14	0.26	413	77
EAS-C	0.24	0.15	0.29	0.33	433	122
DM-A	0.32	0.07	0.13	0.22	418	40
DM-B	0.15	0.05	0.07	0.44	405	47
DM-C	0.19	0.04	0.07	0.32	421	37
VRU-A	2.43	1.69	3.77	0.30	450	155
VRU-B	2.51	1.97	4.16	0.25	450	166

3.2 Mineralogy and lithofacies

Samples were selected from a narrow depth interval in each well, so that the XRD results are very similar (Table 2). The EAS samples are dominated by calcite which ranges from 97.1% to 98.1% where quartz and pyrite only account for 1.3-1.6% and 0.1-0.3%, respectively. The mineral compositions of the DM samples are more variable but still carbonate-rich (> 60%), whereas clay minerals are the most abundant in the VRU samples.

The EAS samples are lime mud-supported fossil-rich carbonate rocks. According to Dunham's carbonate rock texture classification (Dunham, 1962) and XRD data (Table 2), the EAS samples are mud-support limestone. Foraminifers, calcispheres, gastropod, and sponge spicules are observed in the clean matrix (Fig. 2). The DM samples are similar to the EAS samples in thin section observations, they are classified as wackestone because it contains more grains and clay minerals. Core plug samples of the two organic-rich VRU mudstones look black in color, and

maroon in thin section under the petrographic microscope. Some gastropods and unidentifiable bioclast mixed with fine sand-to-clay sized debris, and a muddy matrix are visible in the thin sections. The classification of mudstone is not based on the sedimentary texture because the sedimentary texture and clay-sized particles cannot be observed in petrography thin sections most of the time. Therefore, unlike carbonate rock, their classification is based on the composition rather than sedimentary texture. According to the Gamero-Diaz mudstone classification (Gamero-Diaz et al., 2012), the VRU-A is mixed argillaceous mudstone and VRU-B is mixed mudstone.

Table 2 Sample information and mineral composition

Sample ID	Depth (ft)	Weight percentage (%)								
		Quartz	Albite	Calcite	Kutnohorite	Pyrite	Illite	Montmorillonite	Kaolinite	Clinochlore
EAS-A	8269.00	2.6		97.1		0.3				
EAS-B	8270.00	1.3		98.6		0.1				
EAS-C	8270.50	1.6		98.1		0.3				
DM-A	11895.10	13.3		63.7	1.4	1.5	14.5	1.4	4.2	
DM-B	11896.20	5.2		90.8	0.6	0.3	3.2			
DM-C	11897.75	10.5		72.9	1.5	1	11	0.8	2.4	
VRU-A	9732.30	20.6	10.8	28.5		3	34.2	1.7		1.3
VRU-B	9732.33	14.5	2.6	22.2		2.2	56.2	1.3		1

3.3 Pore structure

Based on the pore classification of Loucks et al. (2012), the low TOC, carbonate-rich EAS and DM samples mostly contain mineral matrix pores (both interparticle and intraparticle pores) and microfractures. Due to the higher TOCs, the VRU samples not only have those mineral pore types, but also contain organic matter pores (Fig. 3G-H). In the EAS samples, the framework grains float on the matrix and are rarely in contact with each other (Fig. 2), the pores are present

between particles and the matrix (Fig. 3A-C). Pore sizes at the μm to nm scale are observed inside the framework grains or aggregates, such as poloidsorpellets, and pyrite

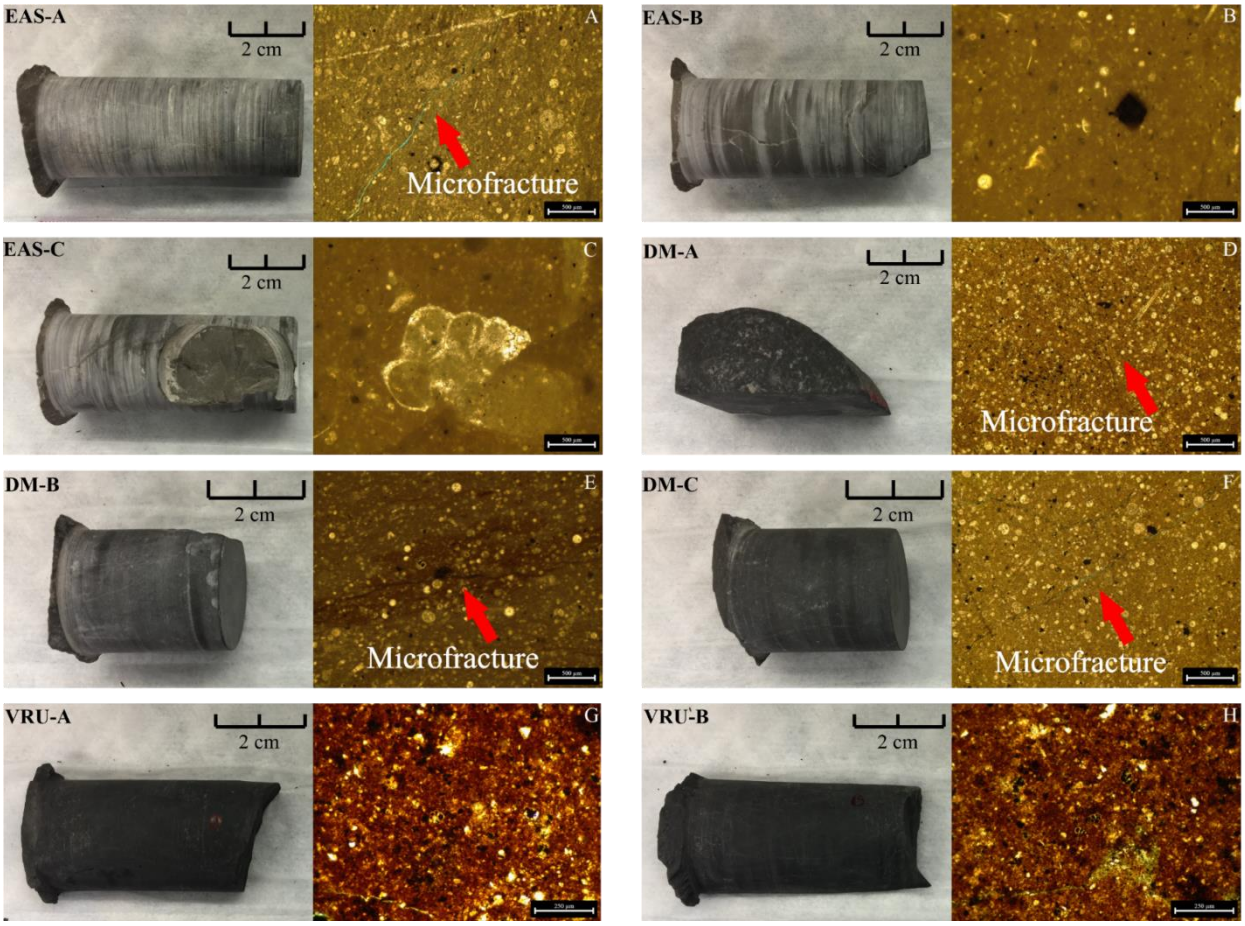

Figure 2 Core plug samples and thin section photos.

aggregates (Fig. 3). Microfractures are observed in the EAS samples, and they can also be seen in thin sections and SEM images. In the DM samples, interparticle pores and intraparticle pores are distributed in the matrix (Fig. 3 D, E, and F). Unlike the EAS and DM samples, the VRU samples contain more than 30% clay and 2% of organic matter, and are dominated by clay mineral-related pores and organic matter-hosted pores (Fig. 3G-I). The organic matter pores often appear inside of the framboidal pyrite, but some of them do appear in the matrix. (Fig. 3G-

H) Considering the VRU samples are in the late oil window, the organic matter is not as porous as in higher maturity mudstones. In Fig. 3G, the outer part of the organic matter is more porous, and the inner part is tighter, which may indicate that the organic matter still has some petroleum generation potential, which is supported by the hydrogen indices of 155 and 166.

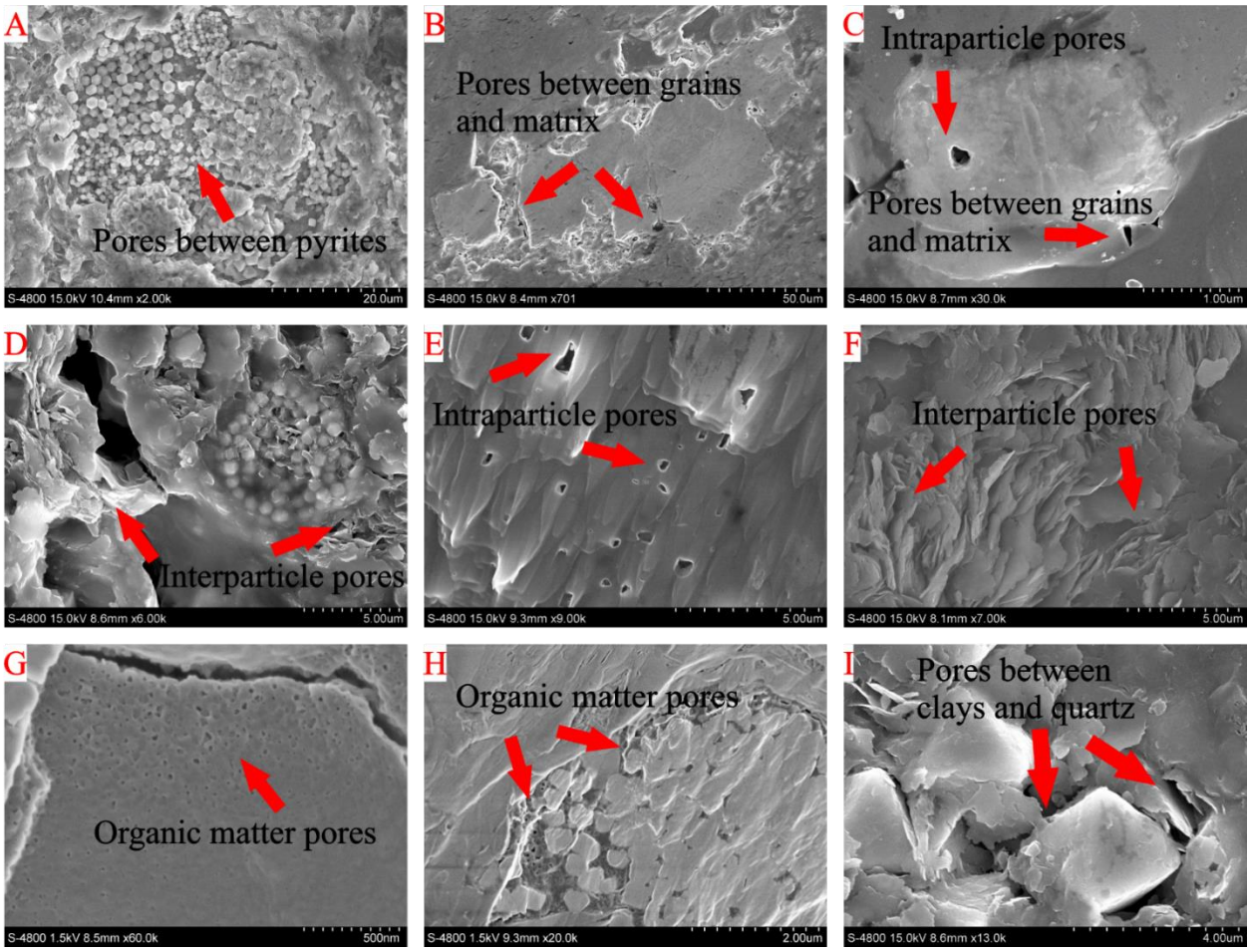

Figure 3 SEM photos. (A) EAS-A, pyrite aggregates; (B) EAS-B, microfractures and pores around and inside of grains; (C) EAS-C, pores inside and around a mineral; (D) DM-A, microfracture around pyrite and clay minerals; (E) DM-B, nm-scale bottle-necked pores in the matrix; (F) VRU-A, pore space in clay minerals; (G) VRU-A, organic matter and organic matter pores. The organic matter is low maturity, the organic pores only appear around the edge; (H) VRU-B, organic pores between pyrite grians; and (I) VRU-B, pore between quartz and clay minerals.

Table 3 presents the porosity data, pore-throat size distribution and permeability for pores from 2.8 nm to 500 μm determined from the MIP test. Overall, the EAS and DM samples have low porosity (2.02% to 3.35%), where the VRU samples have higher porosities with an average of 11.7%. The large percentage of pores with pore throat diameters in the 100,000 to 500,000 nm range suggests that microfractures are relatively abundant in almost all samples, especially for samples EAS-B and DM-B. The three EAS samples, DM-A, and DM-B have a low permeability, ranging from 0.016 to 1.054 mdarcy (10^{-15} m^2), while the DM-C and VRU samples have higher permeability at 10.3 to 11.6 mdarcy.

Table 3 Porosity, pore-throat size distribution and permeability results obtained from MIP tests.

Sample ID	Porosity (%)	Pore-throat diameter %								Permeability (mdarcy)
		100,000-500,000 nm	10,000-100,000 nm	1,000-10,000 nm	100-1,000 nm	50-100 nm	10-50 nm	5-10 nm	2.8-5 nm	
EAS A	2.12	37.47	4.15	2.65	2.50	8.83	18.62	16.00	9.78	1.054
EAS-B	2.47	91.01	6.20	1.69	0.94	0.16	0.00	0.00	0.00	0.420
EAS-C	2.60	49.89	5.71	0.70	0.00	7.22	11.74	16.11	8.64	0.998
DM-A	2.88	75.03	22.65	0.50	0.02	0.33	0.00	0.00	1.47	0.160
DM-B	2.02	97.08	1.35	0.06	0.10	0.64	0.76	0.00	0.00	0.476
DM-C	3.35	27.69	23.16	4.81	5.49	3.92	10.15	18.73	6.05	11.575
VRU-A	12.97	45.95	10.15	2.43	4.50	3.85	12.76	16.41	3.95	11.261
VRU-B	10.42	78.22	6.66	1.56	1.62	0.80	1.51	5.92	3.73	10.296

The hysteresis loops and the pore diameter distribution in the nm range (0.5-260 nm measurable range) from NP are shown in Fig. 4. According to Sing et al. (1985), the EAS samples have H4 loops, and the DM and VRU samples show H3 loops. The shapes of the hysteresis loops suggest that the pores in EAS samples are carbonate-related micro-mesopores, and the pores in DM and VRU samples are mainly plate- or slit-like pores. The pore size distributions over the range of 0.5-260 nm are plotted using the BJH model. Fig. 4 shows that EAS samples have the lowest

maximum N_2 adsorption, whereas the VRU samples have the medium and the DM samples have the highest maximum N_2 adsorption.

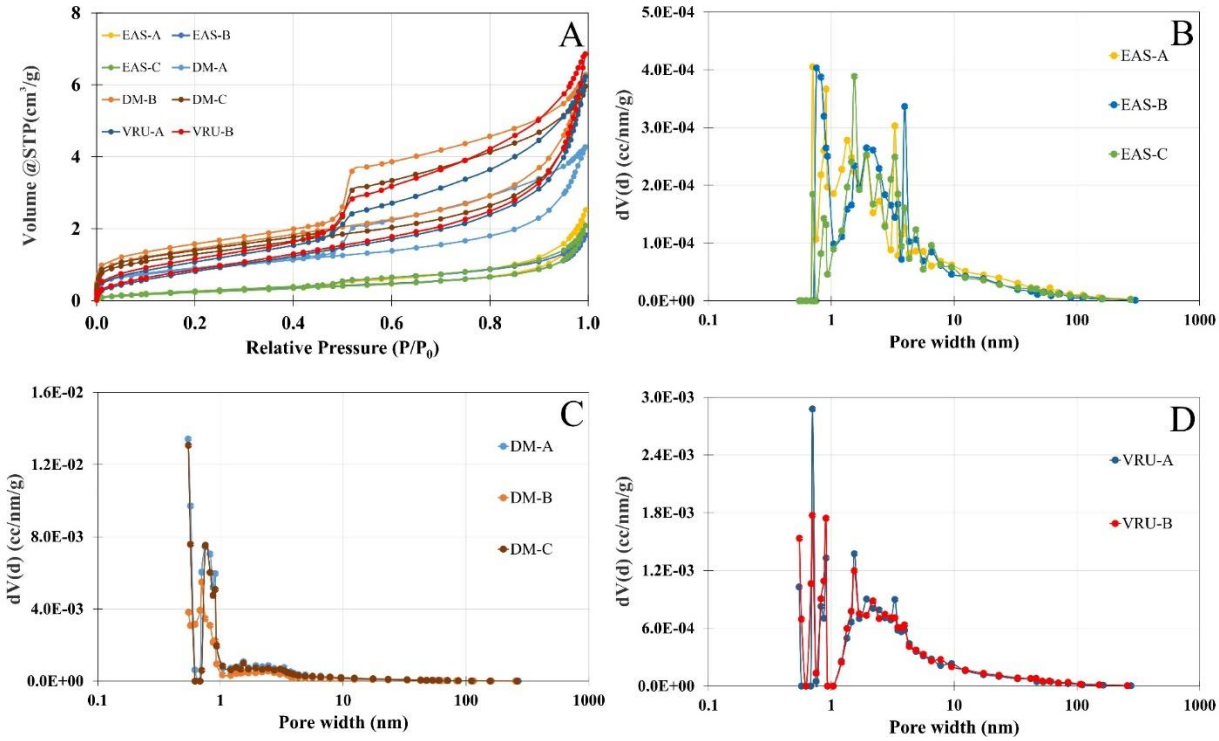

Figure 4 N_2 physisorption results of (A) isotherms; (B) pore size distribution of EAS samples; (C) pore size distribution of DM samples; and (D) pore size distribution of VRU samples.

3.4 Water vapor physisorption

The maximum water vapor adsorption (mg water/g rock) is listed in Table 4. The VRU samples have the highest adsorption capacity with an average of 2.05±0.5 mg/g at 95% relative humidity (RH). The DM samples have lower adsorption capacity ranges from 0.4 to 1.26 mg/g, and the EAS samples have the lowest adsorption capacity of 0.23±0.02 mg/g. The hysteresis loops were determined and interpretated using the approach by Sing et al. (1985) (Fig. 5). The isotherms of VRU samples are H3 type which show increasing adsorption at high RH. This type of isotherm

is often observed for plate-like particles and slit-shaped pores. The isotherms of DM and EAS samples are categorized as H4 type which is indicative of slit-shaped pores domination. To characterize the hysteresis loops and interpret the influencing factors on adsorption, here we used the areal hysteresis index (AHI) method to characterize the water retention ratio during the water vapor desorption (presented in Table 4). The AHI index is expressed as below (Zhu and Selim, 2000; Sander et al., 2005):

$$AHI = \frac{A_{de} - A_{ad}}{A_{ad}} \times 100\% \qquad \text{eq. 1}$$

where A_{de} and A_{ad} are the areas under the desorption and adsorption curves. In the EAS samples (with no clay content), the AHI is as low as 1.35%.

3.5 Spontaneous imbibition

The spontaneous imbibition test was only conducted on the four high carbonate content samples (EAS-A, EAS-B, EAS-C, and DM-B) (Fig. 6). The other samples could not be cut into 1cm^3 cubes because of their fragile nature. The plot of deionized water imbibition versus time is presented on a log-log scale (Fig. 6). In Fig. 6, the imbibition slope could be divided into two

Table 4 Water vapor physisorption results. RH: relative humidity. AHI: areal hysteresis index.

Sample ID	Max adsorption (mg/g)	Adsorption at each RH range/max adsorption			AHI
		0.2-20	20-70	70-95	
EAS-A	0.25	20.2%	36.6%	43.2%	1.35%
EAS-B	0.21	20.6%	39.9%	39.5%	9.98%
EAS-C	0.22	21.1%	34.9%	44.1%	9.38%
DM-A	1.26	29.2%	46.8%	24.0%	26.64%
DM-B	0.51	32.4%	48.1%	19.5%	29.81%
DM-C	0.40	27.8%	51.2%	21.0%	23.33%
VRU-A	2.11	22.0%	47.8%	30.3%	26.39%
VRU-B	2.01	23.0%	48.2%	28.7%	28.24%

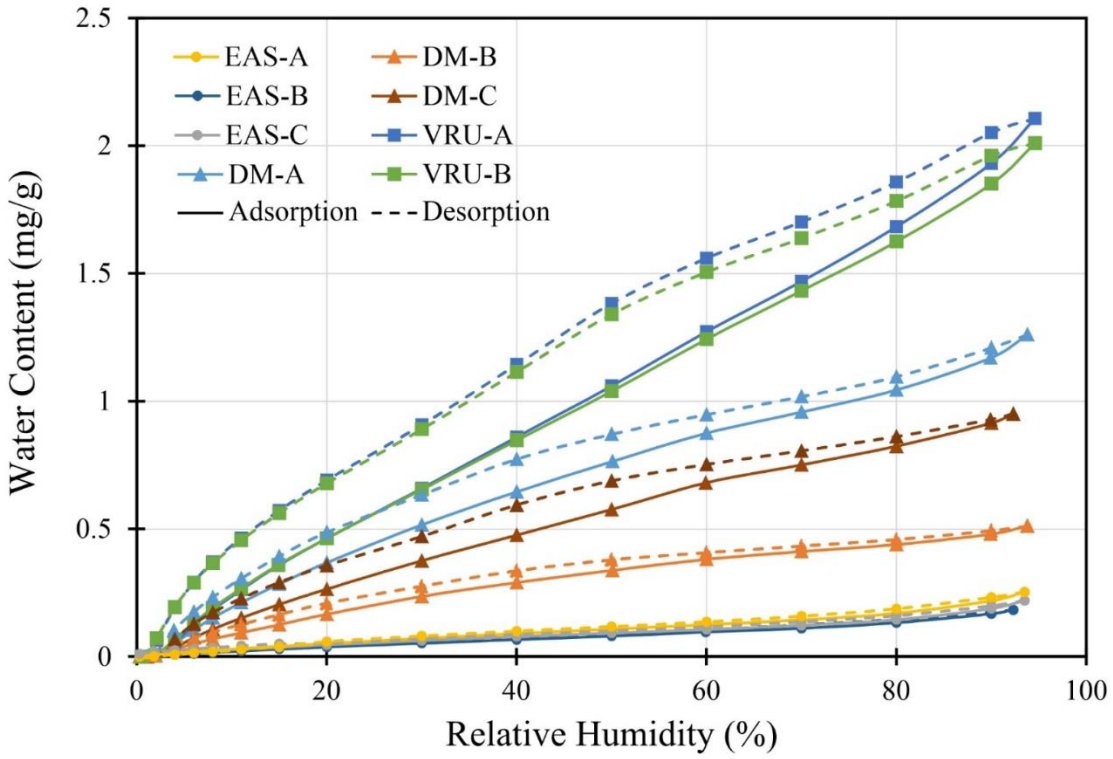

Figure 5 Water vapor physisorption isotherms.

phases: 1st noisy phase (tens seconds to a few minutes) and 2nd matrix phase (several minutes to hours). In the 1st phase, the balance reading is noisy due to the sample's initially contact with the water. After tens of seconds to few minutes, the vibration caused by the sample settling stopped and the balance reading only record the change only made by the matrix imbibition (Hu et al., 2019). This long and stable matrix phase are marked as red in the plots. In this study, only the slope of matrix phase is used to indicate the pore connectivity. In all four samples, the slopes of the steady phase are fall in to less than 0.26 category. According to Hu et al. (2012), a steady phase slope less than 0.26 is characteristic of low pore connectivity towards this fluid.

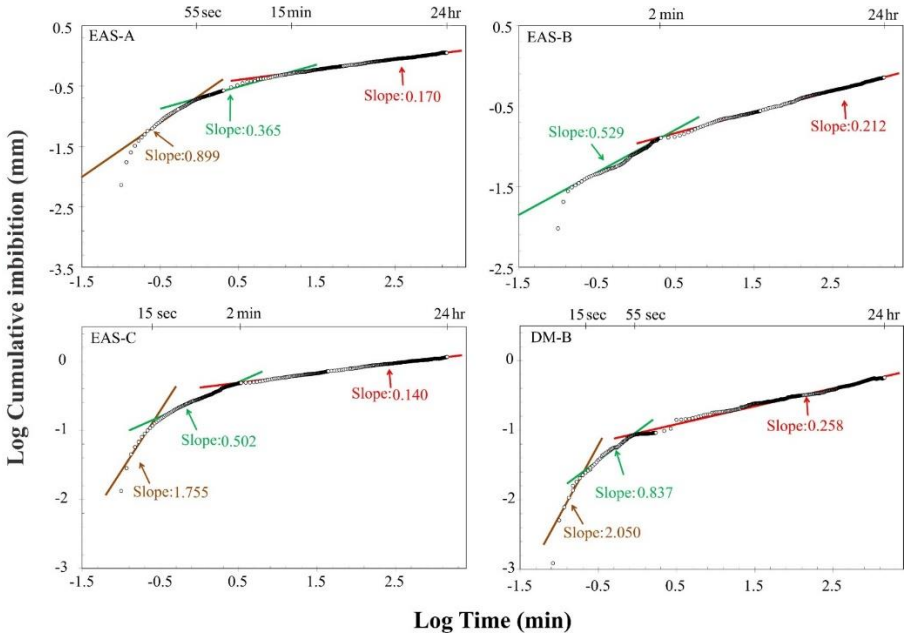

Figure 6 Imbibition results of EAS-A, EAS-B, EAS-C, and DM-B.

4. Discussion

4.1 Pore structure

The pore structure information for the samples, such as pore types, porosity, pore-throat size distribution, and pore size distribution, was based on data from SEM, MIP, and NP analyses. Table 3 shows the pore-throat size distribution from MIP. It worthy to note that sample EAS-B shows no mercury intrusion in the pore-throat size range of 2.8-50 nm, DM-A shows no intrusion in 5-50 nm in diameter, and DM-B shows no intrusion in 2.8-10 nm. The EAS samples have similar sampling depths, mineral compositions, and porosity, but the pore-throat size distribution of EAS-B shows a distinctive difference to the other two samples, namely it has relatively more of the 100-500 μm pores, which are probably microfractures. However, SEM images show that some pores do exist in the 2.8-50 nm range in those samples, both in framboid

pyrite and inside minerals (Fig. 3 D and E). There are two possible reasons to cause this issue. Firstly, the pore connectivity is poor, the nm-sized pores are isolated under the measurement conditions, even some of the pores do respond to the mercury intrusion, but the very small amount of intrusion is less than the detection limit of MIP at 0.1 μL among two pressure steps. Secondly, the DM-B sample contains some ink-bottle pores in nm size, as shown in Fig. 3E. The smaller pore-throats restrict mercury intrusion to enter the larger pores, the pore space from 5-50 nm is controlled by the pore-throat which ranges from 2.8-5 nm. The mercury cannot get into 5-50 nm pores till the pressure is high enough to break through the restriction of 2.8-5 nm pore-throat. Hu et al. (2012; 2015) reported that the pore connectivity controls fluid flow in rock samples, and when the pore connectivity is poor, the fluid used in these fluid-invasion techniques such as MIP cannot access those "isolated" pores. According to Hu et al. (2012), the slope of log (cumulative imbibition) vs. log (imbibition time) can be used to determine the pore connectivity in water-wet rocks. Slopes ≥ 0.5 indicate that the rock has good pore connectivity. In contrast, slopes ≤ 0.26 suggest low pore connectivity. Slopes between 0.26 and 0.5 indicate intermediate pore connectivity. The imbibition slopes of these four samples (EAS-A, EAS-B, EAS-C, and DM-B) with high (> 90%) carbonate contents all have slopes < 0.26, exhibiting low pore connectivity towards water (Fig. 6). The MIP is a fluid intrusion-based technique and can only access the edge-accessible (i.e., connected) pores. The nm size pore space in framboid pyrite and minerals cannot be accessed, even though they are observed in 2D SEM images. During the MIP test, even though some of the smallest size pores are distributed on the surface, the minimal amount of mercury intruded may be less than the detection limit and therefore not recorded. When the samples were crushed to 20-35 mesh, the NP data shows that three EAS samples have

a similar pore size distribution (Fig. 4B), which indicates that even though the mineral composition and porosity are similar, the connectivity can vary among samples.

The VRU mudstone samples show mercury intrusion curve in each measured points between 2.8 nm to 500 μm. The VRU-A has a higher volume of pores at 100-500 μm pore-throats, but less 2.8-50 nm pore-throats, than VRU-B. The 100-500 μm pore-throat is related to the microfractures and the 2.8-50 nm pore-throat are related to clay-associated pores and organic matter-hosted pores as reported in previous research (Loucks et al., 2012; Milliken et al., 2013; Pommer and Milliken, 2015; Hu et al., 2017). The TOC contents of both samples are very similar (Table 1), but the VRU-A has higher clay minerals (Table 2).

4.2 Microfractures

To provide easy-to-follow criteria, here we use a morphology-based description to characterize the microfractures which provides a visual reference (Fig. 7). This morphology-based scheme divides microfractures into seven different types, as seen in our samples, namely (1) amorphous microfractures (Type-A), (2) braided microfractures (Type-B), (3) mineral cracks (Type-M), (4) long microfractures (Type-L), (5) stage microfractures (Type-S), (6) tri-junction microfractures (Type-T), and (7) cross-cutting microfractures (Type-X).

4.2.1 Amorphous microfractures (Type-A)

Amorphous microfracture is a collective name for fractures that are isolated, short in length (several tens to hundreds of μm), and often appear as irregular forms such as straight, curved, dashed, dotted, and zigzag. An example is given in Fig. 7 A. This kind of small-scale microfracture is likely related to the post-coring expansion of gas, pressure release, and desiccation of the matrix (Loucks and Reed, 2016).

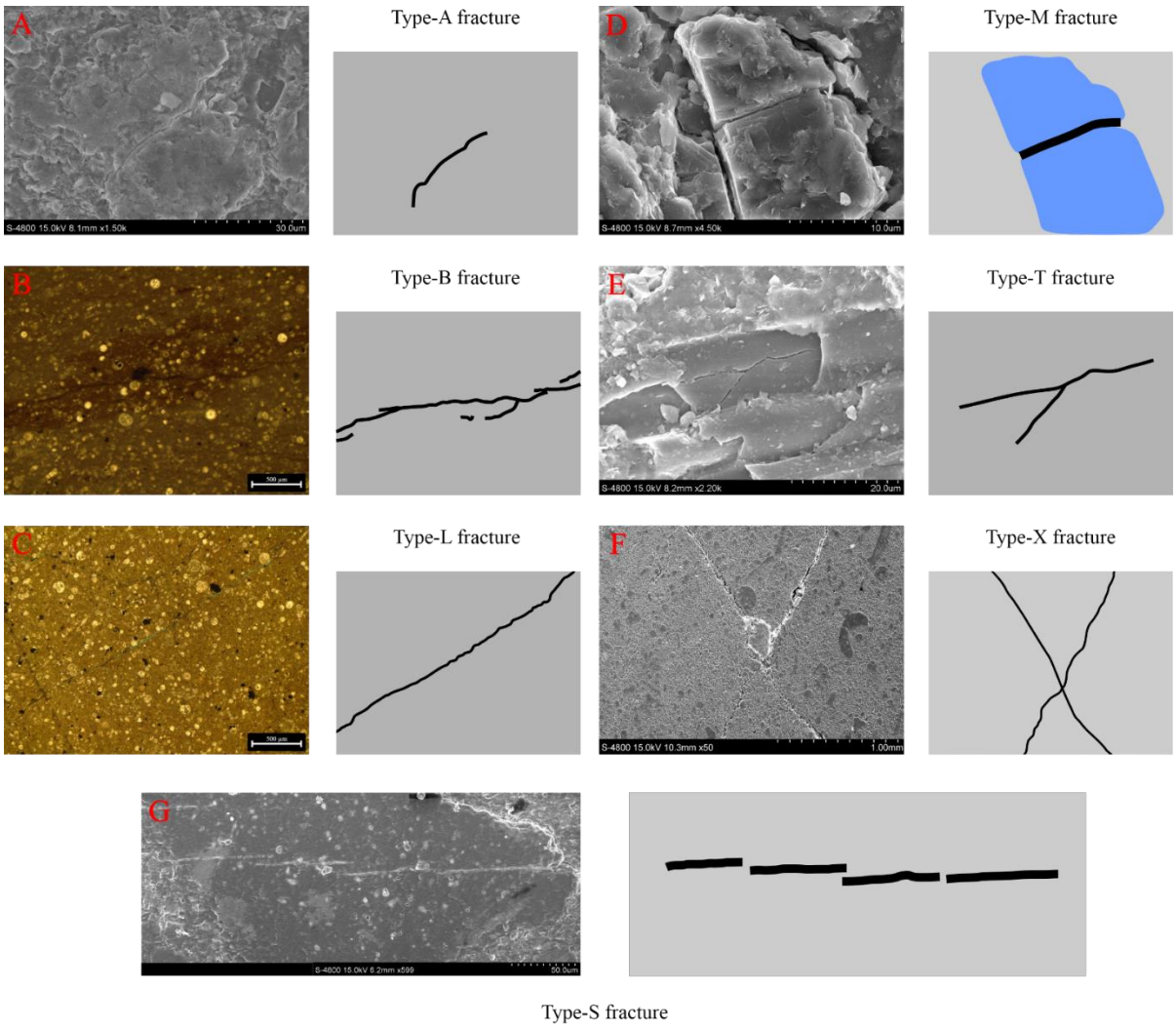

Figure 7 Types of microfractures observed from petrographic and SEM images. A) Type-A fracture, SEM image, DM-C. B) Type-B fracture, petrographic image, DM-A. C) Type-L, petrographic image, DM-C. D) Type-M fracture, SEM image, DM-A. E) Type-T, SEM image, VRU-A. F) Type-X, SEM image, EAS-A. G) Type-S, SEM image, EAS-A.

4.2.2 Braided microfractures (Type-B)

A braided microfracture consisting of multiple small microfractures form a combined pattern like a braid. An example is given in Fig. 7 B. In sandstone and carbonate rocks, tectonically-related braided microfractures can be observed. The fractures are usually fully or partially filled with

mineral precipitation and the origin of these fractures is related to local tectonic movement and diagenesis. (Gale et al., 2004; Hooker et al., 2018; Laubach et al., 2004; Laubach and Ward, 2006). Mudstone also shows braided microfractures in the matrix. However, due to the change in the conditions of pressure, temperature, and fluid-rock interaction, it is very easy to induce artificially braided microfractures (Zhong et al., 2015; Loucks et al., 2016; Ougier-Simonin et al., 2016).

4.2.3 Long microfractures (Type-L)

Long microfractures are distinguished by their length and straightness. The lengths are usually in mm. An example is given in Fig. 7C. Long microfractures can be subdivided into two types based on the fracture sealing. The first type is filled with minerals like calcite, often referred to as calcite veins. The second type has no filling in the fractures and has a clean and sharp surface. The first type is caused by local tectonic activity and the mineral filled in the fracture is related to the composition of the formation fluid (Zeng et al., 2012). The second type is formed by post-coring pressure release and fluid-rock interaction (Loucks and Reed, 2016; Dong et al., 2018). In carbonate rocks, long microfractures develop along the planes of weakness in all directions. In mudstones, the development of long microfractures is parallel to the orientation of the bedding plane (Dong et al., 2018; Du, 2020).

4.2.4 Mineral crack microfractures (Type-M)

Mineral crack microfractures are only developed inside mineral grains, and they are characterized by sharp surfaces and mineral splitting. An example is given in Fig. 7 D. Calcite, dolomite, feldspar, and clay minerals can contain cleavage-like fractures (Gale et al., 2004;

2014). Some minerals such as quartz and hematite do not exhibit the cleavage and they break irregularly.

4.2.5 Tri-junction microfractures (Type-T)

Tri-junction microfractures were first documented by Olsson and Peng (1976). Three microfractures are intersected (Fig. 7E). Twin lamellae concentrate stresses control the generation of the tri-junction microfractures (Olsson and Peng, 1976).

4.2.6 Cross-cutting microfractures (Type-X)

Only the synchronized cross-cutting microfractures can be described as cross-cutting. Olsson and Peng (1976) identified them as type III microfractures, and they can be present in single minerals and mineral aggregates. In our samples, they are present in a carbonate matrix (Fig. 7F).

4.2.7 Stage microfractures (Type-S)

This type of sharp, short, offset microfractures has rarely been reported in previous studies, and the mechanism of formation is still unclear, but it is observed in sample EAS-A (Fig. 7G). Based on its sharp surface and parallel orientation, it may be related to pressure release in the vertical direction or strike-slip in the horizontal direction.

4.3 Microfractures and fluid flow

Many studies (Capuano, 1994; Apaydin et al., 2012; Zhou et al., 2018) suggest that microfractures are important pathways for fluid flow. Our thin section and SEM images show the existence of microfractures in every sample at the scale of 1-3 mm, but those microfractures seem to not improve the pore connectivity in samples which have high carbonate content from the imbibition tests carried out on centimeter-scale samples. This apparent conflict raises the

question as to whether the microfractures are interconnected over a large enough volume, such that they can provide accessible pathways for macro-scale fluid flow. Loucks and Reed (2016) also had the same concern, and pointed out that microfracture networks are widely modeled as contributing to fluid flow, even though that may not be the case in reality. Unlike high-carbonate content samples, the clay-rich samples can generate microfractures during imbibition and the permeability will increase with the development of networked microfractures under laboratory conditions (Dehghanpour et al., 2013; Stavropoulou et al., 2018). Fig. 8 illustrates sporadic and networked microfracture networks with water imbibed into the microfractures. In Fig. 8A-B, water only moves along the connected sporadic microfractures at the base, and does not go any further. In contrast, water penetrates the whole block through the networked microfractures (Fig. 8C-D). Therefore, for microfractures to provide pathways for fluid flow, networks must exist, and sporadic microfractures are not effective at connecting the pore network and enhancing the permeability at a larger scale. If microfractures are abundant enough to enhance the permeability, they should at least be seen to be networked in some thin sections or SEM images if a large enough number of images are acquired from different samples, or other 3D visualization methods, such as computed tomography (CT), are used (Hirono et al., 2003).

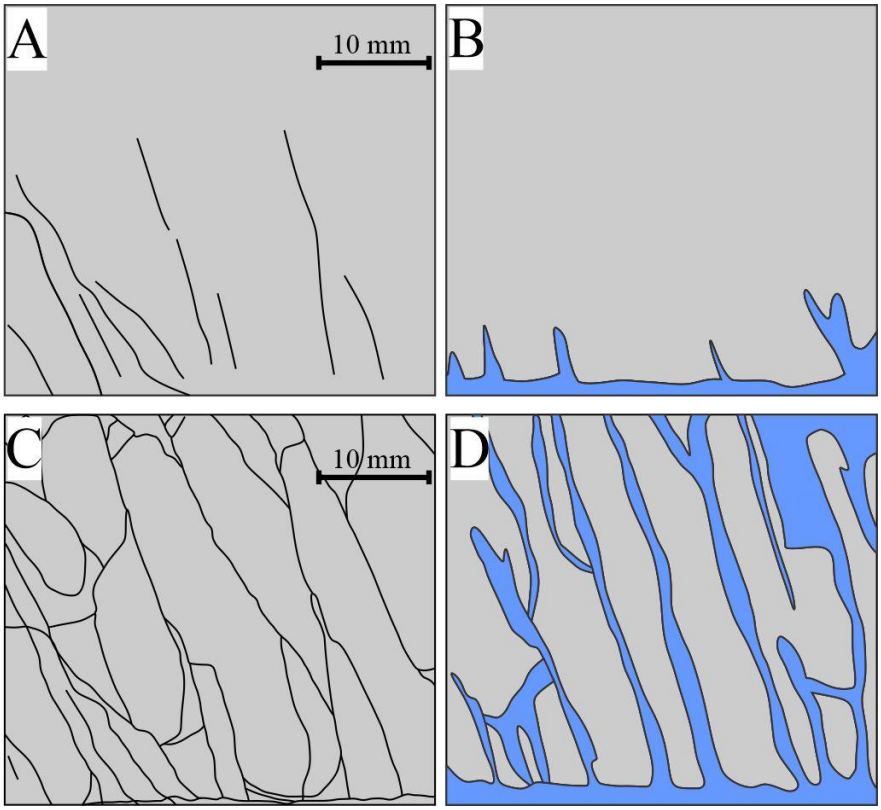

Figure 8 Illustration of sporadic and networked microfractures at the mm scale, illustrated from imbibition-CT photos, modified after Stavropoulou et al. (2018). (A) Sporadic microfracture network; (B) Water imbibition in the sporadic microfracture network, the water stays at a low level; (C) Networked microfractures; and (D) Water imbibition in the networked microfractures, water can penetrate the whole section along the microfractures.

4.4 Water-rock interaction

Since the spontaneous imbibition of water by the four high-carbonate samples is similar (Fig. 6), the water vapor physisorption could provide more insights into water vapor adsorption and desorption in the rock matrix. The hysteresis loops from water vapor adsorption (Fig. 5) reflect the differences in water adsorbed by, versus desorbed from, a sample at a given RH value. Depending on the isotherm, the hysteresis loops exhibit specific behaviors at different ranges of RH values. Yang et al. (2020) arbitrarily divided the isotherm into three ranges, namely low RH (<20% RH), intermediate RH (20-70% RH), and high RH (>70% RH). During adsorption in the

low RH region, water vapor is adsorbed on the solid surface with a high binding energy (Tang et al., 2017). In this region, a monolayer adsorption of water occurs on the clay minerals (Sang et al., 2019), and adsorbed water is present as a film (Lin et al., 2020). The EAS samples contain no clay minerals, and they have the lowest water adsorption. With an increasing clay content, the water adsorption increases, as illustrated by the DM and VRU samples. In the intermediate region, water vapor is adsorbed in multilayers (Lin et al., 2020; Yang et al., 2020). The slope of the adsorption curve in this region is shallower than the low RH region (Fig. 5) because of the thickening of the layer water, such that water in the outer layer(s) is less strongly adsorbed (Lin et al., 2020; Yang et al., 2020). In different lithofacies, the adsorption curves in the high RH region show different behaviors. In the clayey and higher TOC VRU samples, the slopes in the high RH region show the same trend as in the low RH region. However, the wackestone DM samples have shallower slops in the high RH region. On the contrary, the high carbonate EAS samples have steeper slopes in this region. In the high RH region, the water vapor begins to condense under the control of capillary condensation (Lin et al., 2020; Yang et al., 2020).

During desorption process, the adsorbed water content in samples decreases along with the decline in RH (Fig. 5). However, the desorption curve does not overlap with the adsorption curve, and for some RH values the adsorption and desorption curves for the same sample are not even close. Overall, the degree of separation of the curves (hysteresis), characterized by the AHI in Table 4), is higher in the clayey VRU and clayish DM samples. For the EAS samples with no clay, the hysteresis is smaller. However, previous research pointed out that different factors control the hysteresis in different RH regions (Ravikovitch and Neimark, 2002; Morishige and Tateishi, 2003; Lu and Khorshidi, 2015; Lin et al., 2020). In the high and intermediate RH regions, the restricted water desorption has been attributed to the “ink-bottle” effect (a small-

sized pore-throat controls large-sized pore body) (Ravikovitch and Neimark, 2002), such that the retained water needs much more energy to escape from the pore space (Morishige and Tateishi, 2003). In all our samples, the hysteresis is for the most part shown in the high and intermediate RH regions. The ink-bottle pores are reported to be usually present in the organic-rich clay-rich mudstone (Yang et al., 2017; Li et al., 2019). Our SEM images (Fig. 3) also suggest that irregular pores with various cross-cutting shapes and sizes could be ink bottles. The "ink bottle" effect is dominant in the high and intermediate RH regions, and may occur in the low RH region but with less influence (Tang et al., 2017; Yang et al., 2020). The hysteresis loops of the clayey VRU samples and clayish DM samples decrease in the low RH region which is more impacted by the attractive force between clay layers (Lu and Khorshidi, 2015; Lin et al., 2020). In the adsorption process, water molecules need to overcome the attractive force between two clay layers, which increases the difficulty of water adsorption. On the contrary, the attractive force will help to dehydrate the clay layers. This effect makes the low RH region to exhibit less hysteresis than the high and intermediate RH region (Lu and Khorshidi, 2015; Lin et al., 2020).

4.5 Relationship between mineral composition, porosity, and water vapor physisorption

One important controlling factor for water vapor adsorption in geological materials is the mineral composition (Lu and Khorshidi, 2015). Plots of mineral composition vs. maximum adsorbed water content are shown in Figs. 9A-B. Fig. 9A shows the negative relationship between carbonate content vs. the amount of water adsorbed. Previous studies have shown that the surface of carbonate minerals is weakly hydrophobic (Kerisits and Parker, 2004; Rahman et al., 2018), which will reduce the extent of water vapor adsorption. Fig. 9B shows a very good correlation (R^2=0.9879) between water vapor adsorption and clay mineral content. The positive correlation between clay content and water adsorption was also reported by Zolfaghari et al. (2017a). After

water adsorption, clay has the potential to swell and induce microfractures which result in an increased water uptake, although the swelling rate is lower when compared with the imbibition process (Zolfaghari et al., 2017a). In addition, the induced microfractures provide more space for the water vapor adsorption and this increases the maximum water adsorption.

Fig. 9C shows a positive relationship between maximum water adsorption and porosity. It is not hard to understand that more pores can provide more surface area for the mono- and multi-layer adsorption and more void space for capillary condensation. However, the lower porosity samples do not exhibit any correlation. It only looks like there is a correlation because of the high values for the two mudstones. A fourfold increase in porosity does not lead to a fourfold increase in adsorption. So, understanding the nature of, and controls on, this positive relationship needs more data. All three groups of samples show a similar proportion of water adsorption at the low RH region (~20-30%) (Table 4). As discussed before, the low RH region is correlated to the monolayer adsorption, which is mainly related to the presence and the surface chemistry properties of pores associated with clay minerals. In the intermediate RH region, the ratio of adsorbed water in this region to the maximum adsorbed water by the DM and VRU samples (containing clay minerals) is the highest, and above 40% in all cases, whereas in the carbonate EAS samples the values are between 30-40% (Table 4). In the high RH region, the EAS samples show the highest percentage of water adsorption at around 40% of all three groups (Table 4). Zolfaghari et al. (2017b) suggested that the water vapor tends to condense in small pores at the low RH range and in large pores at the high RH range. A large amount of water adsorbed at intermediate and high RH region suggests that water started to condense in the large pores. However, the discussion of prevailing mechanisms for water adsorption in each RH region only

provides a qualitative assessment, and a more realistic relationship between pore structure and water adsorption at each region requires further investigation.

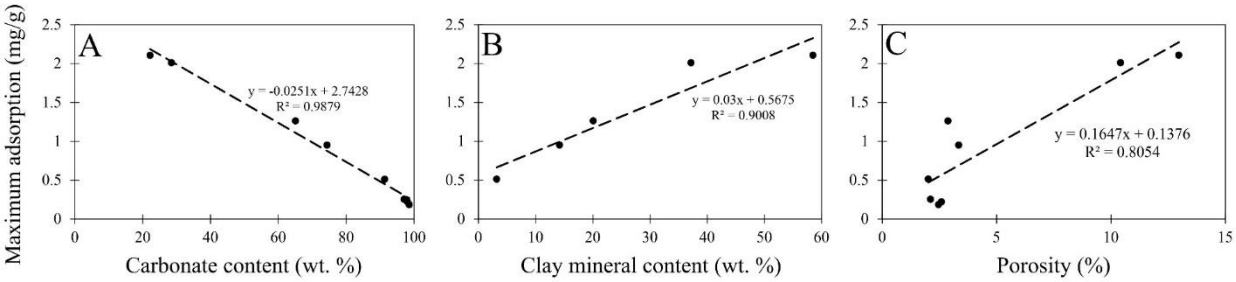

Figure 9 Relationship between maximum water adsorption and (A) carbonate content; (B) clay mineral content; and (C) porosity.

5. Conclusions

A series of petrographic and petrophysical analyses have been performed on three lithofacies of the Lower Eagle Ford Formation. Water vapor physisorption behaviors are strongly related to mineral composition. Microfractures are one of the most important pore types, and they have been characterized and classified by a morphology-based scheme, which could provide a standard method to adequately and accurately describe and interpret microfractures. One problem discussed in this work is whether microfractures can provide efficient pathways for fluid flow. Here, we suggest that when microfractures are very common in a 2D view, and at least some of them interconnect with each other, and hence they could provide efficient flow pathways. Otherwise, microfractures can only be considered as a type of pore space, without contributing to an appreciable rate of fluid flow on a large scale. To obtain more insight into the relationship between microfracture development and properties, fluid flow, and pore

connectivity, a dynamic imbibition-imaging (either gamma ray, X-ray, or neutron) test is recommended on rocks with different lithologies.

Acknowledgments

This project was completed with funding provided by the Nuclear Energy University Program, Office of Nuclear Energy, U.S. Department of Energy, award number DE-NE0008797. We thank late Steve Ruppel, Nathan Ivicic, and Brandon Williamson at the Bureau of Economic Geology at the University of Texas at Austin for providing the core samples used in this study. We also thank Rui Yang, Xiang Lin, and Xiang Zhao at China University of Geosciences (Wuhan, China) for their help and discussions on water vapor physisorption test.

References

Anders, M. H., Laubach, S. E., Scholz, C. H., 2014. Microfractures: A review. Journal of Structural Geology, 69, 377-394.

Apaydin, O. G., Ozkan., E., Raghavan, R., 2012. Effect of discontinuous microfractures on ultra-tight matrix permeability of dual-porosity medium. Society of Petroleum Engineers Reservoir Evaluation & Engineering, 15, 04, 473-485.

Barrett, E. P., Joyner, L. G., Halenda, P. P., 1951. The determination of pore volume and area distributions in porous substances. I. Computations from nitrogen isotherms. Journal of the American Chemical Society, 73, 373–380.

Bednarik, M., Moshammer, B., Heinrich, M., Holzer, R., Laho, M., Rabeder, J., Uhlir, C., Unterwurzacher, M., 2014. Engineering geological properties of Leitha Limestone from historical quarries in Burgenland and Styria, Austria. Engineering Geology, 176, 66-78.

Brunauer, S., Emmett, P. H., Teller, E., 1938. Adsorption of gases in multimolecular layers. Journal of the American Chemical Society, 60, 309–319.

Bryson, L, S., Comez-Gutierrez, I, C., Hopkins, T, C., 2012. Development of a new durability index for compacted shale. Engineering Geology, 139-140, 66-75.

Capuano, R. M., 1994. Evidence of fluid flow in microfractures in geopressured shales. AAPG Bulletin, 78, 10, 1641-1646.

Dehghanpour, H., Lan, Q., Saeed, Y., Fei, H., Qi, Z., 2013. Spontaneous imbibition of brine and oil in gas shales: effect of water adsorption and resulting microfractures. Energy & Fuels, 27, 3039-3049.

Dong, D., Shi, Z., Sun, S., Guo, C., Zhang, C., Guo, W., Guan, Q., Zhang, M., Jiang, S., Zhang, L., Ma, C., Wu, J., Li, N., Chang, Y., 2018. Petroleum Exploration and Development, 45, 5, 2018.

Du, S., 2020. Characteristics and the formation mechanism of the heterogeneous microfractures in the tight oil reservoir of Ordos Basin, China. Journal of Petroleum Science and Engineering, 191, 107176.

Duan, F., Mrugala, M., 1993. Modeling large underground experimental halls for the superconducting super collider. International Journal of Rock Mechanics and Mining Sciences. Abstract, 30, 7, 1333– 1339.

Dunham, R. J., 1962. Classification of carbonate rocks according to depositional texture. In: Classification of Carbonate Rocks (Ed. W.E. Ham), AAPG. Memoir, 1, 108–121.

Frebourg, G., Ruppel, S, C., Loucks, R, G., Lambert, J., 2016. Depositional controls on sediment body architecture in the Eagle Ford/Boquillas system: Insight from outcrops in west Texas, United States. AAPG Bulletin, 100, 4, 657-682.

Gale, J. F. W., Laubach, S. E., Marrett, R. A., Olson, J. E., Holder, J., Reed, R. M., 2004. Predicting and characterizing fractures in dolostone reservoirs: using the link between diagenesis and fracturing. Geological Society, London, Special Publications, 235, 1, 177-192.

Gale, J. F. W., Laubach, S. E., Olson, J. E., Eichhubl, P., Fall, A., 2014. Natural fractures in shale: A review and new observations. AAPG Bulletin, 98, 11, 2165-2216.

Gamero-Diaz, H., Miller, C., Lewis, R., 2012. sCore: A classification scheme for the organic mudstones based on bulk mineralogy. In: AAPG Southwest Section Meeting, Search and Discovery Article #40951.

Gao, Z. Y., Hu, Q. H., 2013. Estimating permeability using median pore-throat radius obtained from mercury intrusion porosimetry. Journal of Geophysics and Engineering, 10, 025014.

Gensterblum, Y., Ghanizadeh, A., Cuss, R, J., Amann-Hildenbrand, A., Krooss, B, M., Clarkson, C, R., Harrington, J, F., Zoback, M, D., 2015. Gas transport and storage capacity in shale gas reservoirs-A review. Part A: Transport processes. Journal of Unconventional Oil and Gas Resources, 12, 87-122.

Gruszkiewicz, M. S., Horita, J., Simonson, J, M., Mesmer, R, E., Hulen, J, B., 2001. Water adsorption at high temperature on core samples from the Geysers geothermal field California, USA. Geothermics, 30, 269-302.

Gu, D., Huang, D., 2016. A complex rock topple-rock slide failure of an anticlinal rock slope in the Wu Gorge, Yangtze River, China. Engineering Geology, 208, 165-180.

Hirono, T., Takahashi, M., Nakashima, S., 2003. In situ visualization of fluid flow image within deformed rock by X-ray CT. Engineering Geology, 70, 37-46.

Hooker, J. N., Laubach, S. E., Marrett, R., 2018 Microfracture spacing distributions and the evolution of fractures in sandstones. Journal of Structural Geology, 108, 66-79.

Hsieh, C., 1980. Vapor Pressure Lowering in Porous Media. Ph.D. Thesis, Stanford University, CA.

Hsieh, C., Ramey, Jr, H. J., 1983. Vapor-pressure lowering in geothermal systems. Society of Petroleum Engineering Journal, 23, 01, 157-167.

Hu, Q. M., Persoff, P., Wang, J. S. Y., 2001. Laboratory measurement of water imbibition into low-permeability welded tuff. Journal of Hydrology, 242, 64-78.

Hu, Q. H., Zhang, Y. X., Meng, X. H., Li, Z., Xie, Z. H., Li, M. W., 2017. Characterization of multiple micro-nano pore networks in shale oil reservoirs of Paleogene Shahejie Formation in Dongying Sag of Bohai Bay Basin, East China. Petroleum Exploration and Development, 44(5): 720–730.

Hu, Q.H., Mann, G., and Zhao, J. H., 2019. Pore structure and fluid uptake of the Yeso, Abo and Cisco formations in the Permian Basin in southeast New Mexico, U.S.A. Interpretation, 7(4): SK1–SK17.

Hu, Q., 2020. Nano-Petrophysical Studies for Nuclear-Waste Repository and Shale-Petroleum Exploitation. Webinar on Science, Engineering, and Technology. (Vebleo Fellow Lecture;

webinar at https://www.youtube.com/watch?v=QAd0-Lu7kyM&ab_channel=Vebleo-ScientificConferences%26Webinars)

Hu, Q., Quintero, R. P., El-Sobky, H. F., Kang, J., Zhang, T., 2020. Coupled nano-petrophysical and organic-geochemical study of the Wolfberry Play in Howard County, Texas U.S.A. Marine and Petroleum Geology, 122, 104663.

Hudec, P., 1989. Durability of rock as function of grain size, pore size, and rate of capillary absorption of water. Journal of Materials in Civil Engineering, 1, 3-9.

Jiang, S., Mokhtari, M., 2019. Characterization of marl and interbedded limestone layers in the Eagle Ford Formation, DeWitt County, Texas. Journal of Petroleum Science and Engineering, 172, 502-510.

Kerisit, S., Parker, S. C., 2004. Free energy of adsorption of water and metal ions on the {1014} Calcite Surface. Journal of the American Chemical Society, 126, 32, 10152-10161.

Keppert, M., Žumár, J., Čáchová, M., Koňáková, D., Svora, P., Pavlík, Z., Vejmelkova, E. and Černý, R., 2016. Water vapor diffusion and adsorption of sandstones: Influence of rock texture and composition. Advances in Materials Science and Engineering, 2016, 8039748.

Khan, M, S., Hossain, S., Ahmed, A., Faysal, M., 2017. Investigation of a shallow slope failure on expansive clay in Texas. Engineering Geology, 219, 118-129.

Ko, L. T., Loucks, R, G., Ruppel, S, C., Zhang, T., Peng, S., 2016. Origin and characterization of Eagle Ford pore network in the south Texas Upper Cretaceous shelf. AAPG Bulletin, 101, 3, 387-418.

Kock, T, D., Turmel, A., Fronteau, G., Cnudde, V., 2017. Rock fabric heterogeneity and its influence on the petrophysical properties of a building limestone: Lede Stone (Belgium) as an example. Engineering Geology, 216, 31-41.

Kranz, R. L., 1983. Microfractures in rocks: A review. Tectonophysics, 100, 449-480. Laubach, S. E., Reed, R. M., Olson, J. E., Lander, R. H., Bonnell, L. M., 2004. Coevolution of crack-seal texture and fracture and fracture porosity in sedimentary rocks: cathodoluminescence observations of regional fractures. Journal of Structural Geology, 26, 967-982.

Laubach, S. E., Ward, M. E., 2006. Diagenesis in porosity evolution of opening-mode fractures, Middle Triassic to Lower Jurassic La Boca Formation, NE Mexico. Tectonophysics, 419, 75-97.

Lehrmann, D. J., Yang, W., Sickmann, Z, T., Ferrill, D, A., McGinnis, R, N., Morris, A, P., Smart, K, J., Gulliver, K, D, H., 2019. Controls on sedimentation and cyclicity of the Boquillas and equivalent Eagle Ford Formation from detailed outcrop studies of western and central Texas, U.S.A. Journal of Sedimentary Research, 89, 629-653.

Li, F., Wang, M., Liu, S., Hao., 2019. Pore characteristics and influencing factors of different types of shales. Marine and Petroleum Geology, 102, 391-401.

Li, J., Li, X., Wu, K., Wang, X., Shi, J., Yang, L., Zhang, H., Sun, Z., Wang, R., Feng, D., 2016. Water sorption and distribution characteristics in clay and shale: Effect of surface force. Energy & Fuels, 30, 8863-8874.

Lin, X., Hu, Q., Chen, Z., Wang, Q., Zhang, T., Sun, M., 2020. Changes in water vapor adsorption and water film thickness in clayey materials as a function of relative humidity. Vadose Zone Journal, 19, 1, e20063.

Liu, K., Sheng, J., 2019. Experimental study of the effect of stress anisotropy on fracture propagation in Eagle Ford shale under water imbibition. Engineering Geology, 249, 13-22.

Liu, k., Sheng, J., Zhang, Z., 2020. A simulation study of the effect of clay swelling on fracture generation and porosity change in shales under stress anisotropy. Engineering Geology, 278, 105829.

Loucks, R. G., Reed, R. M., Ruppel, S. C., Hammes, U., 2012. Spectrum of pore types and networks in mudrocks and a descriptive classification for matrix-related mudrock pores. AAPG Bulletin, 96, 6, 1071-1098.

Loucks, R. G., Reed, R., 2016. Natural microfractures in unconventional shale-oil and shale gas systems: Real, hypothetical, or wrongly defined? Gulf Coast Association of Geological Societies Journal, 5, 64-72.

Lu, N., Khorshidi, M., 2015. Mechanisms for soil-water retention and hysteresis at high suction range. Journal of Geotechnical and Geoenvironmental Engineering, 141, 8.

Lyu, Q., Long, X., Ranjith, P, G., Tan, J., Kang, T., 2018. Experimental investigation on the mechanical behaviors of a low-clay shale under water-based fluids. Engineering Geology, 233, 124-138.

Milliken, K. L., Rudnicki, M., Awwiller, D, N., Zhang, T, W., 2013. Organic matter-hosted pore system, Marcellus formation (Devonian), Pennsylvania. AAPG Bulletin, 97, 2, 177-200.

Morsy, S., Gomma, A., Sheng, J. J., 2014. Improvement of Eagle Ford Shale Formation's water imbibition by mineral dissolution and wettability alteration. Proceeding of SPE Annual Technical Conference and Exhibition, Woodland, Texas, April 8-10. Paper, SPE 168985.

Morishige, K., Tateshi, N., 2003. Adsorption hysteresis in ink-bottle pore. Journal of Chemical Physics, 199, 2301-2306.

Mullen, J., 2010. Petrophysical characterization of the Eagle Ford Shale in south Texas. Proceeding of Canadian Unconventional Resources & International Petroleum Conference, Calgary, Alberta, Canada, October, 19-21. Paper, CSUG/SPE 138145.

Olsson, W. A., Peng, S. S., 1976. Microcrack nucleation in Marble. International Journal of Rock Mechanics and Mining Sciences, 13, 53-59.

Ougier-Simonin, A., Renard, F., Boehm, C., Gilbert, V, S., 2016. Microfracturing and microporosity in shales. Earth-Science Reviews, 162, 198-226.

Pavlík, Z., Žumár, J., Medved I., Cˇerný R., 2012. Water vapor adsorption in porous building materials: Experimental measurement and theoretical analysis. Transport in Porous Media, 91, 939-954.

Pommer, M., Milliken, K., 2015. Pore type and pore size distribution across thermal maturity, Eagle Ford Formation, Southern Texas. AAPG Bulletin, 99, 9, 1713-1744.

Rahaman, A., Grassian, V. H., Margulis, C. J., 2008. Dynamics of water adsorption onto a calcite surface as a function of relative humidity. Journal of Physical Chemistry C, 112, 6, 2109-2115.

Ravikovitch, P. I., Neimark, A. V., 2002. Experimental confirmation of different Mechanisms of Evaporation from ink-bottle type pores: equilibrium, pore blocking, and cavitation. Langmuir, 18, 9830-9837.

Sang, G., Liu, S., Elsworth, D., 2019. Water vapor sorption properties of Illinois shales under dynamic water vapor conditions: Experimentation and modeling. Water Resource Research, 55, 8, 7212-7228.

Sander, M., Lu, Y., Pignatello, J., 2005. A thermodynamically based method to quantify true sorption hysteresis. Journal of Environmental Quality, 34, 3, 1063-1072.

Shang, S., Horne, R. N., Ramery, Jr, H. J., 1995. Water vapor adsorption on geothermal reservoir rocks. Geothermics, 24, 4, 523-540.

Sing, K. S. W., Everett, D. H., Haul, R, A, W., Moscou, L., Pierotti, R, A., Rouquerol, J., Siemieniewska, T., 1985. Reporting physisorption data for gas/solid systems with special reference to the determination of surface area and porosity. Pure and Applied Chemistry, 57, 4, 603-619.

Sun, H., Mašín, D., Najser, J., Scaringi, G., 2020. Water retention of a bentonite for deep geological radioactive water repositories: High-temperature experiments and thermodynamic modeling. Engineering Geology, 269, 105549.

Sun, Y., Zhang, H., Wu, Q., Wei, M., Bai, B., Ma, Y., 2013. Experimental study of friction reducer flows in microfracture during slickwater fracturing. Proceeding of SPE Annual Technical Conference and Exhibition, Woodland, Texas, April 8-10. Paper, SPE 164053.

Stavropoulou, E., Ando, E., Tengattini, A., Briffaut, M., Dufour, F., Atkins, D., and Armand, G., 2018. Liquid water uptake in unconfined Callovo Oxfordian clay-rock studied with neutron and X-ray imaging. Acta Geotechnica, 14, 19-33.

Tang, X., Ripepi, N., Valentine, K. A., Keles, C., Long, T., Gonciaruk, A., 2017. Water vapor sorption on Marcellus shale: Measurement, modeling and thermodynamic analysis. Fuel, 209, 606-614.

U.S. Energy Information Administration, 2014. Updates to the EIA Eagle Ford Play Maps. U.S. Department of Energy, Washington, D.C., Accessible at https://www.eia.gov/maps/pdf/eagleford122914.pdf

Wang, Q., Zhang, X., Hu, Q., Lin, X., 2021. How artificial fractures and bedding plane influence the fluid movement in the fracture-matrix dual-connectivity system of Barnett shale. In: AAPG Annual Convention and Exhibition online Meeting, Search and Discovery Article #11353.

Wang, Q., Zhou, W., Hu, Q., Xu, H., Meendsen, F., Shu, Y., Qiao, H., 2021. Pore geometry characteristics and fluid-rock interactions in the Haynesville shale, East Texas, United States. Energy & Fuels, 35, 237-250.

Wang, T., Tian, S., Li, G., Sheng, M., Ren, W., Liu, Q., Tan, Y., Zhang, P., 2019. Experimental study of water vapor adsorption behaviors on shale. Fuel, 248, 168-177.

White, D. E., 1970. Characteristics of Geothermal Resources. In Geothermal Energy (Edited by Kruger and Otte), Chapter 4, 69. Stanford Press, Stanford, CA.

Yang, R., Jia, A., He, S., Hu, Q., Dong, T., Hou, Y., Yan, J., 2020. Water adsorption characteristics of organic-rich Wufeng and Longmaxi Shale, Sichuan Basin (China). Journal of Petroleum Science and Engineering, 193, 107387.

Yang, R., Hao, F., He, S., He, C., Guo, X., Yi, J., Hu, H., Zhang, S., Hu, Q., 2017. Experimental investigations on the geometry and connectivity of pore space in organic-rich Wufeng and Longmaxi shales. Marine and Petroleum Geology, 84, 225-242.

Youn, H., Tonon, F., 2010. Effect of air-drying duration on the engineering properties of four clay-bearing rocks in Texas. Engineering Geology, 115, 58-68.

Zeng, L., 2010. Microfracturing in the Upper Triassic Sichuan Basin tight-gas sandstones: Tectonic, overpressure and diagenetic origins. AAPG Bulletin, 94, 12, 1811-1825.

Zeng, L., Tang, X., Wang, T., Gong, L., 2012. The influence of fracture cements in tight Paleogene saline lacustrine carbonate reservoirs, western Qaidam Basin, northwest China. AAPG Bulletin, 96, 11, 2003-2017.

Zhang, N., Liu, L., Hou, D., He, M., Liu, Y., 2014. Geomechanical and water vapor absorption characteristics of clay-bearing soft rocks at great depth. International Journal of Mining Science and Technology, 24, 811-818.

Zhang, N., He, M., Liu, P., 2012. Water vapor sorption and its mechanical effect on clay-bearing conglomerate selected from China. Engineering Geology, 141-142, 1-8.

Zhong, J., Liu, S., Ma, Y., Yin, C., Liu, C., Li, Z., Liu, X., Li, Y., 2015. Macro-fracture mode and micro-fracture mechanism of shale. Petroleum Exploration and Development, 42, 2, 269-276.

Zhou, X., Ding, W., He, J., Li, A., Sun, Y., Wang, X., 2018. Microfractures in the middle carboniferous carbonate rocks and their control on reservoir quality in the Zanaral oilfield. Marine and Petroleum Geology, 92, 462-476.

Zhu, H., Selim, H. M., 2000. Hysteretic behavior of metolachlor adsorption-desorption in soils. Soil Science, 165, 8, 632-645.

Zolfaghari, A., Dehghanpour, H., Holyk, J., 2017. Water sorption behavior of gas shales: I. Role of clays. International Journal of Coal Geology, 179, 130-138.

Zolfaghari, A., Dehghanpour, H., Xu, M., 2017. Water sorption behavior of gas shales: II. Pore size distribution. International Journal of Coal Geology, 179, 187-195

CHAPTER III

Micro- to nano-scale areal heterogeneity in pore structure and mineral compositions of a sub-decimeter-sized Eagle Ford Shale

Qiming Wang[a], Qinhong Hu[a, *], Chen Zhao[a], Xiaoguang Yang[a,b] , Tao Zhang[a], Jan Ilavsky[c], Ivan Kuzmenko[c], Binyu Ma[d], and Yukio Tachi[e]

[a] Department of Earth and Environmental Sciences, the University of Texas at Arlington, TX 76019, USA

[b] School of Energy Resources, China University of Geoscience (Beijing), Beijing, 100083, China

[c] X-ray Science Division, Advanced Photon Source, Argonne National Laboratory, IL 60439

[d] Shandong Provincial Key Laboratory of Deep Oil and Gas, China University of Petroleum (East China), Qingdao 266580, China

[e] Department of Geological Disposal Research, Japan Atomic Energy Agency, Ibaraki-ken, 319-1194, Japan.

Submitted to:

Journal of Geophysical Research - Solid Earth

[*] Corresponding author: maxhu@uta.edu

Key Words: Eagle Ford Shale, X-ray scattering, pore structure, μ-XRF, heterogeneity

Abstract

Mineral and organic matter compositions & pore structures of fine-grained shale influence reservoir properties. To improve understanding of the spatial heterogeneity in core-sized samples, methods of microscale X-ray fluorescence (μ-XRF) mapping, (ultra-) small-angle x-ray scattering [(U)SAXS] and wide-angle X-ray scattering (WAXS) have been used to determine elemental, pore structure variations in samples up to ~10 cm on two samples prepared at circular and rectangular orientations from a piece of Eagle Ford Shale outcrop in South Texas, USA. In addition, thin section petrography and field emission-scanning electron microscopy (FE-SEM) observations, X-ray diffraction (XRD), total organic carbon (TOC), and pyrolysis were utilized to investigate the potential spatial heterogeneity of pore types, mineral and organic matter compositions for cm-sized samples at both orientations. Overall, the siliceous-carbonate mineral contents in these two samples (8 cm×8 cm×0.8 mm and 5 cm×8 cm×0.8 mm in terms of width×length×thickness) of carbonate-rich Eagle Ford Shale vary between laminations at mm scales. For the circular sample, porosity and surface area variations range from 0.82 to 3.04% and 1.51 to 14.1 m^2/g, respectively. For the rectangular sample, values for porosity and surface area vary from 0.93 to 2.50% and 3.95 to 10.8 m^2/g. By analyzing six selected sub-samples on each of two samples with X-ray scattering and XRD techniques, nm-sized pores are mainly interparticle ones in the higher calcite regions, where the porosity is also relatively lower, while the lower calcite regions consist of both interparticle and intraparticle pore types with higher porosity. Finally, the μ-XRF and (U)SAXS are combined to generate porosity distribution maps to provide more insights about the porosity heterogeneity related to the laminations and fractures at our observational scales.

1. Introduction

Successful and economical recovery of gas and oil from shale has become one of the hottest geological topics in recent years. Compared to conventional sandstone reservoirs, shale is well known for its complex pore systems and high heterogeneity from nanometer to basin scales (Peng et al., 2017; Borrok et al., 2019; Ma et al., Mighani., 2019; Zhang et al., 2019; Huang et al., 2020). Complementary with wireline log and seismic data, core analyses are a direct measurement of rock properties. However, they are limited by their resolution and sample holding capacity of various measurement approaches and associated instrumentation. Cores are usually analyzed after plugging, cutting, and/or crushing which will lead to the issues of inability of studying, and altering, the heterogeneity at the dm-scale. With the improvement in instrumentation, a variety of non-destructive techniques is available to assess the pore structure and geochemical properties of core-sized (commonly 2.5 cm in diameter) samples. Microscale X-ray fluorescence (μ-XRF) mapping has been applied in core-sized samples to visualize the elemental and laminar distribution (Reed et al., 2019; Birdwell et al., 2019; Barker et al., 2020a; 2020b). Wang et al. (2021b) recently applied a rapid and high-precision (ultra) small-angle X-ray scattering [(U)SAXS] technique to characterize the porosity, pore size distribution, surface area and their distribution in a Barnett Shale sample across an area of several tens of cm^2.

The Cretaceous Engle Ford Shale is a prolific petroleum reservoir in the central to southwest Texas region (U.S. Energy Information Administration, 2022). The organic matter-rich beds of the Eagle Ford Formation have been extensively studied with regard to depositional environment, diagenesis, mineral composition, organic matter type, pore types and pore-size distribution, and water-rock interaction (e.g., Pommer and Milliken, 2015; Frebourg et al., 2016; Alnahwi and Loucks., 2018; Wang et al., 2021a). These studies indicate a high degree of heterogeneity across multiple

observational scales. At the field scale across several counties, the organic matter (OM)-rich beds are interbedded with OM-poor limestones, and the proportion of OM-rich shale vs. limestone negatively influences the formation fracability and positively the petroleum production (Breyer et al., 2015). On the core scale of centimeters, the Eagle Ford Shale shows a lithologic variation from coccolith-rich pellets to siliceous-argillaceous seams, and foraminifera (Reed et al., 2019), and there are still many remaining needs for further investigation into larger-sized samples for the decimeter-scale variability in properties such as pore structure, mineral and OM composition.

This work has employed μ-XRF mapping, (U)SAXS, and wide-angle X-ray scattering (WAXS) to investigate the spatial heterogeneity of the elemental & mineralogical composition and pore structure on two Eagle Ford Shale wafers taken perpendicular to each other. Then, six locations on each sample (1 cm×1 cm×0.8 mm) showing large variations in pore structure and elemental composition were selected and cut into chips. These sub-samples were processed at different sizes for analyses by petrographic microscopy, field emission-scanning electron microscopy (FE-SEM), X-ray diffraction (XRD), total organic carbon content (TOC), and pyrolysis to investigate the spatial heterogeneity of sedimentary structure, mineral composition, pore types, organic richness, and thermal maturity.

2. Methods

2.1 Sample collection and preparation

A Cretaceous-aged Eagle Ford Shale sample was collected from an outcrop outside of Del Rio city, TX. First the outcrop was cored as a cylinder at 10.2 cm in diameter and 10 cm in height, and then two samples perpendicular to each other were cut at a thickness of 0.8 mm (Fig 1A); both samples are perpendicular to the bedding plane of the original outcrop. The circular sample (C sample in later texts) shown in Fig. 1B has a diameter of 10.2 cm, and the rectangular sample (R

sample) shown in Fig. 1C has a dimension of 10.2 cm×6.1 cm. Samples were placed in an oven at 60 C° for 2 days to remove the moisture in the connected pore space before analyses. Both μ-XRF mapping and X-ray scattering were first carried out on these C and R whole samples, and then selected locations were cut into 1cm×1cm×0.08 mm sub-samples (orange squares in Fig. 1B-C) for X-ray diffraction (XRD) analyses and scanning electron microscopy (SEM) imaging, and crushed to powder for the analyses of total organic carbon (TOC) and pyrolysis. The rock chips shown in blue rectangular (Fig. 1B-C) were prepared to make four thin sections for petrography. The rest of rock samples in orange squares and blue rectangles were ball-milled as powders for bulk XRD analyses.

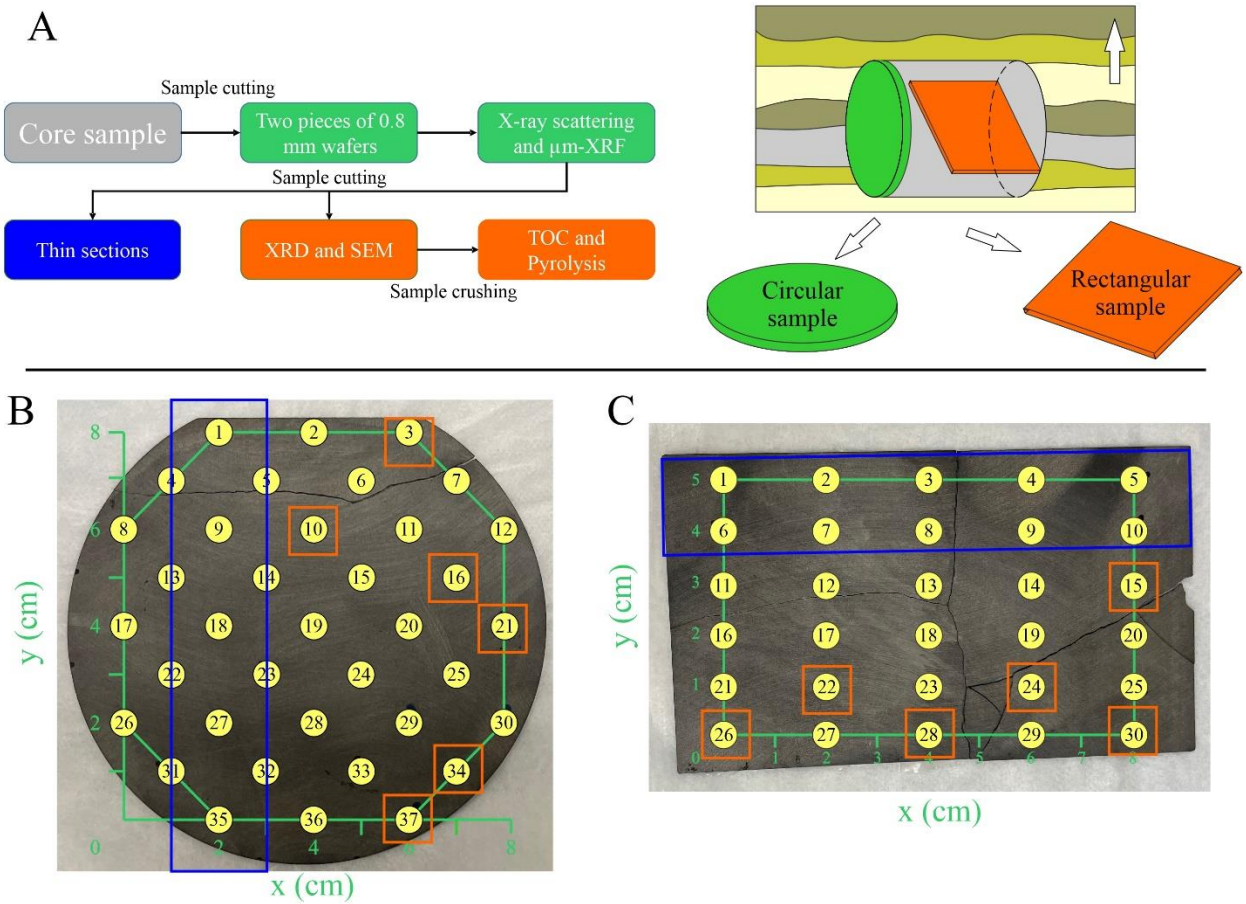

Figure 1. Workflow of sample preparation (A) and experiments at different sampling locations (yellow dots: X-ray scattering; a blue rectangle: thin-section petrographic microscopy; orange

squares: XRD, SEM, TOC and pyrolysis) for Circular (Fig. 1B) and Rectangular (Fig. 1C) samples.

2.2 X-ray scattering

Both ultra-small angle X-ray scattering (USAXS) and small-angle X-ray scattering (SAXS) were conducted on the C and R samples to investigate the areal heterogeneity of porosity, pore size distribution, and surface area distribution over a pore-diameter scale of 1-1000 nm, and wide-angle X-ray scattering (WAXS) was used to determine the mineral types. USAXS/SAXS/WAXS analyses were conducted at 9-ID beamline of Advanced Photo Source (APS) at Argonne National Laboratory. The detailed beamline parameters, fundamental principles, analyses procedure, and data processing follow the work of Ilavsky and Jemian (2009), Ilavsky et al. (2018), and Wang et al. (2021b). For the C sample, a total of 37 positions were scanned (Fig. 1B), with each position scanned at 3-4 beam spots (labeled as A to C-D) following the sequence in Wang et al. (2021b) for a total of 132 beam spots being scanned. For the R sample, there was 30 positions (Fig. 1C), and each position was scanned at 2-3 beam spots for a total of 72 beam spots. Each beam spot only took 90, 10, and 10 seconds to complete the sequential runs of USAXS and SAXS (for pore structure) & WAXS (for mineral composition). Hereafter individual beam spots are described as, for example, Position 1A or Position 2B, where the former refers to Position 1 & beam spot A, and the latter to Position 2 & beam spot B. In brief summary, the USAXS and SAXS are combined to be (U)SAXS to determine the porosity, pore diameter distribution, and surface area, at beam spots of 0.8 mm×0.8 mm, and the WAXS is used to determine the type of minerals, at the same beam spots but a smaller area of 0.8 mm × 0.2 mm.

2.3 Micro-X-ray Fluorescence Mapping

μ-XRF mapping is a fast and non-destructive method that can quantitatively measure the spatial elemental distribution on the surface of mm to cm-sized samples (Nikonow and Rammlmair, 2016; Birdwell, et al., 2018). Our data were obtained from a μ-EDXRF spectrometer M4 Tornado manufactured by Bruker, and the chemical elements Al, Ca, Fe, K, Mg, Mn, Na, and Si were selected to be monitored at 50 kV. The maximum resolution of μ-XRF scanning is 14 μm, and the scanning time depends on the sample size and resolution. For the sub-dm-sized samples used here with the best resolution, the scanning time is around 20 hours.

2.4 Petrographic microscopy

To investigate the changes in sedimentary textures for C and R samples, a rectangular area of ~2 cm × 10 cm on both samples was cut out for petrographic microscopy (Fig. 1B-C), and the photos of prepared thin sections were taken under the Leica DM 750P polarizing microscope.

2.5 X-ray diffraction

After X-ray scattering and μ-XRF mapping for pore structure and elemental composition of the large-sized C and R samples, six sub-samples as rock chips (1 cm×1 cm×0.8 mm) from areas showing large variations were selected and cut out from each sample, in order to determine the mineral compositions by XRD on the intact sample. In addition, a ball-milled powder sample from the rest of rock chips after cutting of twelve sub-samples was prepared to investigate the average mineral composition of the sample. The XRD analyses were conducted on a Shimadzu MaximaX XRD-7000, and the 2θ was set to be 20 to 70 degrees. The Jade 9 analysis program was used to determine the mineral compositions from the raw spectral data.

2.6 Field emission-scanning electron microscopy

Six selected sub-samples on each of C and R samples were gradually polished with sandpapers ranging from 200, 400, 800, 1200, 2000, and 3000 grits. After polishing, samples were coated with Au/Pt in CrC-100 Sputtering system and then directly examined by Hitachi 4800 SEM to investigate the pore types. In this study, images were collected with secondary electrons (SE) mode under 15 for minerals and their related pores and 1.5 kV for organic matters.

2.7 TOC and pyrolysis

When the previous analyses were finished, these 12 selected sub-samples from C and R samples were crushed to be powders (<75 μm) to examine the organic matter content (TOC) by LECO C230 Carbon Analyzer, as well as quality and thermal maturity through HAWK pyrolysis manufactured by Wildcat Technologies.

3. Results

3.1 Areal heterogeneity of sub-decimeter-sized samples

3.1.1 Elemental distribution

The results of powder-sized samples show the average mineral compositions of the whole sample (Table 1). These results indicate that the samples used in this study are carbonate-rich with small amounts of quartz and a very small amount of pyrite & clay minerals. Therefore, in the following μ-XRF mapping test, only the elemental composition data related to the detected main minerals are presented, with tight elements selected.

In XRF images (Figs. 2-3), the higher the concentration is, the brighter the color is. Based on the mineral compositions provided by XRD results for the powder sample, Ca being detected by the μ-XRF is present only in calcite ($CaCO_3$), Fe is in pyrite (FeS_2), Si is from siliceous minerals such as quartz (SiO_2) and clay minerals, and Al, Na & K are present in clay minerals. Since the clay

minerals only account for a very small amount of the total minerals (Table 1), the Si signal will be mostly due to quartz, so the detection of Al, Na, and K is used to characterize the clay minerals distribution. Both Mg and Mn are used to reflect the potential presence of ankerite [Ca(Fe, Mg, Mn)$(CO_3)_2$] or dolomite [$CaMg(CO_3)_2$]. For both C and R samples (Figs. 2-3), strong laminations are seen for high concentrations of Ca, Si, and Fe, slight laminations are observed for Al and K, and no laminations are present for Mg, Mn, and Na. To quantify the distribution of three most abundant elements (Ca, Si, and Fe), the intensities of scanned areas are normalized to the highest intensity observed for each element (Fig. 4). In Fig. 4A, the normalized Ca distribution map of the C sample shows that Ca is rich in all scanned areas with multiple laminations across the sample. The difference in the relative intensity (RI) between higher Ca areas (yellow color, ~80% RI) and lower Ca (green color, ~60%) area is relatively small. The area with higher Ca concentrations is in the upper two-thirds of the sample, whereas the lower Ca concentrations occur in the bottom portion of one-third (Fig. 4A). The normalized Si distribution map (Fig. 4B) shows that areas with higher Si concentration are located at the sample bottom, and lower Si concentrations occur in the middle and upper regions of the sample. The normalized distribution map for Fe (Fig. 4C) shows very high intensity (~80-100% RI) at the sample bottom, but only a low intensity (~0-20% RI) for the rest of the sample.

For the normalized distribution maps of the R sample (Fig. 4D-F), the areas with higher Ca concentrations (~60-100% RI) appear in the middle of sample, while the areas with lower Ca concentrations (~0-20% RI) are located on the left and right sides (Fig. 4D). The higher concentration areas of Si (~80-100% RI) and Fe (~60%-100 RI) occur on the right-hand side (Fig. 4E-F). A comparison of these three normalized maps shows that the area with high RI for Ca also

has low concentrations of Si and Fe; similarly, the area with low Ca concentration has high Si and Fe concentrations.

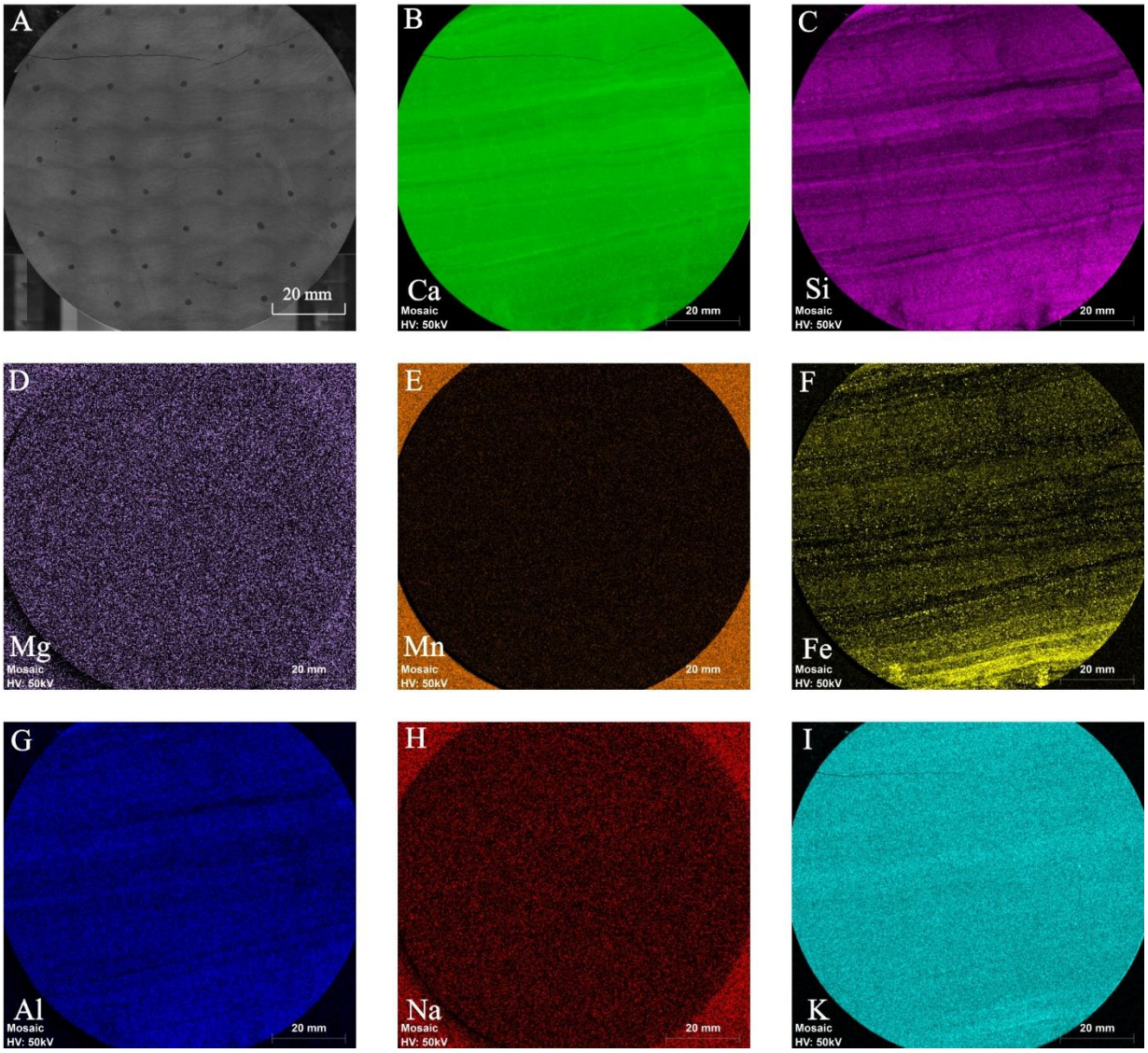

Figure 2. (A) Sample photo and (B-I) elemental distribution of Ca, Si, Mg, Mn, Fe, Al, Na, and K from μ-XRF for the circular-shaped wafer sample (Fig. 1B).

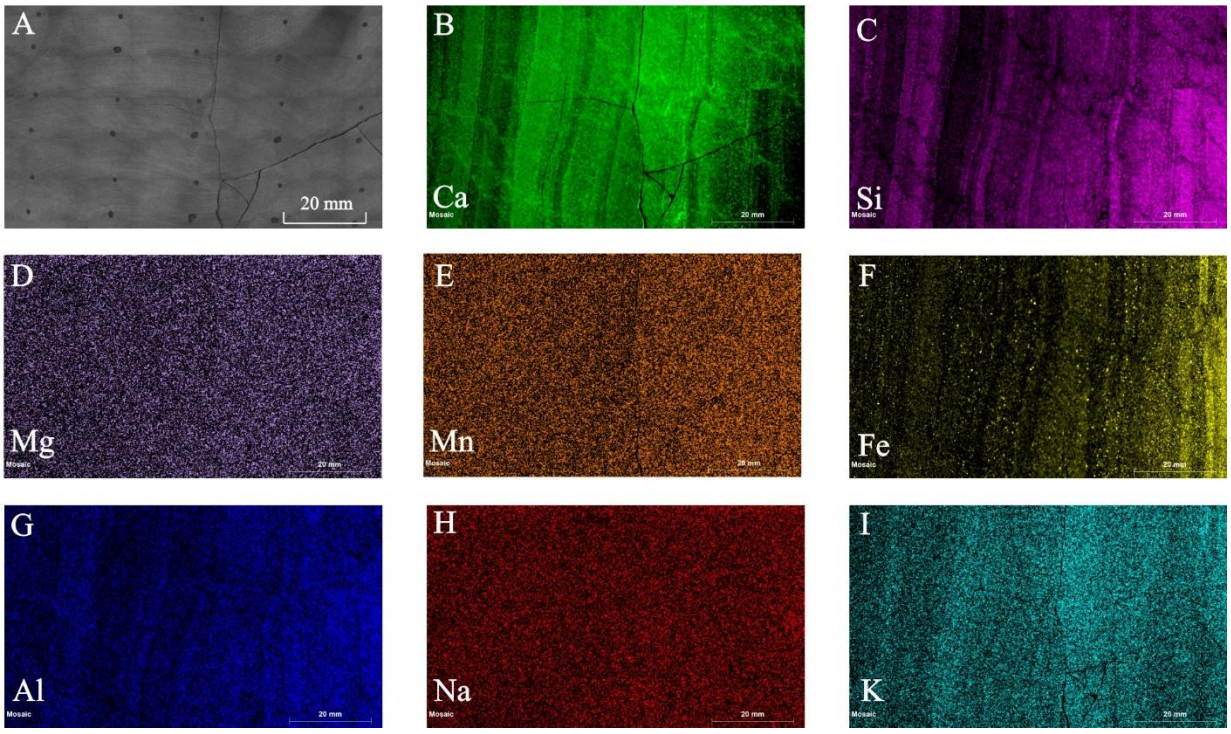

Figure 3. (A) Sample photo and (B-I) elemental distribution of Ca, Si, Mg, Mn, Fe, Al, Na, and K from μ-XRF for the rectangular-shaped wafer sample (Fig. 1C).

Once the Ca, Si, and Fe data are normalized, the sedimentary features, such as laminations and fractures, can be identified and marked on Figs. 4G and H for the C and R samples, respectively. In Fig. 4G, several fractures cut through the laminations in the C sample and offset the laminations on the right side by 3-5 μm. In the R sample (Fig. 4H), fractures cut though the laminations and lead to an offset of laminations.

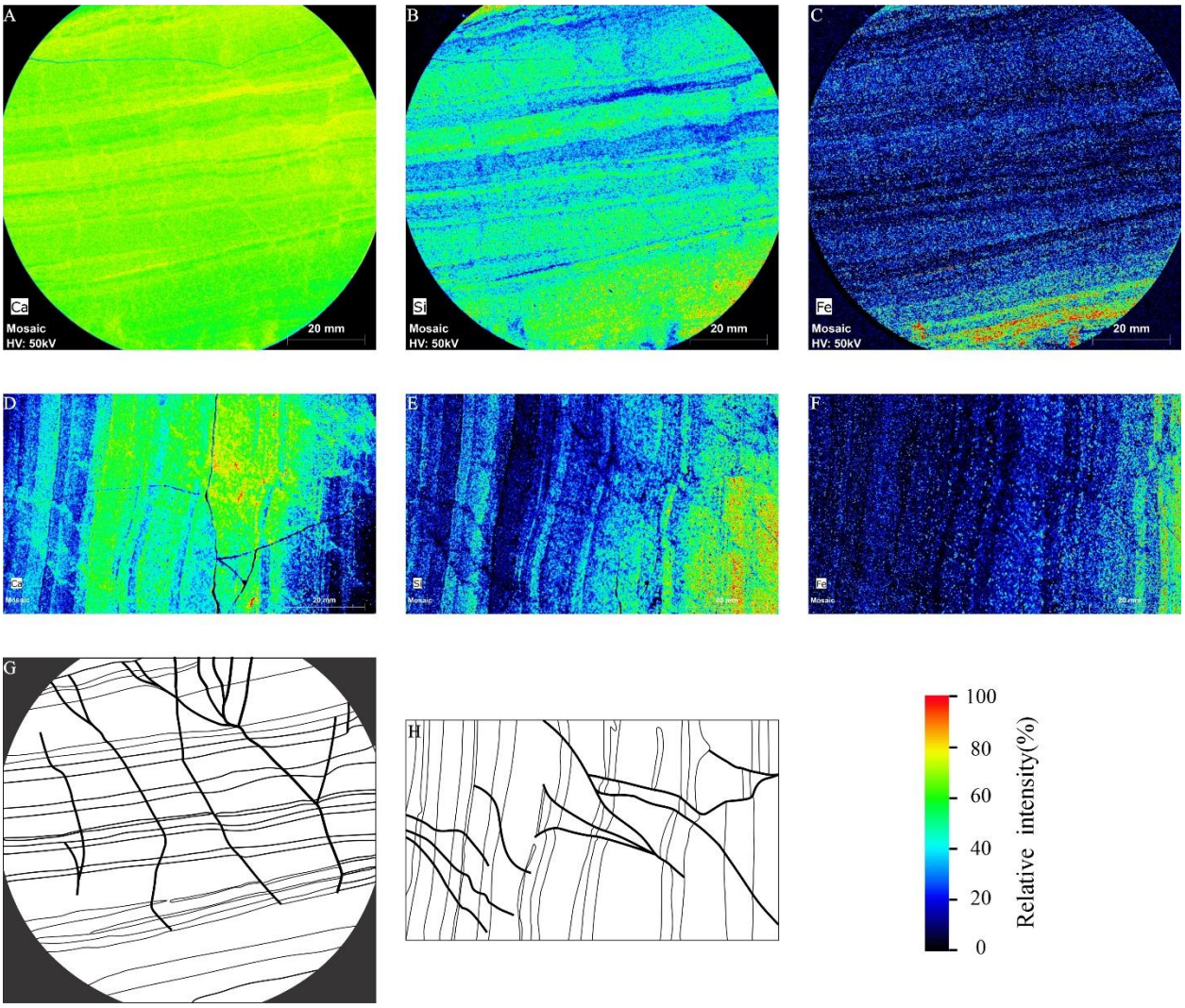

Figure 4. Elemental intensities of Ca, Si, and Fe for (A-C) Circular and (D-F) Rectangular samples as well as the interpretation of sedimentary features (G-H).

3.1.2 Sedimentary textures

Thin section petrography was carried out to determine the textural and mineral compositional changes across two C and R samples. Four positions with different Si/Ca ratios (following the normalized map in Fig. 4) on each sample were selected for petrographic microscopy (Fig. 5). Thin sections of the small rectangular areas marked as A-H in Fig. 5 are shown in Fig. 6A-H.

Under a plane-polarized light, these sub-samples show as either yellow (calcite) and brown-black color (quartz, clay, pyrite, and organic matter). Unlike other fossil-rich Eagle Ford Shale samples being collected from both wells and outcrop (Pommer and Milliken, 2015; Lehrmann et al., 2019; Reed et al., 2019; Wang et al., 2021a), fossils are only occasionally found in this sample. In the high Ca regions (A and E), the yellow color is dominant, whereas in the high Si regions (D and H), the proportion of brown-black color increases dramatically. In other thin section views cutting across Ca-Si mixed laminations (B, C, F, and G), the ratios of yellow/brown-black are intermediate. Based on the thin section petrographic observations, the samples do not show a lithological change at sub-cm scales, though there is a variation in compositions, evidenced from different ratios of yellow/black-brown colors.

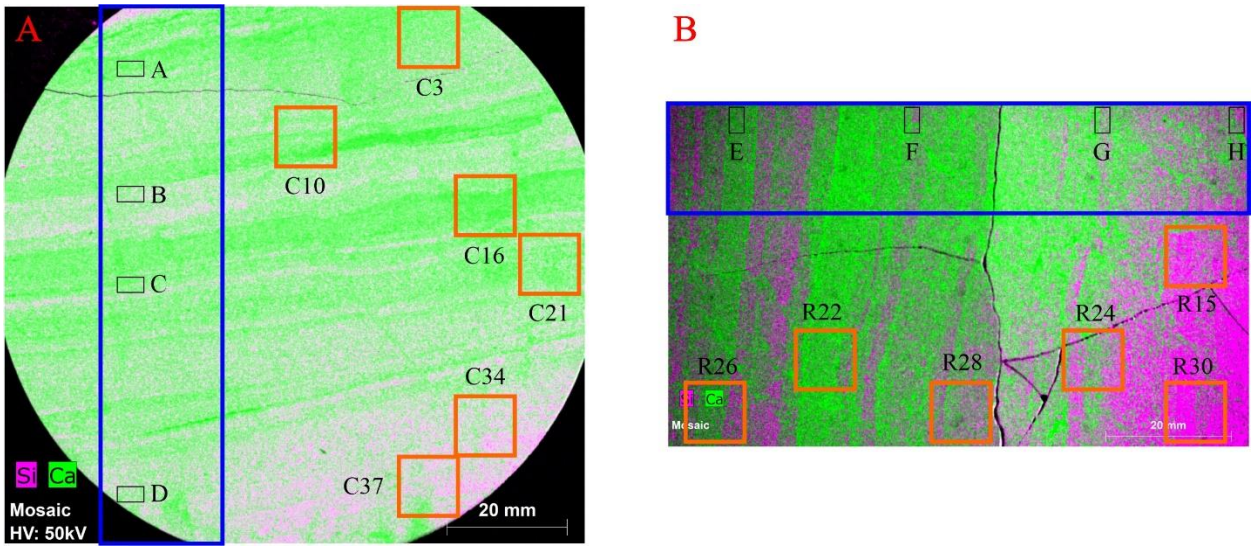

Figure 5. Sampling positions for thin-section petrography (A-H) and analyses of SEM, XRD, TOC, and pyrolysis (Fig. 1B-C).

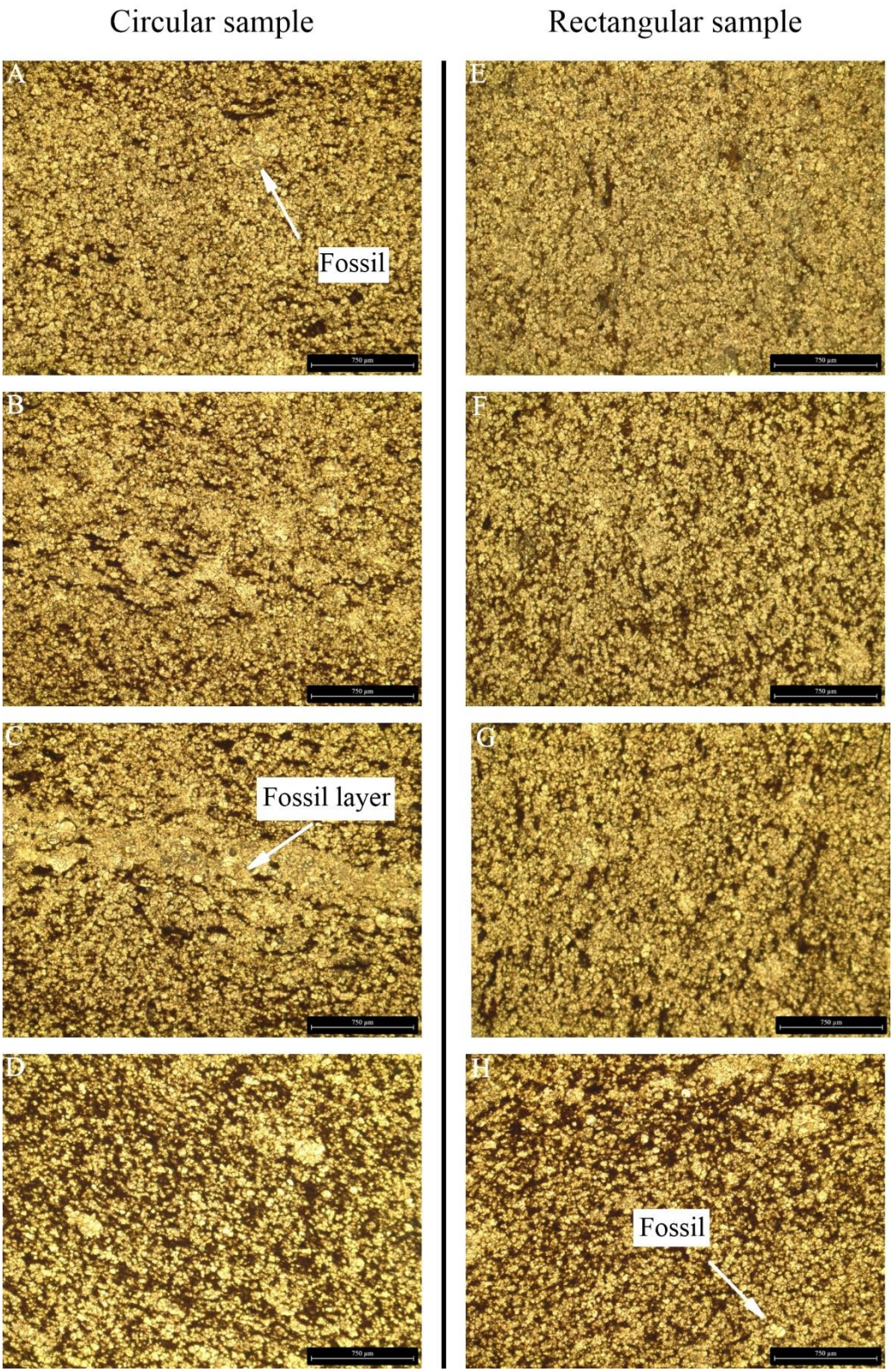

Figure 6. Thin-section petrographic photos of selected positions marked in Figure 5.

3.1.3 Pore structure

The pore structure of the C and R samples was investigated with (U)SAXS techniques. The porosity distribution and surface area for each sample are presented in Fig. 7. Overall, the porosity of the C sample ranges from 0.82 to 3.04%, with an average of 1.72±0.36% (N=132). The high porosity region is mainly located at the bottom region. The porosity of the R sample ranges from 0.93 to 2.50% and has an average of 1.61±0.35% (N=72). The high porosity region occurs at the right and bottom regions. The surface area distribution of these two samples is spatially mapped out as well from (U)SAXS data. The surface area of the C sample is 1.51-14.1 m^2/g with an average of 6.52±1.74 m^2/g (N=132), similar to the R sample of 6.89±1.52 m^2/g (N=72). While the distributions of porosity and surface area are similar, there are still some differences. For example, Positions 11 (coordinates: x=6 and y=6) and 20 (coordinates: x=4 and y=6) have the lowest porosities on the C sample, but their surface areas are not the lowest (Fig. 7 A and C). For the R sample, Positions 27 (coordinates: x=2 and y=0) and 30 (coordinates: x=8 and y=0) do not show the highest porosity, but they have the highest surface area (Fig. 7B and D)

3.2 Areal heterogeneity of selected sub-samples of large C and R samples

This section looks at the differences in mineral compositions, pore types, organic matter quantity (TOC) and quality (pyrolysis), as well as their influences on the pore size and surface area distributions. Six sub-samples (1 cm×1 cm×0.8 mm) on both C and R samples with high differences in Ca/Si intensity, porosity, and surface area were selected and cut out for XRD and SEM analyses and then crushed to powder for TOC and pyrolysis analyses. WAXS was conducted for the large-sized samples before the rock chips were cut out to validate the XRD results at different sampling scales (XRD: 1 cm × 1 cm; WAXS: 0.8 mm × 0.2 mm). For the C sample, a

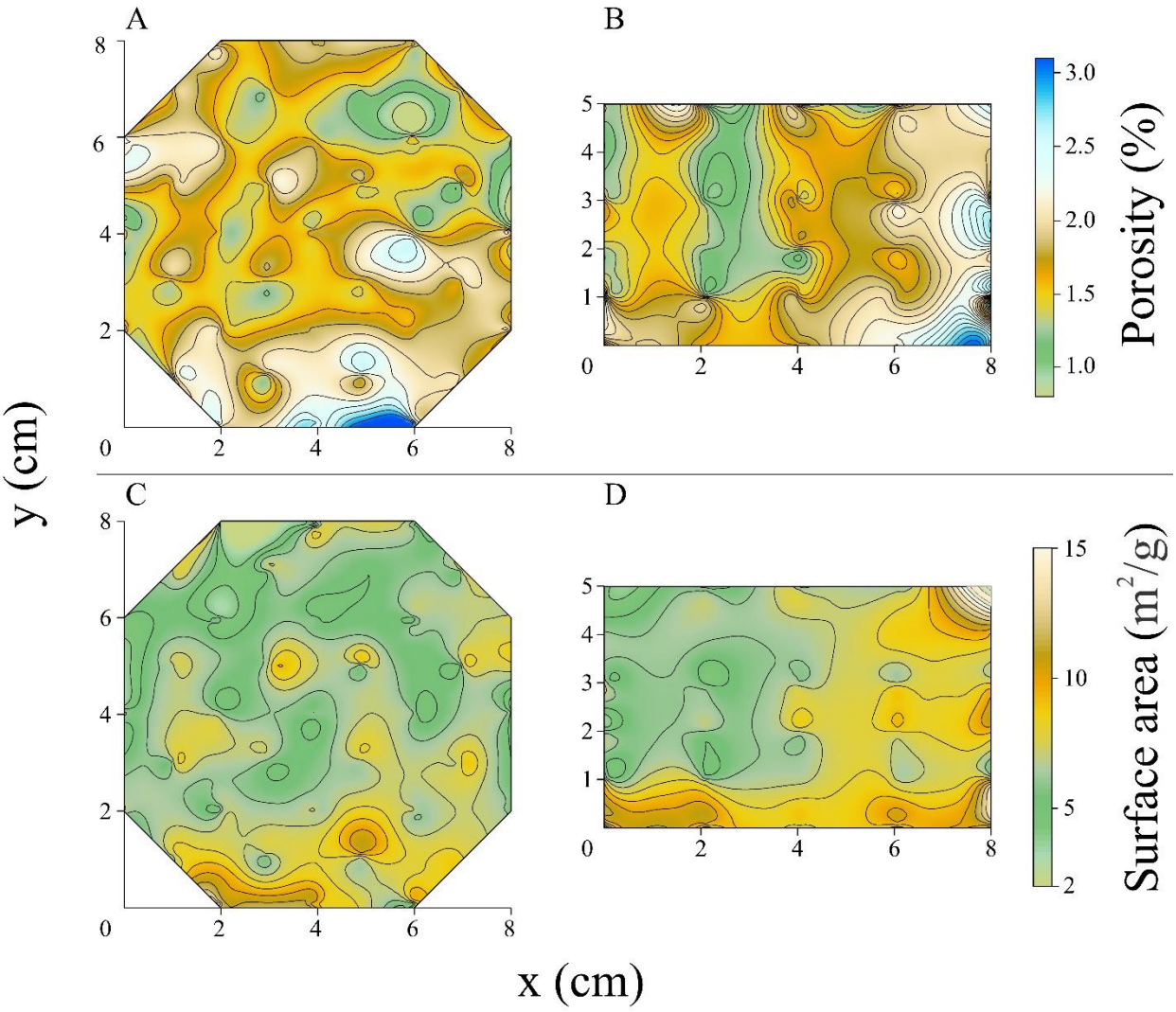

Figure 7. (U)SAXS mapping results of porosity (A-B) and surface area (C-D) distribution for Circular and Rectangular samples of Eagle Ford Shale.

total of six sub-samples were selected from Positions 3 (named C3), 10, 16, 22, 34, and 37. Similarly, six sub-samples from the R sample were chosen from Positions 15, 22, 24, 26, 28, and 30 (Fig. 5; Table 2).

3.2.1 Mineral compositions and organic matters

The results of mineral compositions, TOC, and pyrolysis of these 12 sub-samples are shown in Table 1. Due to their low abundance (0.7% from powder sample), the clay minerals are neglected during the XRD mineral composition calculation, as the calculated values for a very small amount may have a large uncertainty. C3, C10, C16, and C21 have relatively higher calcite (91.7 to 94.8 wt.%) and lower quartz (5.2 to 6.9 wt.%), whereas the C34 and C37 positions have relatively lower calcite (85.6 and 87.0 wt.%) and higher quartz (10.8 and 11.7 wt.%). Pyrite only appears in sub-samples ofC16, C21, and C37, with contents ranging from 1.3 to 3.7 wt.%. R22 and R26 show a detection of relatively low quartz (6.3 and 7.6 wt.%), high calcite (93.7 and 92.4 wt.%), and no pyrite. In contrast, R15, R24, R28, and R30 sub-samples show higher quartz (11.1-15.5 wt.%) and lower calcite (82.7-88.9 wt.%). The higher quartz rock-chips are commonly found in sub-samples with more abundant pyrite (ranging from 1.1 to 2.3 wt.%), with an exception of R28. Even though the quantification function for mineral composition from WAXS data has not been developed, its function can help to determine what types of minerals appearing in the sampling location of 0.8 mm × 0.2 mm. Results show that the higher calcite samples barely contain pyrite along with a low intensity of kaolinite and quartz (Fig. 8A and C), whereas the lower calcite samples have higher intensities of pyrite, kaolinite, and quartz (Fig. 8B and D). In addition, Table 1 shows that TOC values are higher in sub-samples with lower calcite for both R and C samples. The pyrolysis results show that all of 12 sub-samples have low values of S1 (free hydrocarbons) and S3 (CO_2 yield during pyrolysis from kerogen). Low S1 values may be due to the fact that this being an outcrop sample, and free hydrocarbons have evaporated off or been weathered away. The S2 values (mass of hydrocarbons per gram of rock generated during pyrolysis) increase with an increasing TOC content and, therefore, the hydrogen index (HI) ranges from 538 to 769. The T_{max} values (434-435

°C) from the pyrolysis are very similar as would be expected, indicating that this Eagle Ford Shale from outcrop is likely in the very early oil generation stage (Yang and Horsfield, 2020).

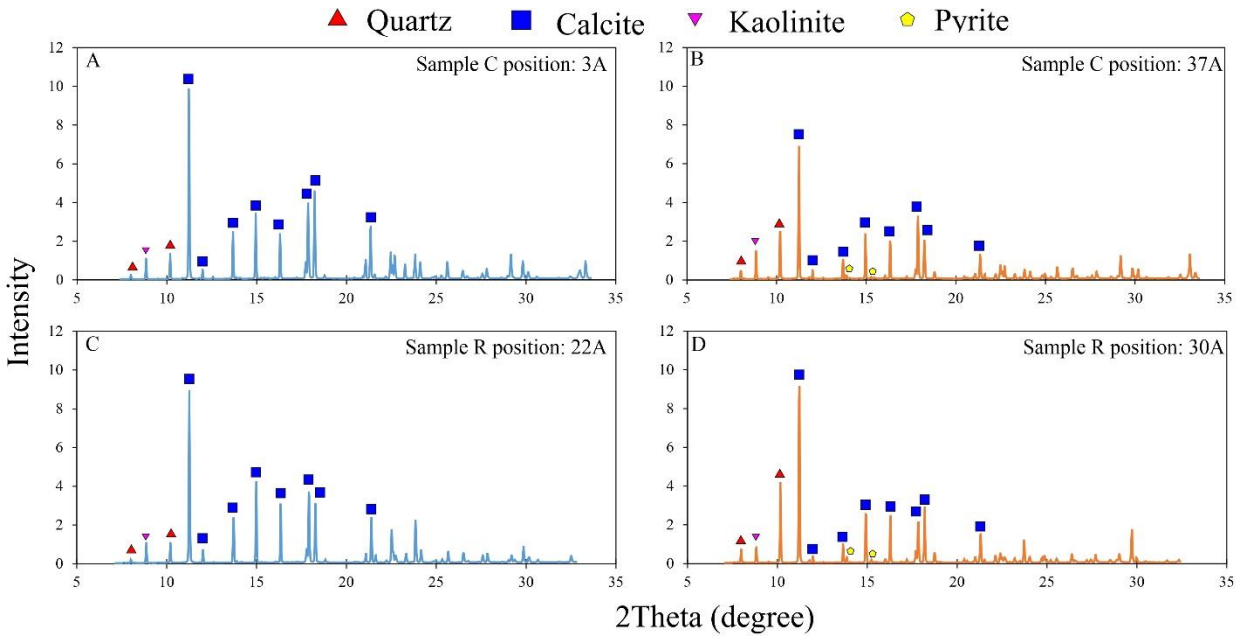

Figure 8. WAXS results for sampling positions of high calcite (A and C) and high siliceous minerals (B and D) in Circular and Rectangular samples.

3.2.2 Pore types

Fig. 9 presents the SEM images of six sub-samples taken from the C sample (shown in Fig. 5). In the higher calcite sub-samples (C3, C10, C16, and C21; Table 1), the pores are mostly interparticle between calcite and quartz (Fig. 9A, B, and D). In some parts of the solid rock matrix, there is a limited abundance of pores (Fig. 9C). In the sub-samples with lower calcite contents (C34 and C37), the pores are primarily interparticle and intraparticle in types. The interparticle pores appear between calcite, quartz, pyrite, and clay minerals, whereas the intraparticle pores are present inside pyrite framboids and clay aggregates (Fig. 9E-F and H-I). Due to its low maturity, the organic matter does not contain any pores (Fig. 9G). Similarly, Fig. 10 shows the SEM images of six sub-samples from the R sample. The higher calcite sub-samples (R22 and R26) contain dominantly

interparticle pores, and only a few pores appear in the solid matrix (Fig. 10B and D). In the lower calcite sub-samples (R15, R24, R28, and R30), pores are mainly observed between mineral crystals (Fig. 10A and G); in addition, pyrite framboids and clay aggregates can provide pore spaces (Fig. 10E, H, and I). The quartz in the SEM images is mainly secondary (formed as cement during diagenesis) with a good crystal form, indicating that it was probably from dissolved silica and precipitated as quartz cement (Fig. 9B and D; Fig 10E).

3.2.3 Pore structure

Fig. 11 shows the relationship of pore diameter with either incremental porosity or surface area of six beam spots of highest porosity in each subsample for C and R samples, whereas Table 2 gives the total porosity and surface area as well as their distributions. Pores in the C sample are dominated by diameters in the 100-1000 nm range. The higher calcite locations (C3A, C10B, C16A, and C21B; all >91%) show two major peaks in the 200-400 nm and 500-1000 nm ranges, whereas the lower calcite locations (C34A and H37A; <87%) exhibit two major peaks at 100-200 nm and 400-1000 nm. Unlike other locations, the C37A shows two peaks in the 400-1000 nm range. The surface area of all sampling locations mostly falls in the 1-10 nm range, with two main peaks located at 1-4 nm and 5-7 nm. The higher calcite beam spots (C3A, C10B, C16A, and C21B) show similar peaks in intensity and pore diameter range; on the contrary, the lower calcite C34A spot has no peaks between 5-7 nm, and rather a high peak at 10-12 nm. Furthermore, for the R sample, both higher calcite spots (R22A and R26A; >92%) and lower calcite spots (R15A, R24C, R28A, and R30A; <89%) have peaks at similar pore diameters, but they have different intensities and widths. Moreover, the incremental surface areas of six locations have similar peaks but different intensity as well (Fig. 11).

Table 1 Results of mineral composition (XRD), TOC (LECO), and pyrolysis (HAWK) for the Eagle Ford Shale sample

Sample ID	Mineral composition (wt.%)				TOC (wt.%)	Pyrolysis				
	Quartz	Calcite	Pyrite	Clays		S_1 (mg HC/g)	S_2 (mg HC/g)	S_3 (mg CO_2/g)	T_{max}(°C)	Hydrogen Index
Powder sample	7.3	91.2	0.8	0.7				N/A		
C3	6.2	93.8		nd	1.4	0.1	7.4	0.3	435	538
C10	6.1	93.9		nd	1.5	0.2	8.4	0.2	434	575
C16	5.2	94.8		nd	1.3	0.3	7.9	0.2	435	605
C21	6.9	91.6	1.6	nd	1.5	0.2	9.7	0.2	435	659
C34	10.8	85.6	3.7	nd	2.2	0.2	14.4	0.2	434	660
C37	11.7	87.0	1.3	nd	2.2	0.2	14.9	0.3	434	669
R15	14.2	84.7	1.1	nd	2.6	0.2	17.0	0.2	435	645
R22	6.3	93.7		nd	1.4	0.2	8.7	0.4	434	633
R24	13.8	84.0	2.3	nd	1.7	0.2	12.9	0.3	435	769
R26	7.6	92.4		nd	1.6	0.2	10.6	0.2	435	659
R28	11.1	88.9		nd	1.9	0.2	12.0	0.2	435	649
R30	15.1	82.7	2.2	nd	2.9	0.3	19.7	0.3	435	676

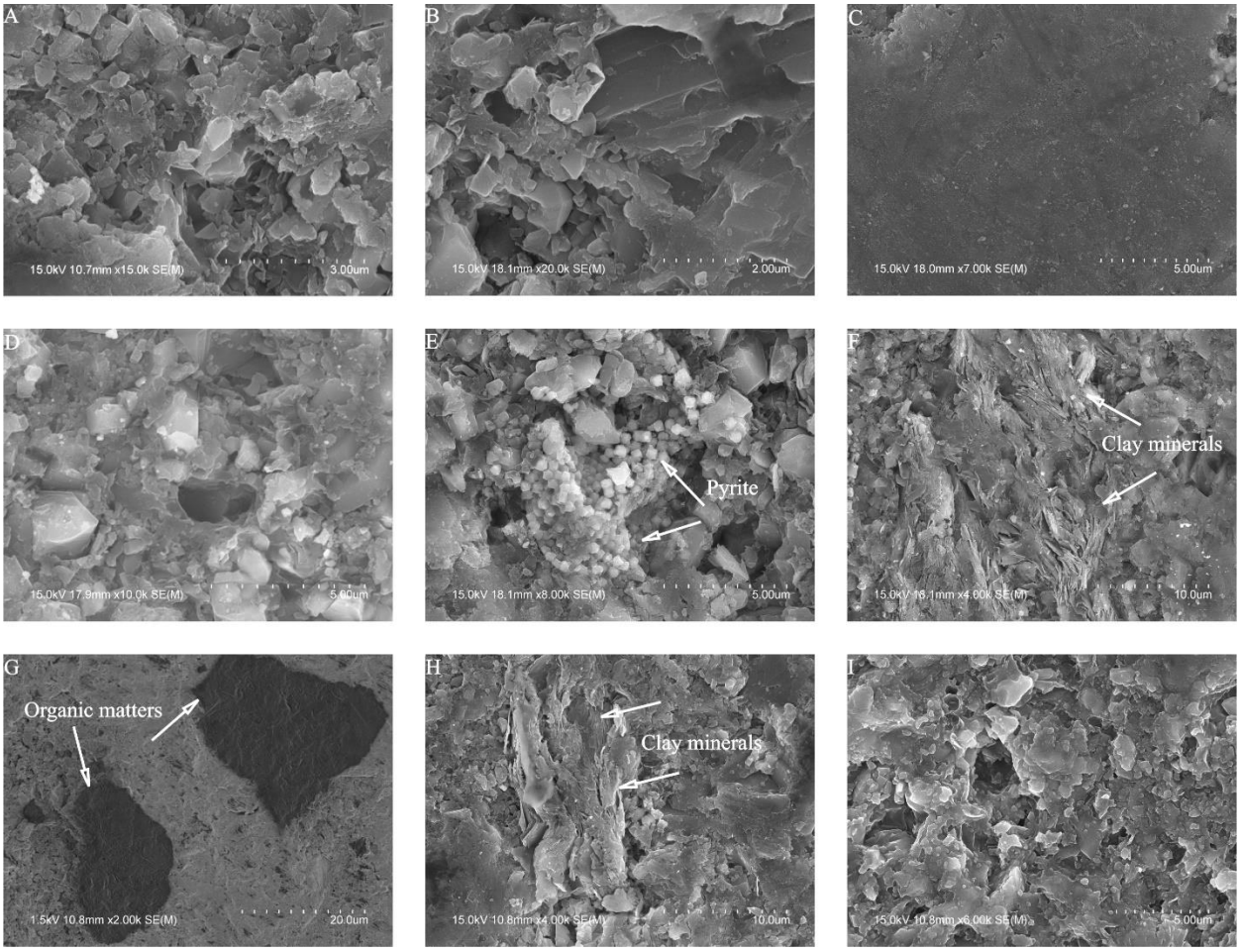

Figure 9. SEM images of the Circular sample: (A) C3, interparticle pores between minerals; (B) C10, interparticle pores and calcite matrix; (C) C16, calcite matrix; (D) C21, interparticle pores between minerals; (E) C34, pyrite; (F) C34, clay minerals and intraparticle pores; (G) C37; organic matter; (H) C37; clay minerals and intraparticle pores; and (I) C37; interparticle pores between minerals.

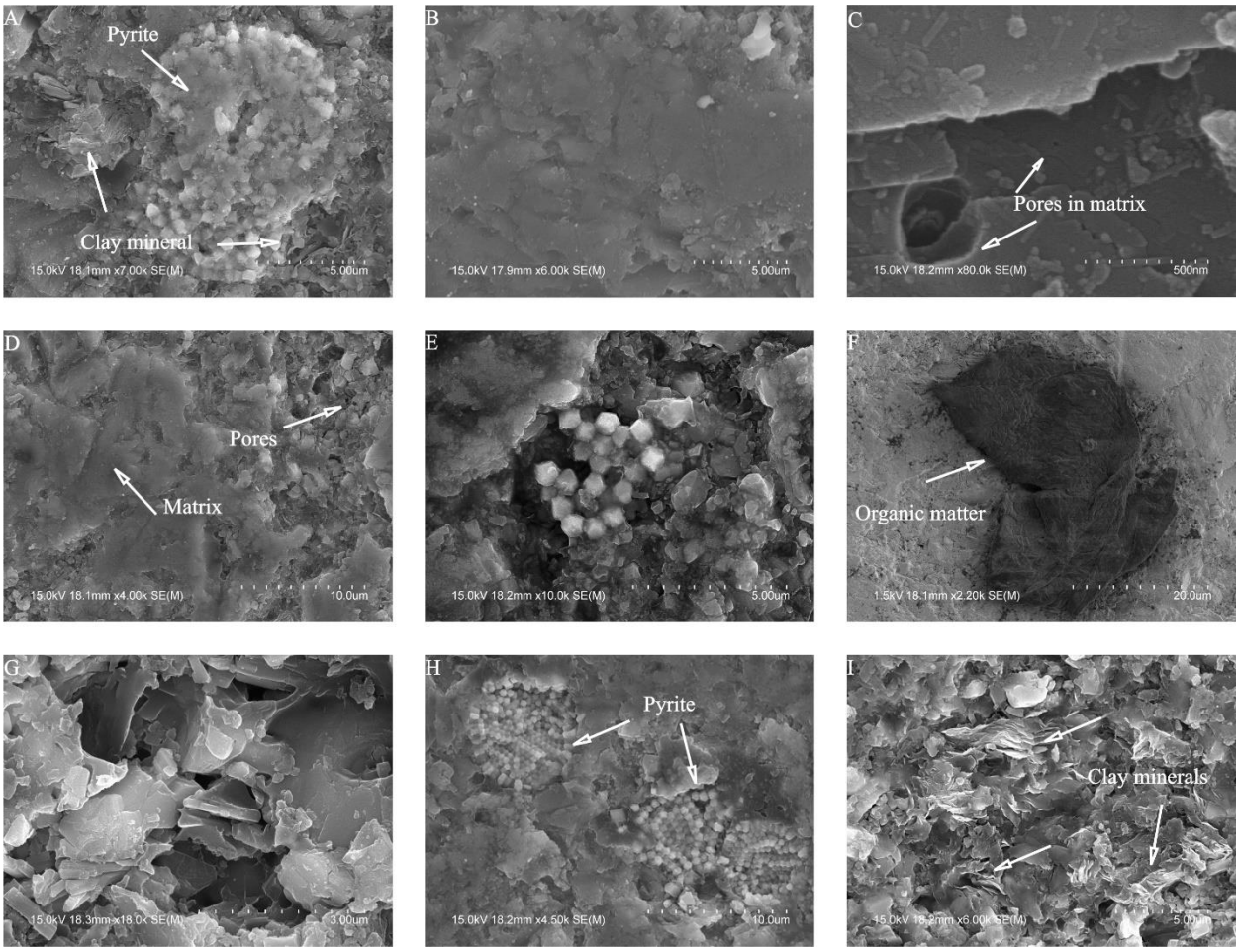

Figure 10. SEM images of the Rectangular sample: (A) R15, pyrite and clay minerals; (B) R22, pores in calcite matrix; (C) R24, interparticle pores and calcite matrix; (D) R26, interparticle pores and calcite matrix; (E) R28, pyrite; (F) R28, organic matter; (G) R28, interparticle pores; (H) R30; pyrites; and (I) R30; clay minerals.

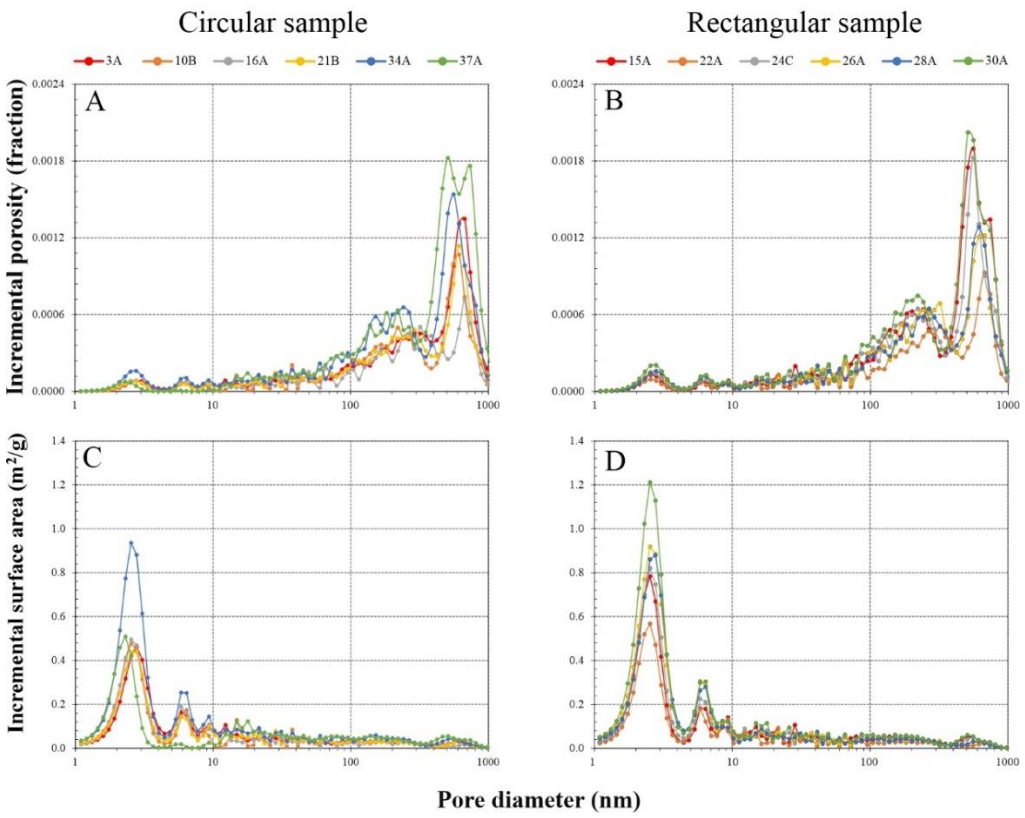

Figure 11. Comparison of porosity (A-B) and surface area (C-D) with pore diameter for six subsample locations on the Circular and Rectangular samples.

Table 2 Porosity, pore size distribution, surface area and surface area distribution data for six subsample locations in the C and R samples from (U)SAXS analyses.

Sample ID	Position ID	Porosity (%)	Pore size distribution (%)				Surface area (m^2/g)	Surface area distribution (%)			
			1-10 nm	10-50 nm	50-100 nm	100-1000 nm		1-10 nm	10-50 nm	50-100 nm	100-1000 nm
Circular (C)	3A	1.52	0.37	14.00	6.52	79.11	5.25	9.29	76.78	3.78	10.16
	10B	1.30	0.59	14.36	7.93	77.12	4.87	13.67	71.65	4.23	10.45
	16A	1.08	0.67	17.38	7.37	74.59	4.92	12.63	75.78	3.27	8.33
	21B	1.33	0.52	14.46	7.34	77.68	4.84	12.49	73.01	4.06	10.45
	34A	2.00	0.67	14.75	7.65	76.94	8.57	13.49	74.07	3.59	8.86
	37A	2.43	0.55	8.53	7.22	83.70	5.14	22.55	53.40	6.88	17.17
Rectangular (R)	15A	2.19	0.60	11.52	6.63	81.26	7.30	15.41	69.36	4.01	11.23
	22A	1.22	0.81	14.96	7.59	76.63	5.29	16.18	71.34	3.62	8.85
	24C	1.94	0.65	13.85	7.47	78.04	7.66	14.14	72.40	3.68	9.78
	26A	1.74	0.88	16.10	7.39	75.64	8.71	15.31	74.11	2.92	7.66
	28A	1.73	0.76	16.00	7.24	76.01	8.40	13.63	75.57	2.96	7.83
	30A	2.50	0.76	13.93	7.16	78.15	10.84	15.17	73.03	3.20	8.60

4 Discussions

In this study, the results of μ-XRF patterns show that the Ca abundance is inversely correlated with Si, Fe, Al, and K (Figs. 2-3) at sub-dm scales. The (U)SAXS results illustrate that the porosity and surface area vary across the whole sample area (Fig. 7). Shales are fine-grained rocks being deposited and accumulated under low-energy aqueous environments, and the depositional process of laminations is a function of the *in situ* water energy and sediment supply (O'Brien 1996; Fr´ebourg et al., 2016; Yawar and Schieber, 2017). In a similar deposition environment, the only difference between adjacent laminations is the type of sediment supply. Fig. 12 shows cross-plots of calcite from XRD vs. porosity [from (U)SAXS], surface area [from(U)SAXS], TOC (from LECO), and S2 (from pyrolysis) of 12 selected sub-samples from the C and R samples. It shows a negative relationship between calcite and porosity (correlation coefficient R^2=0.7852; N=12), surface area (R^2=0.4748), TOC (R^2=0.7358), and S2 (R^2=0.8641). This negative relationship between calcite and porosity indicates that calcite contents are inversely related to pore space. In addition to pores being observed between the mineral crystals, Louck et al. (2012) reported that pores are also presented in pyrite framboids and clay aggregates. From the XRD results and SEM images in this study, the pyrite and clay minerals are only present in the lower calcite regions. Within the pyrite framboids and clay aggregates, those intraparticle pores provide extra pore spaces and surface area in these lower calcite locations, which lead to higher porosity and surface area compared with higher-calcite spots. Reed et al. (2009) and Frebourg et al. (2016) also pointed out that the recrystallization of calcite will eliminate its original texture and the calcite overgrowth will fill the pore networks, and therefore, porosity will decrease in the higher calcite content regions. In our thin sections photos (Fig. 6 A, C, and H), the calcitic-fossils were dissolved and

reprecipitated to be with crystalline calcite and only a couple of molded fossils are visible. Therefore, in the higher calcite spots, the porosity will be expected to be lower than that in the lower calcite spots.

Many other studies also reported that the organic matter can provide a certain amount of porosity to organic matter-rich shale as a result of petroleum generation (Curtis et al., 2012; Ko et al., 2016; İnan et al., 2018; Wang et al., 2020; Bai et al., 2021). However, in this Eagle Ford Shale sample, pyrolysis results indicate that organic matter is at best in the early oil window, and SEM observations show that no pores show up within the organic matter particles. Therefore, the contribution of organic matter-hosted pores to porosity and pore surface area is negligible in this sample. Overall, for this carbonate-rich Eagle Ford Shale, the increase in siliceous minerals and pyrite will lead to high porosity and surface area. Several studies have reported that high porosity is not necessarily related to high silica content (Yang et al., 2016; Wu et al., 2019; Shu et al., 2021), but might be related to clay mineral contents (Ross and Bustin, 2008; Chen et al., 2016). Calcite also shows a weak negative relationship to the surface area, but the R^2 is only 0.4748. It's been recognized that clay minerals have a much higher surface area than calcite and quartz (Clouter et al., 2001; Michot and Villieras, 2006; Montes-Hernandez et al., 2008; Kuila and Prasad, 2013). However, our Eagle Ford Shale sample has a very limited amount of clays (less than 1%) from the XRD analyses. In addition, TOC and S2 show a good negative relationship (R^2= 0.7358 and 0.8641) with calcite. Many previous studies suggested that Fe can stimulate organic matter productivity (Tribovillard et al., 2015; Frebourg et al., 2016; Zhang et al., 2017). As with the clay minerals, however, the composition of pyrite cannot be accurately calculated due to its low abundance in this sample.

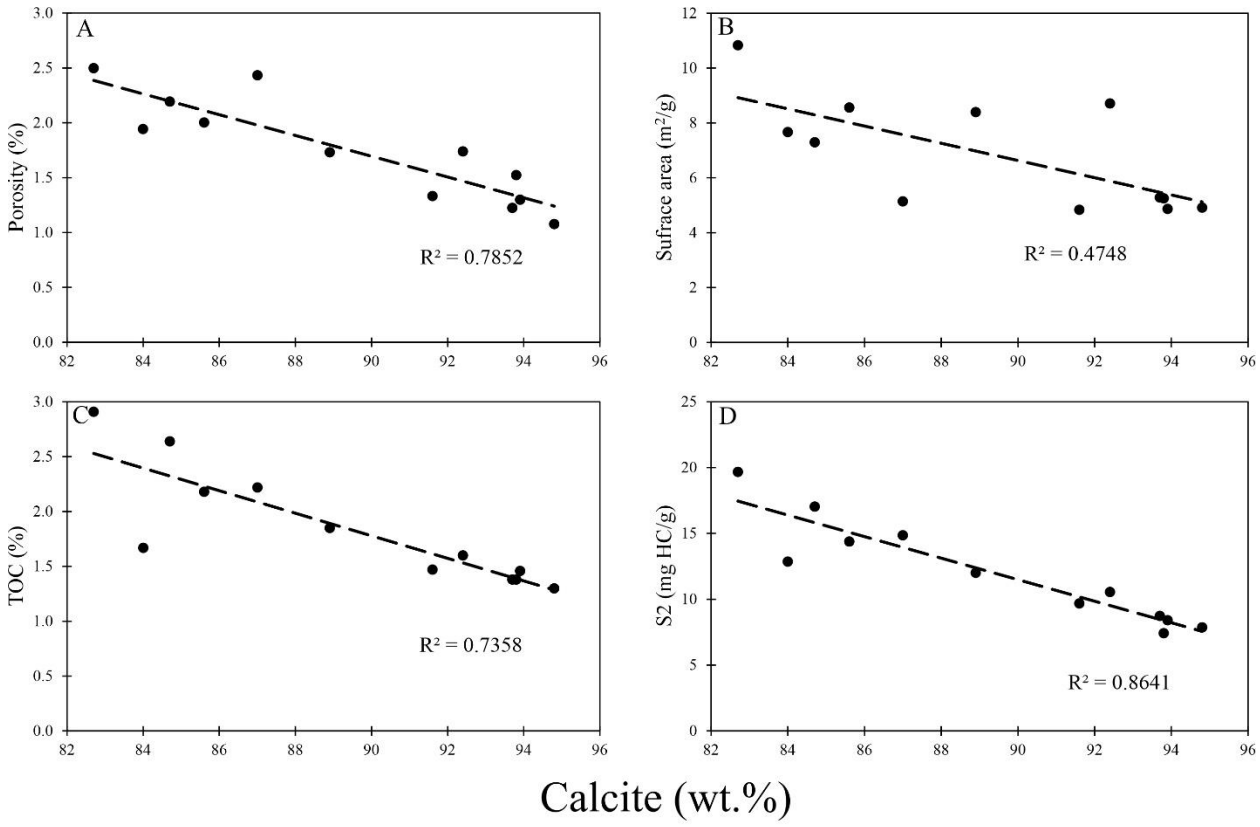

Figure 12. Relationships between calcite content (from XRD) with A: porosity [from (U)SAXS]; B: surface area [from (U)SAXS]; C: TOC (from LECO); and D: S2 (from pyrolysis).

Since the cross-plot of calcite and porosity shows a good correlation (R^2=-0.7852), the Ca signals on the μXRF maps can be directly correlated to the porosity. Based on the normalized Ca intensity data, the porosity of each lamination can be calculated and shown in Fig. 4G and H. Therefore, the sedimentary textures map (Fig. 4G and H) can be filled with calculated porosity of each lamination to generate a porosity-lamination map to reflect the porosity changes among laminations (Fig. 13). Although the porosity does not show a large change within the same lamination, the fractures often related to local tectonic activities can offset the lamination and lead to porosity variation. The local tectonic movement will stimulate the generation of fractures which can offset with? a lamination by micrometers to a meter (at scales larger than meters, the fracture is called a fault). In this Eagle

Ford sample, the lamination offset is limited to μm-mm scales, and it will not impact porosity measurements at the 2.5 cm-diameter core plug scale, but will affect petrophysical analyses at sample sizes at sub-mm scales (e.g., 100s μm used for gas physisorption, a common approach to determining pore size distribution). However, other studies (Gillen et al., 2019; Zhang et al., 2019; Xu et al., 2020) reported that some lamination offsets can be at the cm-m scale; this large-scale offset will lead to variable results from two cores which are distanced at meters apart.

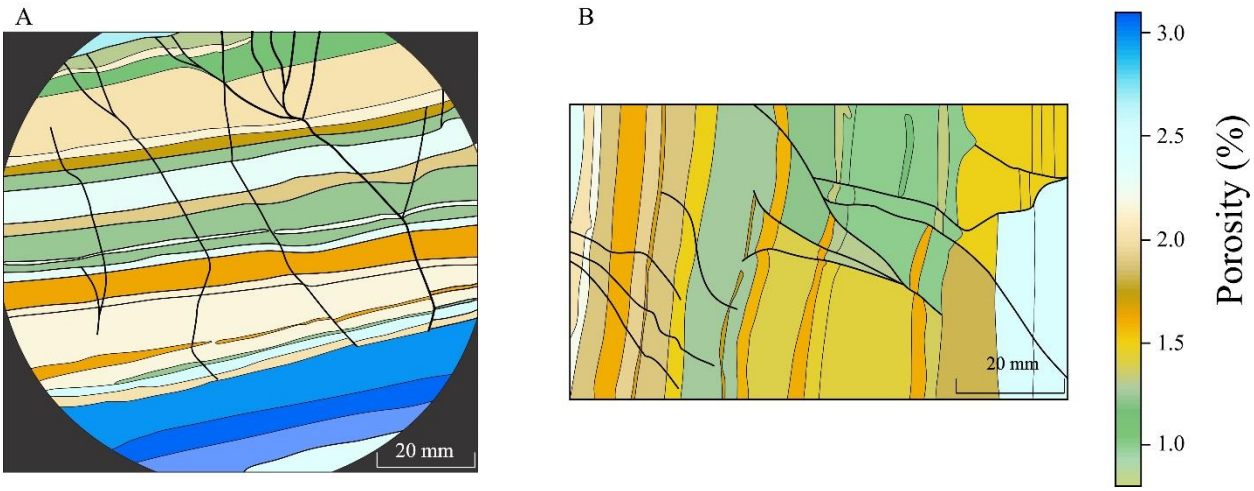

Figure 13. Sub-decimeter-scale areal heterogeneity of porosity distribution and sedimentary features for (A) Circular and (B) Rectangular samples.

5. Conclusions

This study investigates the areal heterogeneity of mineral compositions, pore structure, and organic matter composition on two sub-dm-sized samples from an outcrop of Eagle Ford Shale. Even though it is not visible to the naked eye, the spatial heterogeneity can be observed across the whole sample area with the help of μ-XRF and (U)SAXS. Based on the relationship between compositions and measured porosity from (U)SAXS, the porosity at other non-measured locations can be extrapolated; and the sedimentary-textural maps can be associated with calculated porosity.

The capabilities of quickly and non-destructively analyzing dm-scaled samples and providing good resolutions of μm to cm of those two techniques for areal heterogeneity studies open up a wide range of potential applications to many geological fields such as mineralogy, petrology, sedimentary geology, environmental geology, energy geology, and astrogeology.

Acknowledgment

We thank the financial support from the Nuclear Energy University Program managed by the Office of Nuclear Energy at U.S. Department of Energy (award number DE-NE0008797), the AAPG Grants-in-Aid program (John H. and Colleen Silcox Named Grant in 2021), and Japan Atomic Energy Agency. The X-ray scattering data were collected at the X-ray Science Division beamline of 9-ID, a resource of the Advanced Photon Source, a U.S. Department of Energy (DOE) Office of Science User Facility operated for the DOE Office of Science by Argonne National Laboratory under Contract No. DE-AC02-06CH11357. All data presented in this work will be placed into a repository managed by Mavs Dataverse of the University of Texas at Arlington and are also available on request (maxhu@uta.edu).

References

Alnahwi, A., Loucks, R, G., 2018. Mineralogical composition and total organic carbon quantification using x-ray fluorescence data from the Upper Cretaceous Eagle Ford Group in southern Texas. AAPG Bulletin, 103, 12, 2891-2907.

Bai, L., Liu, B., Du, Y., Wang, B., Tian, S., Wang, L., Xue, Z., 2021. Distribution characteristics and oil mobility thresholds in lacustrine shale reservoir: Insights from N2 adsorption experiments on samples prior to and following hydrocarbon extraction. Petroleum Science, in press, https://doi.org/10.1016/j.petsci.2021.10.018.

Barker, R, D., Barker, S, L, L., Wilson, S, A., Srock, E, D., 2020a. Quantitative mineral mapping of drill core surfaces I: A method for μXRF mineral calculation and mapping of hydrothermally

altered, fine-grained sedimentary Rocks from a Carlin-type gold deposit. Economic Geology, 116, 4, 803-819.

Barker, R, D., Barker, S, L, L., Cracknell, M, J., Srock, E, D., Holmes, G., 2020b. Quantitative mineral mapping of drill core surfaces I: Long-wave infrared mineral characterization using μXRF and machine learning. Economic Geology, 116, 4, 821-836.

Birdwell, J, E., Draves, C., Kemeny, G., Whaley, S., Wilson, S, A., 2019. Application of multiple hyperspectral imaging tools to the examination of submillimeter variability in geochemical reference materials from major, U.S. shale plays. Processing of AAPG Annual Convention and Exhibition, San Antonio, Texas, May 19-22, Search and Discovery Article #90350.

Borrok, D, M., Yang, W., Wei, M., Mokhtari, M., 2019. Heterogeneity of the mineral and organic content of the Tuscaloosa Marine Shale. Marine and Petroleum Geology, 109, 717, 731.

Bourdet, J, F, R., Stalker, L., Hortle, A, L., Ryan, C, R., 2020. Tracking mercury contaminant in the subsurface. Processing of Offshore Technology Conference, Kuala Lumpur, Malaysia, August 17-19. Paper #: OTC-30395-MS.

Breyer, J., Wilty, R, H., Tian, Y., Salman, A., O'Connor, K, W., Kurtoglu, B., Hooper, R. J., Daniels, R, M., Bulter, R, W., Alfred, D., 2015. Limestone frequency and well performance, Eagle Ford Shale (Cretaceous), South Texas, Search and Discovery Article #51091.

Chen, S., Han, Y., Fu, C., Zhang, H., Zhu, Y., Zuo, Z., 2016. Micro and nano-size pores of clay minerals in shale reservoirs: Implication for the accumulation of shale gas. Sedimentary Geology, 342, 180-190.

Clouter, A., Brown, D., Hohr, D., Borm, P., Donaldson, K., 2001. Inflammatory effects of respirable quartz collected in workplaces versus standard DQ12 quartz: Particle surface correlates. Toxicological Sciences, 63, 90-98.

Curtis, M, E., Cardott, B, J., Sondergeld, C, H., Rai, C, S., 2012. Development of organic porosity in the Woodford Shale with increasing thermal maturity. International Journal of Coal Geology, 103, 26-31.

Frebourg, G., Ruppel, S, C., Loucks, R, G., Lambert, J., 2016. Depositional controls on sediment body architecture in the Eagle Ford/Boquillas system: Insight from outcrops in west Texas, United States. AAPG Bulletin, 100, 4, 657-682.

Gillen, K., Wood, J, M., Sharp, L., Grimison, T., Guerard, B., 2019. Natural and induced structural fabrics in drill-cores from the Montney Formation, western Canada. Processing of William C. Gussow Geoscience Conference, Banff, Canada, October 15-17.

Hu, Q.H., Ewing, R.P., Rowe, H.D., 2015. Low nanopore connectivity limits gas production in Barnett Formation. Journal of Geophysical Research – Solid Earth, 120, 12, 8073–8087.

Huang, B., Li, L., Tan, Y., Hu, R., Li., 2020. Investigating the meso-mechanical anisotropy and fracture surface roughness of continental shale. Journal of Geophysical Research – Solid Earth, 125, e2019JB017828.

Ilavsky, J., Jemian, P., 2009. *Irena*, tool suite for modeling and analysis of small-angle scattering. Journal of Applied Crystallography, 42, 347-353.

Ilavsky, J., Zhang, F., Andrews, R. N., Kuzmenko, I., Jemian, P. R., Levine, L. E., Allen, A. J., 2018. Development of combine microstructure and structure characterization facility for in situ and operando studies at the Advanced Photon Source. Journal of Applied Crystallography, 51, 867-882.

İnan, S., Badairy, H, A., İnan, T., Zahrani, A, A., 2018. Formation and occurrence of organic matter-hosted porosity in shales. International Journal of Coal Geology, 199, 39-51.

Ko, L, T., Loucks, R, G., Zhang T., Ruppel, S, C., Shao, D., 2016. Pore and pore network evolution of Upper Cretaceous Boquillas (Eagle Ford-equivalent) mudrocks: Results from gold tube pyrolysis experiments. AAPG Bulletin, 100, 11, 1693-1722.

Kuila, U., Prasad, M., 2013. Specific surface area and pore-size distribution in clays and shales. Geophysical Prospecting, 61, 341-362.

Lehrmann, D, J., Yang, W., Sickmann, Z, T., Ferrill, D, A., McGinnis, R, N., Morris, A, P., Smart, K, J., Gulliver, K, D. H., 2019. Controls on sedimentation and cyclicity of the Boquillas and equivalent Eagle Ford formation from detailed outcrop studies of western and central Texas, U.S.A. Journal of Sedimentary Research, 89, 629-653.

Loucks, R, G., Reed, R, M., Ruppel, S, C., Hammes, U., 2012. Spectrum of pore types and networks in mudrocks and a descriptive classification for matrix-related mudrock pores. AAPG Bulletin, 96, 6, 1071-1098.

Ma, L., Dowey, P, J., Rutter, E., Taylor, K, G., Lee, P, D., 2019. A novel upscaling procedure for characterizing heterogeneous shale porosity from nanometer to millimetre-scale in 3D. Energy, 181, 1285-1297.

Michot, L, J., Villieras, F., 2006. Surface area and porosity. Developments in Clay Science, 1, 965-978.

Mighani, S., Bernabe, Y., Boulenouar, A., Mok, U., Evans, B., 2019. Creep deformation in Vaca Muerta Shale form nanoindentation to triaxial experiments. Journal of Geophysical Research – Solid Earth, 124, 7842-7868.

Montes-Hernandez, G., Fernandez-Martinez, A., Charlet, L., Tisserand, D., Renard, F., 2008. Textural properties of synthetic nano-calcite produced by hydrothermal carbonation of calcium hydroxide. Journal of Crystal Growth, 310,2946-2953.

Nikonow, W., Rammlmair, D, 2016. Risk and benefit of diffraction in energy dispersive X-ray fluorescence mapping. Spectrochimica Acta Part B, 125, 120-126.

O'Brien, N, R., 1996. Shale lamination and sedimentary processes. Geological Society, Special Publications, 116, 1, 23-36.

Peng, S., Xiao, X., 2017. Investigation of multiphase fluid imbibition in shale through synchrotron-based dynamic micro-CT imaging. Journal of Geophysical Research – Solid Earth, 122, 4475-4491.

Pommer, M., Milliken, K., 2015. Pore type and pore size distribution across thermal maturity, Eagle Ford Formation, Southern Texas. AAPG Bulletin, 99, 9, 1713-1744.

Reed, R, M., Sivil, J, E., Sun, X., Ruppel, S, C., 2019. Heterogeneity of microscale lithology and pore systems in an Upper Cretaceous Eagle Ford Group circular core, South Texas, U.S.A. GCAGS Journal, 8, 22-34.

Ross, D, J, K., Bustin, R, M., 2008. Characterizing the shale gas resource potential of Devonian-Mississippian strata in the Western Canada sedimentary basin: Application of an integrated formation evaluation. AAPG Bulletin, 92, 1, 87-125.

Shu, Y., Lu, Y., Hu, Q., Wang, C., Wang, Q., 2019. Geochemical, petrographic and reservoir characteristics of the transgressive systems tract of lower Silurian black shale in Jiaoshiba area, southwest China. Marine and Petroleum Geology, 129, 105014.

Tribovillard, N., Hatem, E., Averbuch, O., Barbecot, F., Bout-Roumazeilles, V., Trentesaus, A., 2015. Iron availability as a dominant control on the primary composition and diagenetic overprint of organic-matter-rich rocks. Chemical Geology, 401, 67-82.

U.S. Energy Information Administration, 2022. Drilling productivity report. Department of Energy, Washington, D.C., Accessible at https://www.eia.gov/petroleum/drilling/

Wang, Q., Hu, Q., Larsen, C., Zhao, C., Sun, M., Zhang, Y., Zhang, T., 2021a. Microfracture-pore structure characterization and water-rock interaction in three lithofacies of the lower Eagle Ford Formation. Engineering Geology, 292, 106276.

Wang, Q., Hu, Q., Ning, X., Ilavsky, J., Kuzmenko, I., Tom, T., 2021b. Spatial heterogeneity analyses of pore structure and mineral composition of Barnett Shale using X-ray scattering techniques. Marine and Petroleum Geology, 134, 105354.

Wang, Y., Liu, L., Hu, Q., Hao, L., Wang, X., Sheng, Y., 2020. Nanoscale pore network evolution of Xiamaling Marine Shale during organic matter maturation by hydrous pyrolysis. Energy & Fuels, 34, 1548-1563.

Wu, S., Yang, Z., Zhai, X., Cui, J., Bai, L., Pan, S., Cui, J., 2019. An experimental study of organic matter, minerals and porosity evolution in shales within high-temperature and high-pressure constraints. Marine and Petroleum Geology, 102, 377-390.

Xu, S., Gou, Q., Hao, F., Zhang, B., Shu, Z., Zhang, Y., 2020. Multiscale faults and fractures characterization and their effects on shale gas accumulation in the Jiaoshiba area, Sichuan Basin, China. Journal of Petroleum Science and Engineering, 189, 107026.

Yang, S., Horsfield, B., 2020. Critical review of the uncertainty of T_{max} in revealing the thermal maturity of organic matter in sedimentary rocks. International Journal of Coal Geology, 225, 103500.

Yang, R., He, S., Yi, J., Hu, Q., 2016. Nano-scale pore structure and fractal dimension of organic-rich Wufeng-Longmaxi shale from Jiaoshiba area, Sichuan Basin: Investigations using FE-SEM, gas adsorption and helium pycnometry. Marine and Petroleum Geology, 70, 27-45.

Yawar, Z., Schieber, J., 2017. On the origin of silt laminae in laminated shales. Sedimentary Geology, 360, 22-34.

Zhang, J., Zeng, Y., Slatt, R., 2019. XRF (X-ray fluorescence) applied to characterization of unconventional Woodford Shale (Devonian, U.S.A.) lateral well heterogeneity. Fuel, 254, 115565.

Zhang, W., Yang, W., Xie, L., 2017. Controls on organic matter accumulation in the Triassic Chang 7 lacustrine shale of the Ordos Basin, central China. International Journal of Coal Geology, 183, 38-51.

Zhang, X., Shi, W., Hu, Q., Zhai, G., Wang, R., Xu, X., Xu, Z., Meng, F., Liu, Y., 2019. Pressure-dependent fracture permeability of marine shales in the Northeast Yunnan area, Southern China. International Journal of Coal Geology, 214, 103237.

CHAPTER IV

Spontaneous water imbibition and vapor sorption into various sedimentary rocks across Texas and Oklahoma, USA

Qiming Wang[a], Qinhong Hu[a,*], Chen Zhao[a], Xiaoming Zhang[a,b], Tao Zhang[a], and Xiang Lin[a,c],

[a] Department of Earth and Environmental Sciences, the University of Texas at Arlington, TX 76019, USA

b School of Earth Resources, China University of Geosciences, Wuhan 430074, China

c School of Environmental Studies, China University of Geosciences, Wuhan 430074, China

Prepared for: Energy & Fuels

[*] Corresponding author: maxhu@uta.edu

Key words: spontaneous imbibition, water vapor sorption, pore structure, pore connectivity, sedimentary rocks

Abstract

As sedimentary rock formations are involved in many energy, environmental, and geological fields, its pore structure plays a significant role in impacting fluid flow behavior and how they can be utilized. This work studied 12 typical sedimentary rocks, across Texas and Oklahoma, with various lithologies such as sandstones, carbonate rocks, and shale to investigate their pore structure by water immersion porosimetry (WIP), mercury intrusion porosimetry (MIP), and spontaneous imbibition and water vapor sorption. In addition, X-ray diffraction (XRD) and contact angle methods are used to determine the mineral compositions and wettability. MIP results show that the pore-throat diameters of sandstone and carbonate rocks are relatively simple, with major ones controlling more than 75% of the total pore volume. Shale samples have a more complex pore structure that the pore-throat sizes appear in a broad nm-μm range and nm-sized pore-throats are more than μm sized ones in terms of total pore volume. According to the spontaneous imbibition studied in the directions of both transverse and parallel to the bedding plane, directional pore connectivity is accessed. Most sandstone and carbonate rock samples show high to intermediate pore connectivity, and do not exhibit pore connectivity differences in two directions. Shale samples overall show intermediate to low pore connectivity and higher pore connectivity in the direction of being parallel than transverse. Compared with spontaneous imbibition water uptake with sample-liquid contact, water vapor sorption tests suggest that it can contribute as high as 65.6% of water uptake in the initial dry condition for shale. As the influencing factors on fluid flow in porous media, porosity, pore-throat diameter distribution, pore connectivity, wettability, and clay minerals exert the impact differently, and this study points out that the pore connectivity is one of the most important factors often being ignored.

1. Introduction

Fluid flow and mass transport in porous and fractured media are critical processes in energy and environmental stewardship, such as oil and gas recovery, CO_2 sequestration, contaminant remediation, and geological disposal of radioactive wastes. On the one hand, as the fluid flows through the fractured rocks to preferentially percolate along with the pre-existing fractures, some fluids may be imbibed into the neighboring partially-saturated rock matrix (Hu et al., 2001) and can even occasionally create damage to rocks such as the swelling of expansive clays (Dehghanpour et al., 2012; Stavropoulou et al., 2020). On the other hand, liquid and water vapor in geological reservoirs influence the petroleum production (Yang et al., 2020; 2021). Along with the shale revolution starting from the first decade of the 21st century, spontaneous liquid imbibition and water vapor adsorption in low permeability rocks attract more attention (Dehghanpour et al., 2012; Hu et al., 2012; Cai et al., 2014; Stavropoulou et al., 2020).

Sedimentary rocks such as sandstone, carbonate rock, and shale are the major targets of groundwater banking, geothermal energy exploitation, petroleum production, and CO_2 sequestration, and disposal of radioactive wastes, and attract wide attestations on the pore structure (e.g., porosity, pore-throat size distribution, and pore connectivity) and fluid flow (e.g., permeability, capillary pressure, uptake and retention) studies (e.g., Cant et al., 2018; Yang et al., 2019a; Hu et al., 2020; Seyyedi et al., 2020; Wang et al., 2021a). Compared to porosity and pore-throat size distribution, although it has been reported in some studies, how pore connectivity in the direction of transverse and parallel to the laminations will impact fluid uptake and flow has not been well studied and understood (Hu et al., 2012; Gao and Hu, 2016).

Sandstones are usually considered well-connected rocks with high permeability in all the directions; however, the tight sandstone is less well connected and has a lower permeability

(Mostaghimi et al; 2013; Lai et al., 2018). The pore structure of carbonate rock is more various, and it is more related to its compaction, dissolution, and recrystallization which all will change its original pore structure (Moore and Druckman, 1981; Mazzullo et al., 2004). Shale is even worse. It has been reported to have more complex pore structures such as high spatial heterogeneity in terms of porosity distribution, nm-sized pore-throat size distribution, and pore connectivity heterogeneity in the direction of transverse and parallel to the bedding plane (Gao and Hu, 2016; Wang et al., 2021b). The heterogeneity can lead to permeability differences in a degree of more than ten times (Pan et al., 2015). Therefore, it is critical to experimentally characterize the pore connectivity of rocks cost-effectively in a short duration of testing time. The 1-D spontaneous imbibition is a quick and cost-effective way to determining the pore connectivity of various rock samples, as validated by many studies of natural rocks (Hu et al., 2012; 2015; Gao and Hu, 2016; Kibria et al., 2018; Sun et al., 2019; Wang et al., 2021c; 2021d). However, those studies more likely focus on wettability-related pore connectivity determination and often ignore the imbibition direction of samples, which could lead to incorrect interpretations and predictions of fluid flow. In addition, the spontaneous imbibition is a multi-factors-controlled process, the influencing factors such as wettability, pore structures, and vapor sorption will need to be considered.

In this study, a total of sedimentary rocks with different lithologies are included to test water spontaneous imbibition and water vapor adsorption in the direction of transverse and parallel to the bedding plane on cubes-shaped rock samples to investigate the pore connectivity and water flow behavior in both liquid and vapor phases. Analyses of X-ray diffraction (XRD), contact angle, and mercury intrusion porosimetry (MIP) were also conducted to access the mineral composition, wettability, and pore structure; these supplementary information will be used to evaluate the controlling factors on different fluid flow behaviors. This work will extend the understanding of

pore connectivity assessment in the typical natural sedimentary rocks and liquid/vapor water uptake tests and provide a feasible workflow for other types of rocks such as igneous and metamorphic rocks.

2 Methods

2.1 Materials

A group of outcrop sedimentary rocks across the states of Texas and Oklahoma was collected to include five carbonate rocks, two sandstones, and five shales (Figure 1; Table 1). Samples were cut to be 1 cm×1 cm×0.5 cm thin slab for contact angle, 1 cm×1 cm×1 cm cubes for MIP, and 2 cm×2 cm×2 cm cubes for spontaneous imbibition and water vapor sorption tests. The rest of the rock fragments were crushed by mortar and pestle to be >200 mesh for XRD analyses.

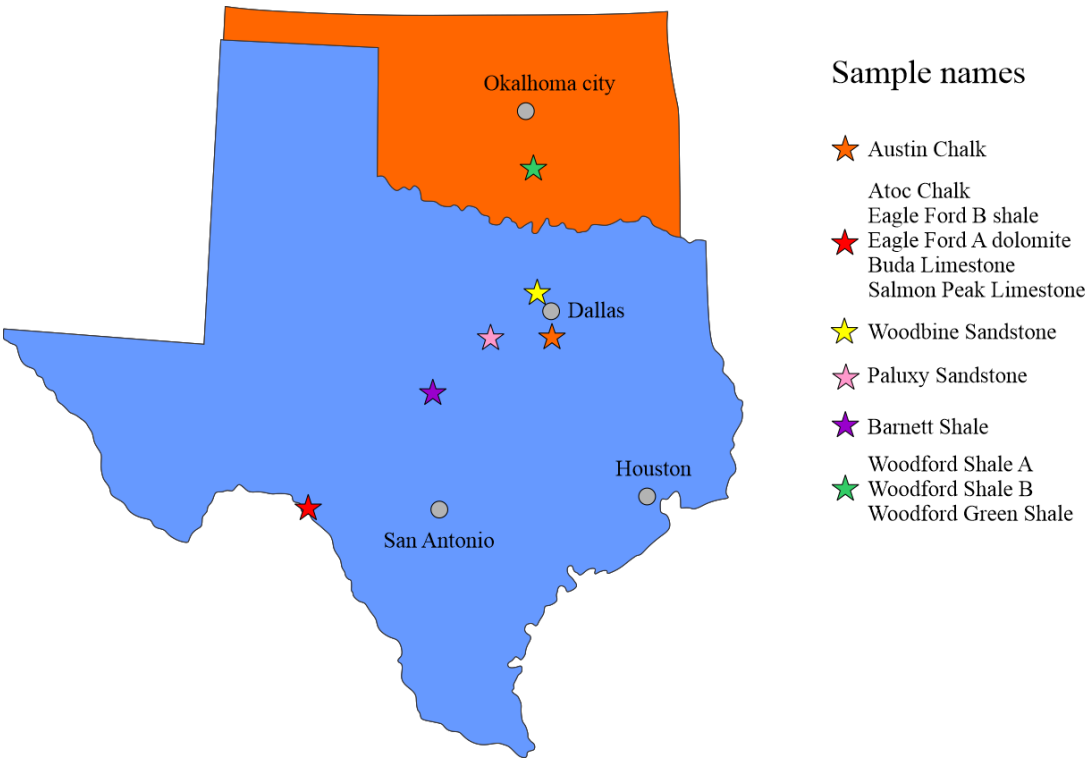

Figure 1. Sampling locations.

Table 1. Mineral compositions (wt.%) of twelve rock samples.

Sample ID	Quartz	Orthoclase	Albite	Microcline	Calcite	Ankerite	Kutnohorite	Dolomite	Pyrite	Magnetite	Goethite	Fluorapatite	Clays
Austin Chalk	1.2				96.3		0.5						2
Atco Chalk	1				99								
Eagle Ford B shale	15.5				79.6	1.2			0.8				2.9
Eagle Ford A dolomite	9.8				0.7	44.8	36.5			0.2	2		6
Buda Limestone	1.3				98.7								
Salmon Peak Limestone	0.2				99.8								
Woodbine Sandstone	91.8										8.2		
Paluxy Sandstone	42.5					57.5							
Barnett Shale	40.7	1	1.3		2.2							13.1	41.7
Woodford Shale A	13.7			0.3				64.9	1.5				
Woodford Shale B	17.9			1.2				72.8	0.2			2.2	5.9
Woodford Green Shale	60.8			12.8					4				22.3

2.2 XRD

The rock fragments from the sample cutting were pulverized to be less than 200 mesh to conduct XRD on the MAXima X XRD-7000 with the scanning range of 2 to 70 degree. Mineral compositions were calculated with Jade 9 software.

2.3 Water immersion porosimetry

The self-designed water immersion porosimentry was used to determine the edge-accessible bulk density, grain density, and porosity of porous materials at sample sizes from ~2 mm to 10 cm in dimensions. The detailed test procedure follows Wang et al. (2021c). Three $1cm^3$ cubes of each sample were tested to decrease the uncertainty from possible sample heterogeneity.

2.4 Mercury intrusion porosimetry

A Micromeritics AutoPore 9520 mercury intrusion porosimetry was used to analyze a series of petrophysical properties such as porosity, pore-throat size distribution, pore-volume, surface area, capillary pressure, permeability, and tortuosity (Hu et al., 2017). Tests were conducted from 0.5 (or 5, depending on sample porosity) to 60,000 psi and the equilibration time at each pressure point was 30 seconds. A starting pressure for filling mercury to surround the samples which porosity lower than 10% was set to be 5 psi to avoid the conformance effect, and for sample porosity higher than 10% at 0.5 psi to capture the information of μm-sized pores within the samples. The contact angle of mercury to sample (140° for inorganic rock; 152.45° for organic-rich shale) and surface tension of mercury (485 dyne/cm for inorganic rock; 475 dyne/cm for organic shale) (Wang et al., 2016) were used to calculate pore-throat size distribution. Following Katz and Thompson (1986; 1987) and Gao and Hu (2013), both permeability and tortuosity can be calculated accordingly.

2.5 Contact Angle

As a quick wettability assessment approach, a contact angle measurement has been widely used to determine the wettability of a solid surface towards fluid(s). In this study, Ramé-hart Model 250 Tensiometer was used for contact angle measurement, with deionized water representing the hydrophilic fluid. Oven-dried thin slabs at 1 cm×1 cm×0.3 cm were used in the air-liquid contact angle test. Thin slabs were first polished by 180, 400, and 800 grit sandpapers to reduce the surface roughness. For each test, one thin slab was placed onto an adjustable platform. A droplet of water was released onto the surface and built-in instrumental software was used to capture the spreading behavior of droplets and generate contact angle results.

2.6 Spontaneous water imbibition and water vapor sorption

For the water imbibition tests, samples were cut into two cubes. Except for the top and the bottom sides, all other surfaces were covered with a quick-cure epoxy. The coated samples were placed into the 60°C ovens for 48 hr to remove the moisture in the connected pore space. Then the samples were taken out of the oven and immediately placed into a desiccator to be cooled to room temperature. The sample, holder, balance, and fluid dish were assembled as shown in Fig. 2. The balance used was Radwag AS 60/220.R2 with a readability of 0.00001 g. Once the sample touched the surface of water, the balance readings were automatically recorded for a duration of 24 hr.

The water vapor sorption tests were conducted in the same experimental set as the imbibition except that the sample bottom did not contact water and the tests ran for a longer duration (72 hr). The water vapor which evaporates from the fluid reservoir will penetrate the rock matrix through vapor transport and capillary condensation into the pore spaces of these natural rocks (Hu et al., 2001; Cihan et al., 2019). This test can monitor the water vapor sorption vs. time at a

high relative humidity which can be used to investigate the dynamic behavior of wetting-gas phase diffusion and capillary condensation in porous media.

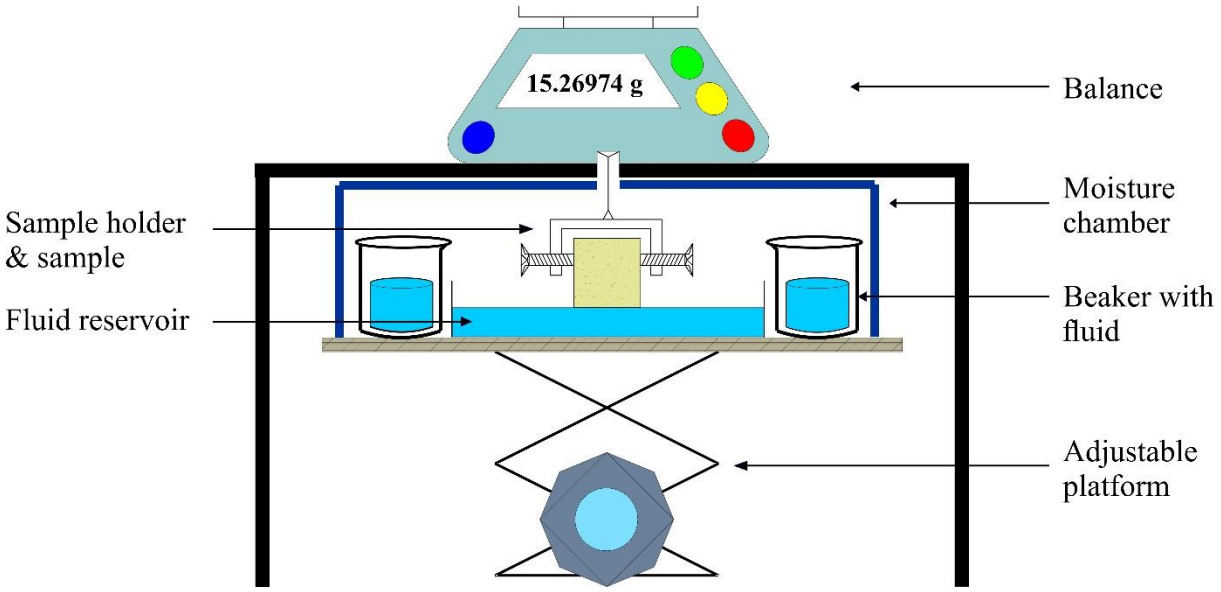

Figure 2. Illustration of spontaneous imbibition setup (Wang et al., 2021c).

3. Background of water imbibition and vapor sorption

In this study, we employ Handy's imbibition model for liquid imbibition with negligible contribution of gravitational force:

$$Q_w^2 = \left(\frac{2P_c k_w \emptyset A^2 S_w}{\mu_w}\right)t \quad (1)$$

where Q_w is the total volume of water imbibed in cm^3; P_c is capillary pressure in Pascal; k_w is the effective permeability of the porous medium to a wetting fluid in cm^2; A is the imbibition cross-sectional area in cm^2; S_w is water saturation, %; μ_w is fluid viscosity, Pascal-second; $\emptyset$ is sample porosity, and t is imbibition time in second.

The spontaneous imbibition is mathematically analogous to diffusion as the molecules navigate through the tortuous and connected pore space in porous media, the wetting front distance (l)

from the bottom shows a linear relationship to the square root of time ($t^{0.5}$) (Hu et al., 2012). Therefore, when being interpreted at the log-log scale, $\log_I = 0.5\log_t$. The slope of the log-log equation is called the imbibition slope and can reflect the pore connectivity (Hu et al., 2015). According to Hu et al. (2012), imbibition slope> 0.5 indicates good pore connectivity. An imbibition slope smaller than 0.5 but larger than 0.26 indicates intermediate pore connectivity, whereas an imbibition slope smaller than 0.26 means poor pore connectivity of the porous media towards the imbibing fluid.

Water vapor sorption is a lumped term for diffusion, adsorption, and capillary condensation of water vapor into a partially saturated porous media. Due to those three processes leading to the water uptake in various levels of relative humidity, a single-equation model is not available to describe the water vapor sorption. Vincent et al. (2017) and Cihan et al. (2019) indicate that the transition of diffusion-adsorption-capillary condensation could be investigated with experiments and Hu et al. (2001; 2015) indicate the water vapor sorption can also be interpreted in the log-log scale as liquid imbibition.

4. Results

4.1 Lithology and mineral composition

According to the results of XRD, mineral compositions of 12 natural rocks are determined and presented in Table 1. Austin Chalk, Atco Chalk, Buda Limestone, and Salmon Peak Limestone contain a very high percentage of calcite (96.3 to 99.8%), whereas the Eagle Ford A dolomite, Woodford Shale A, and Woodford Shale B possess a high percentage of dolomite-group minerals (64.9 to 81.3%) such as ankerite (Fe-dolomite), kutnohorite (Mn-dolomite), and dolomite. Eagle Ford B Shale has a high calcite content which is followed by quartz. Barnett

Shale, which is siliceous mineral rich, it Eagle Ford Shale contains 15.5% of quartz and ~80% of calcite. The Woodbine and Paluxy Sandstones are quartz-rich; however, the Paluxy Sandstone has more than half of the ankerite. In addition, fine-grained Woodford Green Shale only contains siliceous components such as quartz, microcline, clay minerals and pyrite.

4.2 Pore structure

To investigate the pore structure of these 12 samples, both WIP and MIP analyses were used in this study to assess the sample edge-accessible pore space for water and mercury. Capable of accommodating a wide range of sample sizes, WIP can analyze the porosity and densities for a batch of samples in two days. MIP tests were conducted according to the porosity measured by the WIP and offer more detailed pore structure information such as porosity, surface area, permeability, tortuosity, and pore-throat size distributions. Table 2 shows that the edge-accessible porosity of all 12 samples measured by WIP varies from 1.64 to 32.33%, which also agrees with the porosity derived from MIP technique (Table 3). In addition, MIP-derived surface area ranges from 0.16 to 37.33 m^2/g, permeability from 0.31 to 7604.87 md, and tortuosity from 2.51 to 11.63. Fig. 3 shows the pore-throat size distribution of 12 samples. Austin Chalk, Atco Chalk, Eagle Ford A dolomite, Salmon Peak Sandstone, and Paluxy Sandstone have a dominant pore-throat diameter of 0.1-1 μm, as compared to 0.01 to 0.05 μm for the Buda Limestone. Eagle Ford B Shale, Barnett Shale, and Woodford Shale B show the appearance of pores at all and wide measurable ranges. The dominant pore-throat diameters of coarsed-grained Woodbine Sandstone are at 10-100 μm, and fine-grained Woodford Shale A and Woodford Green Shale mostly at less than 0.01μm.

Table 2 Results of water immersion porosimetry and contact angle tests.

Sample ID	Porosity (%)	Bulk density (g/cm^3)	Grain density (g/cm^3)	Water-air contact angle (°)	Wettability to water
Austin Chalk	29.12	1.91	2.70	43.6	Intermediately
Atco Chalk	7.38	2.49	2.69	83.4	Slightly
Eagle Ford B shale	1.64	2.39	2.43	87.8	Slightly
Eagle Ford A dolomite	15.49	2.34	2.77	15.1	Strongly
Buda Limestone	3.47	2.60	2.70	55.1	Intermediately
Salmon Peak Limestone	7.74	2.49	2.70	45.4	Intermediately
Woodbine Sandstone	32.33	1.84	2.72	0	Strongly
Paluxy Sandstone	10.81	2.46	2.73	85.1	Slightly
Barnett Shale	13.47	1.87	2.16	80.2	Slightly
Woodford Shale A	2.63	2.51	2.58	78.5	Slightly
Woodford Shale B	7.96	2.34	2.55	88.3	Slightly
Woodford Green Shale	24.37	2.03	2.68	28.8	Strongly

Table 3. Pore structure information determined by MIP.

Sample ID	Pressure range (psi)	Porosity (%)	MIP/WIP porosity ratio	Average pore-throat diameter (nm)	Surface area (m2/g)	Permeability (mD)	Tortuosity
Austin Chalk	0.5-60,000	28.8	0.988	259.2	2.8	217.7	4.2
Atco Chalk	5-60,000	6.5	0.877	102.2	1.2	0.6	3.6
Eagle Ford B shale	5-60,000	2.0	1.241	11.3	4.1	0.1	4.6
Eagle Ford A dolomite	0.5-60,000	15.4	0.993	288.7	1.1	519.3	2.5
Buda Limestone	5-60,000	3.2	0.915	28.9	2.0	8.2	3.7
Salmon Peak Limestone	5-60,000	7.6	0.985	279.4	0.5	2.5	4.3
Woodbine Sandstone	5-60,000	30.3	0.937	1321.8	0.2	7604.9	2.5
Paluxy Sandstone	0.5-60,000	9.5	0.878	178.4	1.1	540.6	3.0
Barnett Shale	0.5-60,000	13.1	0.976	17.7	18.4	287.6	4.9
Woodford Shale A	5-60,000	2.8	1.073	8.5	9.8	0.3	6.2
Woodford Shale B	5-60,000	6.5	0.813	27.0	5.7	0.6	6.5
Woodford Green Shale	0.5-60,000	21.9	0.898	12.9	37.3	36.6	11.6

Table 4. Pore connectivity results from liquid water imbibition in both P and T directions.

Sample ID	P imbibition					T imbibition				
	Slope 1	Duration	Slope 2	Duration	Connectivity	Slope 1	Duration	Slope 2	Duration	Connectivity
Austin Chalk	0.597	27 s-1.5 hr			High	0.557	1.3-52 min			High
Atco Chalk	0.305	41 s-24 hr			Intermediate	0.250	2 min-2.6 hr	0.401	2.6-24 hr	Low-intermediate
Eagle Ford B shale	0.204	5 min-24 hr			Low	0.166	2 min-24 hr			Low
Eagle Ford A dolomite	0.562	1.2-36 min			High	0.568	41 s-1 hr			High
Buda Limestone	0.457	2.3 min-24 hr			Intermediate	0.408	1.1 min-22 hr			Intermediate
Salmon Peak Limestone	0.567	10 s-26 min	0.391	26 min-12.4 hr	High to intermediate	0.368	46 s-17 hr			Intermediate
Woodbine Sandstone	1.066	16 s			High	2.190	6 s			High
Paluxy Sandstone	0.449	44 s-4.4 hr			Intermediate	0.474	44 s-4.4 hr			Intermediate
Barnett Shale	0.433	40 s-5.4 hr	0.214	5.4-24 hr	Intermediate	0.195	18 s-8.4 hr	0.330	8.4-24 hr	Low-intermediate
Woodford Shale A	0.258	10 s-15.6 hr			Low	0.202	2 min-24 hr			Low
Woodford Shale B	0.361	20 s-24 hr			Intermediate	0.248	1.5 min-24 hr			Low
Woodford Green Shale	0.430	2 min-2.7 hr	0.508	2.7-24 hr	Intermediate to high	0.301	2 min-2.7 hr	0.367	2.7-24 hr	Intermediate

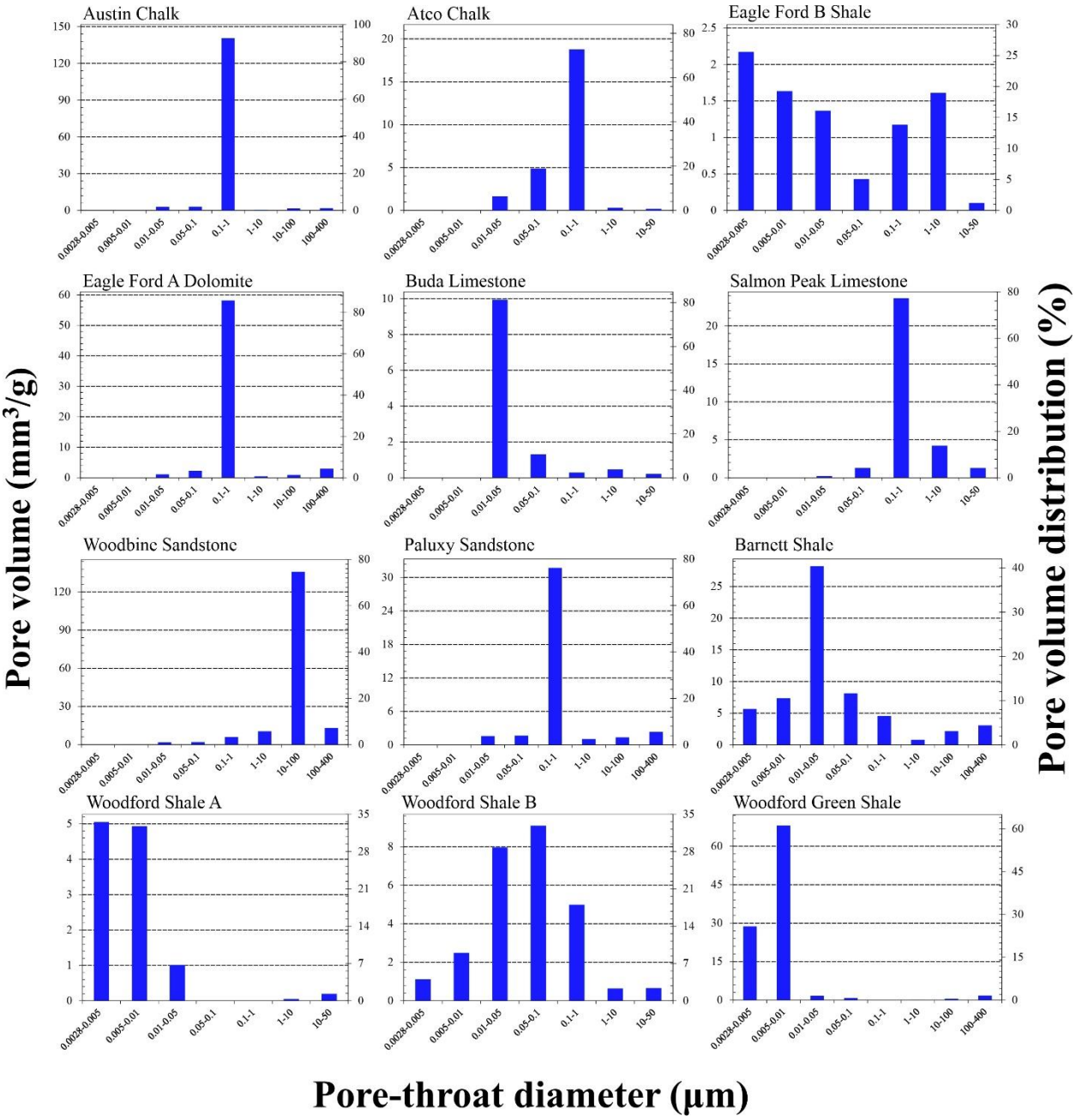

Figure 3. MIP results of pore volume and its distribution vs. pore-throat diameter.

4.3 Water-air contact angle

The contact angles of deionized water (DIW) were measured with the sessile drop contact angle method, with the results shown in Table 2. Previous contact-angle-based wettability

classification (Craig, 1971; Treiber et al., 1972) is not always suitable for classifying the wettability of natural rock, especially for shale (Wang et al., 2021c). Wang et al. (2021c) suggested a more refined wettability classification into the wetting categories using 30° and 60° as the boundaries of being strongly-, intermediately-, and slightly-wet for a single fluid. Following this wettability classicization for 12 natural rocks, the carbonate mineral-rich and inorganic rocks such as Austin Chalk, Atco Chalk, and Paluxy Sandstone are intermediately- to slightly-wet towards DIW (contact angle: 43.6° to 85.1°). Organic-rich shales such as Eagle Ford B Shale, Barnett Shale, Woodford Shale A, and Woodford Shale B are all slightly-wet to DIW (contact angle: 78.5° to 88.3°). On the other hand, Eagle Ford A dolomite, Woodbine Sandstone, and Woodford Green Shale are strongly-wet to DIW at contact angle of 0° to 28.8°.

4.4 Water imbibition and vapor sorption.

Fig. 4 shows the cumulative water content gain per gram of rock sample. The imbibition curves conducted with the imbibition direction at P and T directions towards the bedding plane at the end of tests show three types of behaviors which are: (1) both imbibition curves have a similar shape and height (for example, Austin Chalk, Buda Limestone, Salmon Peak Limestone); (2) both imbibition curves have a similar shape but different height (for example, Eagle Ford A dolomite, and Paluxy Sandstone); (3) both curves have different shape and height (for example, Atco Chalk, Eagle Ford B Shale, Woodbine Sandstone, Barnett Shale, Woodford Shale A, Woodford Shale B, and Woodford Green Shale). According to Hu et al. (2012), the imbibition slope from the plot of log cumulative imbibition height vs. log time can reflect the pore connectivity of porous media. Therefore, the pore connectivity of 12 samples in P and T directions is calculated and shown in Table 4 and Figs. 5-6. Overall, our samples cover all of these three categories of pore connectivity. Austin Chalk, Eagle Ford A Dolomite, and Woodbine

Sandstone show a high pore connectivity in both P and T directions, and the imbibition process last from several seconds to around 1.5 hr. Atco Chalk, Paluxy Sandstone show an intermediate pore connectivity in both testing directions, and the imbibition process last 4.4 to 24 hr, whereas Eagle Ford B Shale and Woodford Shale A have a low connectivity in both directions with the imbibition process not showing a tendency of reaching the sample top at the end of experimental duration. Interestingly, Atco Chalk, Salmon Peak Limestone, Barnett Shale, and Woodford Green Shale show the changing imbibition slope with different pore connectivity in different durations, indicating the encounter of pore networks with different connectivity. For example, the Salmon Peak Limestone shows imbibition slopes of 0.567 from 10s-26 min and 0.391 from 26 min-12.4 hr in the P direction. Barnett Shale shows imbibition slopes of 0.195 from 18 s-8.4 hr and 0.330 from 8.4-24 hr. In addition, the pore connectivity of Atco Chalk, Salmon Peak Limestone, Barnett Shale, Woodford Shale B, and Woodford Green Shale has higher pore connectivity in the P direction than their respective T directions.

Water vapor sorption significantly contributes to the total water uptake in the manner of vapor diffusion, adsorption, and capillary condensation into pore spaces (Table 5). In the imbibition test, even if the sample is coated with epoxy, moistures could still be taken up from the sample top though it's loosely covered with a foil. Table 3 presents the water uptake per gram of sample from imbibition and vapor sorption tests. Comparing the water uptake by imbibition and vapor sorption at 24 hr, the vapor-sorbed water accounts for 4.7 to 65.6% of imbibed water for the same rock sample. Several work on shale (e.g., Sortore, 2017) pointed out that the cumulative imbibition height of vapor sorption is proportional to the square root of time, even if the liquid imbibition results do not exhibit such a behavior. Therefore, on a log-log scale, the slope of vapor sorption can be calculated. Due to the different water uptake mechanisms of imbibition

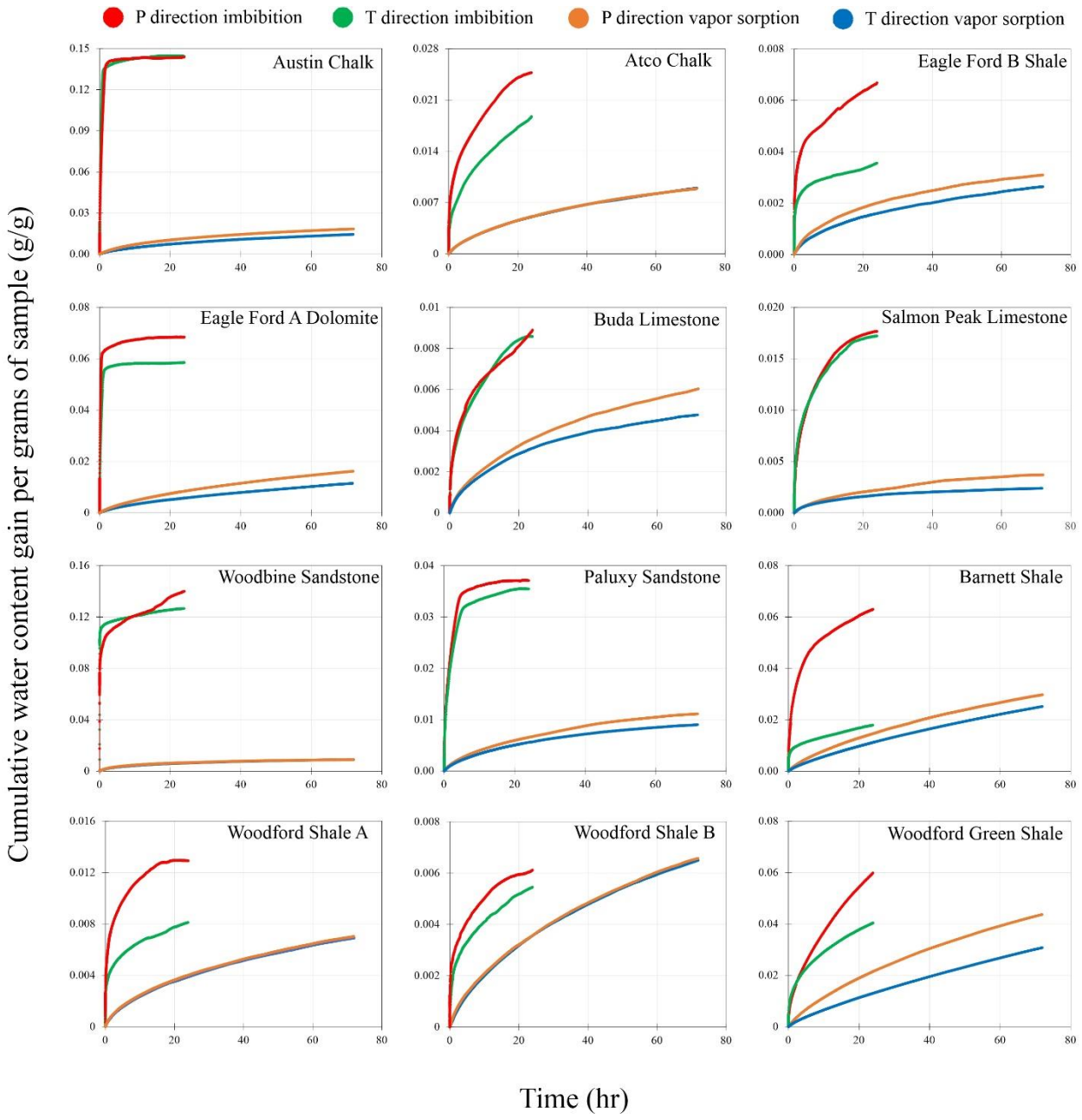

Figure 4. Spontaneous imbibition and vapor sorption data of T and P directions.

and vapor sorption, the slope of vapor sorption cannot be used to determine the pore connectivity. It, however, can be used to determine the water uptake process of vapor sorption which will be discussed in the later section.

Table 5. Weight gain rates (gram water/gram sample) after imbibition and vapor sorption tests at both P and T testing directions.

Sample ID	Water uptake per gram of sample after imbibition and vapor sorption (g/g)			Vapor-sorbed/imbibed water at 24 hr	Water uptake per gram of sample after imbibition and vapor sorption (g/g)			Imbibed /vapor-sorbed water at 24 hr
	P imbibition (24 hr)	P vapor sorption (24 hr)	P vapor sorption (72 hr)		T imbibition (24 hr)	T vapor sorption (24 hr)	T vapor sorption (72 hr)	
Austin Chalk	0.144	0.008	0.014	5.6%	0.144	0.011	0.018	7.8%
Atco Chalk	0.025	0.005	0.009	20.6%	0.019	0.005	0.009	26.9%
Eagle Ford B shale	0.007	0.002	0.003	23.9%	0.004	0.002	0.003	56.4%
Eagle Ford A dolomite	0.068	0.008	0.016	12.3%	0.058	0.006	0.012	9.8%
Buda Limestone	0.009	0.004	0.006	42.1%	0.009	0.003	0.005	35.5%
Salmon Peak Limestone	0.018	0.002	0.004	12.5%	0.017	0.002	0.002	10.0%
Woodbine Sandstone	0.140	0.007	0.009	4.7%	0.127	0.006	0.009	5.0%
Paluxy Sandstone	0.037	0.007	0.011	17.7%	0.035	0.006	0.009	15.8%
Barnett Shale	0.063	0.015	0.030	23.2%	0.018	0.011	0.025	62.4%
Woodford Shale A	0.013	0.004	0.007	31.1%	0.008	0.004	0.007	47.8%
Woodford Shale B	0.006	0.004	0.006	58.1%	0.005	0.004	0.007	65.5%
Woodford Green Shale	0.060	0.021	0.044	35.9%	0.040	0.013	0.031	32.3%

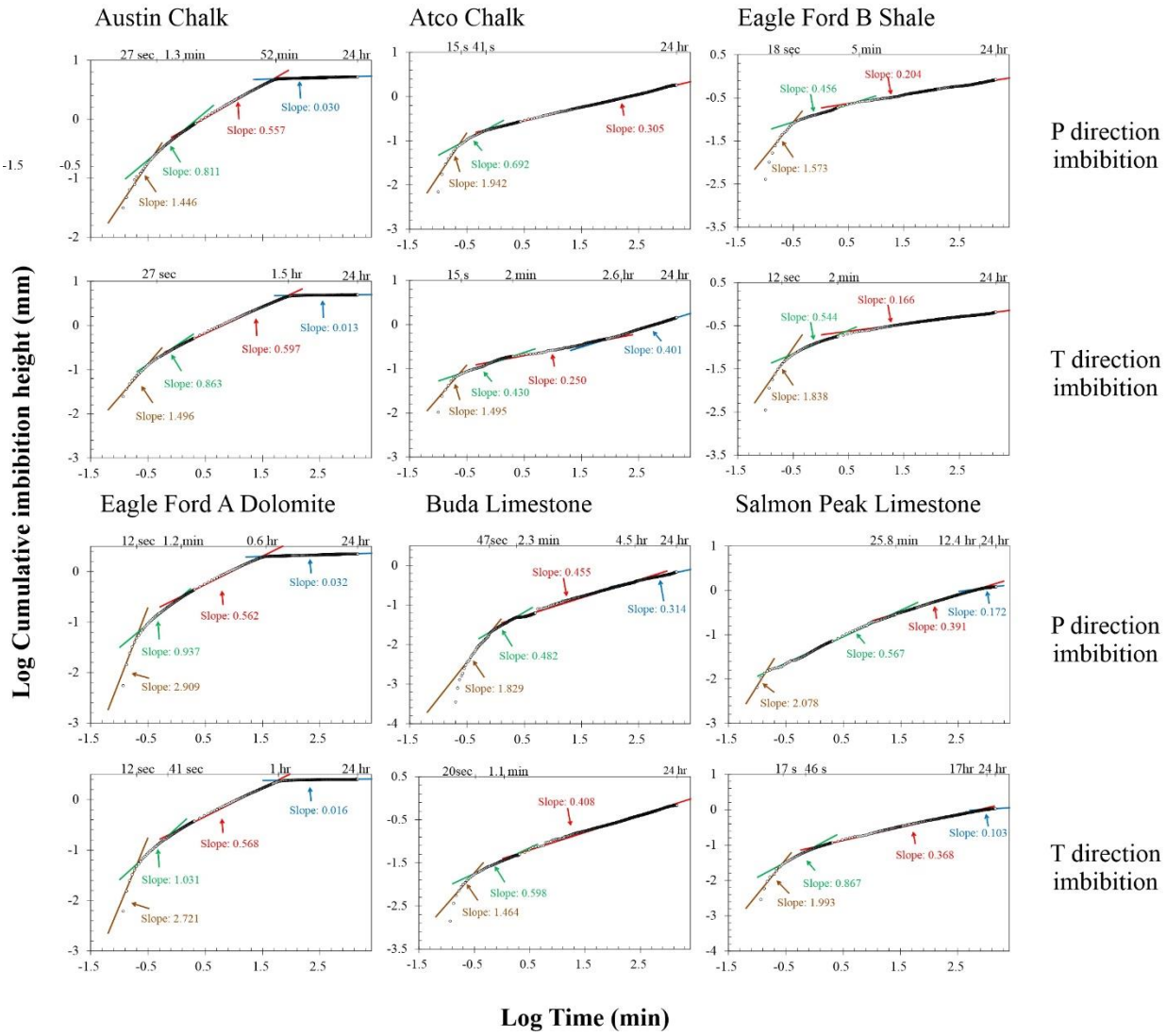

Figure 5. Log cumulative imbibition height vs. log time of water imbibition on P and T directions of six rock samples.

5. Discussion

5.1 Water spontaneous imbibition

As reported in many studies, water imbibition is capillary pressure dominated process and influenced by many factors such as porosity, pore/pore-throat diameter distribution, wettability,

mineral compositions, organic matter richness, and water-rock interactions (Singh, 2016; Yang et al., 2017; Tian, Cihan et al., 2019). In their studies, there are three factors, pore structure, wettability, and clay minerals that are often being mentioned as the most important influencing factors; those three factors are also discussed below.

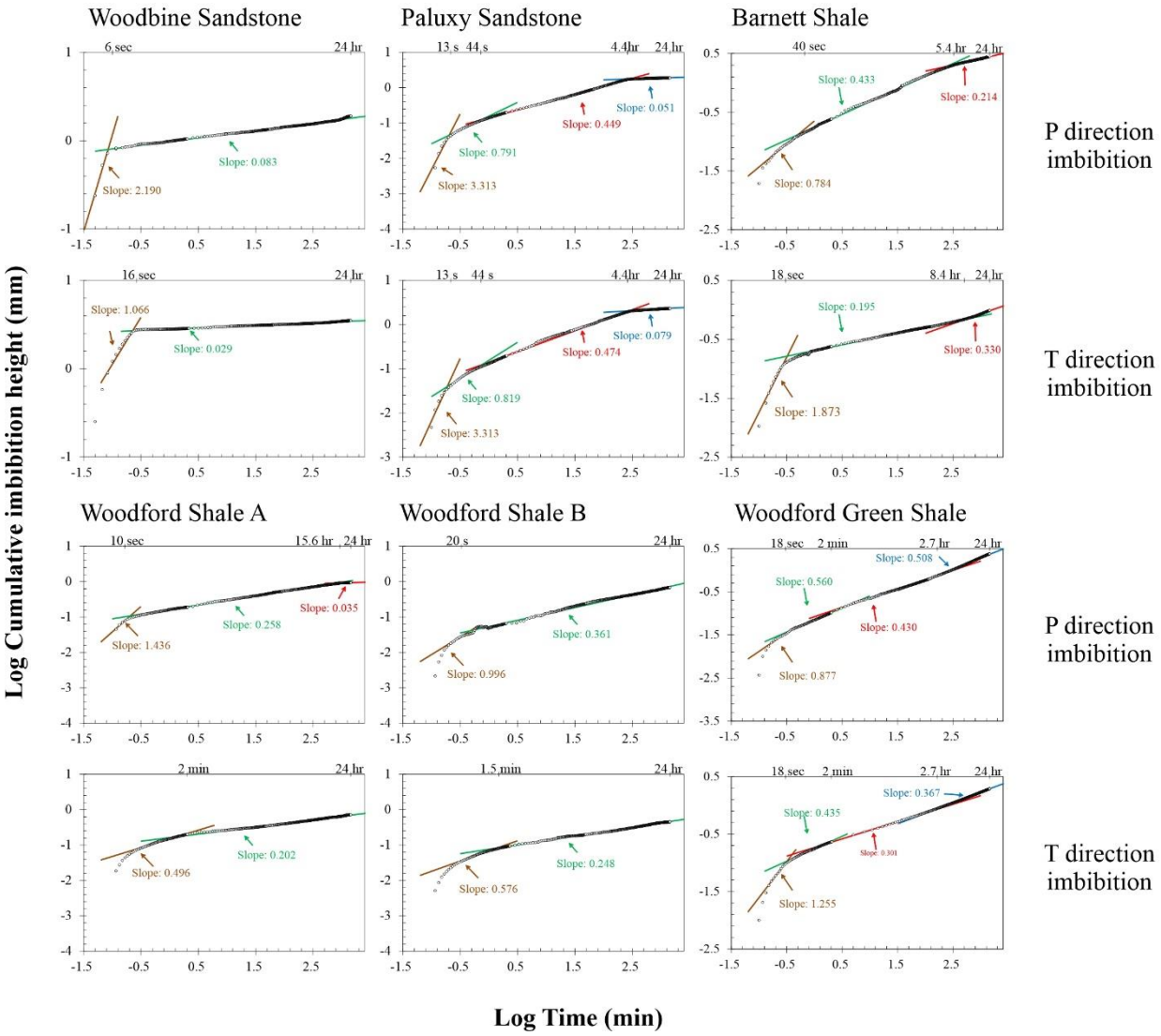

Figure 6. Log cumulative imbibition height vs. log time of water imbibition on P and T directions of six rock samples.

The pore structure is the most important factor controlling the spontaneous imbibition because it determines the critical properties of, and fluid flow pathways in, a rock. Pore structure in natural rocks especially in shale is complex. They contain pores and microfractures in various shapes, sizes, orientations, types, connectivity, and wettability (Loucks et al., 2012; 2016; Yang et al., 2019b; Zhang et al., 2020). Sandstone and carbonate rock used in this study have relatively simple pore-throat diameter distribution (with a single major peak accounting for more than 75% of total pore volume; Fig. 3), large average pore-throat diameter (28.9 to 1321.8 nm), and good porosity (3.47 to 32.33% as measured by WIP) which are favorable for water flow throughout the rock. Therefore, the pore connectivity measured from spontaneous imbibition is intermediate to high. Shale samples used in this study have complex pore-throat diameter distribution (not a major peak accounting for more than 50% of total pore volume), and small average pore-throat diameter (8.5 to 17.7 nm), and WIP-derived porosity ranging from 1.64 to 13.47%. If only looking at porosity values, some shale samples even have higher porosity than carbonate rock and they could have at least intermediate to high pore connectivity as well. For example, the porosity of Woodford Shale B is 7.98% and the imbibition slope is 0.361 in the P direction and 0.248 in the T direction, whereas the porosity of Buda Limestone is 3.47% and the imbibition slope is 0.457 in P direction and 0.408 in T direction. Previous pore structure studies of sandstone and carbonate rock by CT scanning show that most of their pores are connected and barely show vertical variation within the same lithology (Jiang et al., 2013; Feng et al., 2020). However, even though shale might have high porosity, its pores are separately connected (Hu et al., 2015; Gou et al., 2019) and are sometimes not accessible when water flow is directional; this is related to thermal maturation of OM-rich shale to alter the pore structure by forming extremely narrow pore throats that inaccessible to probing fluids at the sample surface (Hu, 2018). From

SEM observations, pores in shale samples are parallel to the laminations and do not connect to other pores in different laminations unless the presence of opened microfractures cut across laminations (Klaver et al., 2016). Barnett Shale used in this study is a good example, according to our previous studies of thin section petrography (Ning et al., 2022), there are microfractures with a μm-scaled aperture that appears along the laminations. When spontaneous imbibition is conducted in the P direction, water can flow through those fractures easily (40 sec to 5.4 hr; imbibition slope=0.433) and then gradually enter the matrix (5.4 to 24 hr). In the T direction, due to a no-presence of microfractures across the laminations, water first flows in the low connectivity matrix (18 sec to 8.4 hr), then could encounter the microfractures and the imbibition rate start to increase (8.4 to 24 hr). For the tight Woodford Shale A, the porosity is only 2.63%, its average pore-throat diameter of 8.5 nm is also the lowest among all of 12 samples. Water can only randomly flow in a very thin layer near sample surface and cannot penetrate the whole sample within the test duration, a joint effect of poor pore connectivity and wettability from its high water-air contact angle.

Many studies have reviewed the influences of wettability and clay minerals on imbibition by listing them as another two of top three important factors on spontaneous imbibition (Singh 2016; Tian et al., 2021). Indeed, in the petroleum industry, geologists and engineers need to recover more petroleum cost-effectively, and wettability plays an important role in the oil-water-rock three-phase interaction. In the water-air-rock system (not fully-saturated with a single fluid) and water-rock system (water-saturated condition), the wettability might only influence the capillary pressure according to the Washburn equation. As for water-expansive clay minerals, they play an important role in water imbibition in clayey rocks (Singh 2016). The clay hydration

could lead to better water uptake capabilities, with the osmosis effect providing an extra driving force for water imbibition (Singh, 2016; Tian et al., 2021).

Even though the water imbibition process is a lumped behavior of capillarity and relative permeability and hard to be described when the rock has a high heterogeneity. Some, and even, simplified models are useful to describe the relationship between imbibition slope and fluid flow mechanism. Liu et al. (2015) calculated that in the homogeneous and high pore connectivity porous media the imbibition process which has a slope of 0.5 obeys Darcy's law and the fluid flow is called Darcian flow. When the imbibition slope is lower than 0.5, it cannot be described by Darcy's law with the fluid flow considered as non-Darcian flow. In this study, most of our samples have an imbibition slope lower than 0.5 except for Austin Chalk, Eagle Ford A Dolomite, and Woodbine Sandstone which are high in both porosity and permeability. In Liu's interpretations, they only focused on distinguishing Darcy's flow and non-Darcy's flow but didn't pay attention to the difference between the imbibition slopes from 0.5 to 0.26 and <0.26. Hu et al. (2012) pointed out that according to the percolation theory, the wetting front is approximately one-fourth power to the time in a poorly connected system. In another word, on a log-log scale, the imbibition slope of less than 0.26 indicates pores spaces in the rock are poorly connected and the fluid will only anomalously move into a very short distance by diffusion-like imbibition. Therefore, a decreasing imbibition slope from 0.5 to 0.26 could be assumed as a transition from Darcy's flow to diffusion.

5.2 Water vapor sorption

Water vapor sorption was widely noticed in the studies of geothermal and shale reservoirs (e.g., Shang et al., 1995; Gruszkiewicz et al., 2001; Tokunaga et al., 2017; Zolfaghari et al., 2017a; 2017b). Only some of them mentioned that water vapor sorption will happen in the rock matrix

during imbibition, and water vapor diffusion, adsorption, and capillary condensation will trigger imbibition too (Hu et al., 2001; Vincent et al., 2017, Cihan et al., 2019). Vincent et al. (2017) reported that the water vapor sorption process is confined by relative humidity (RH). At low RH<0.6, moisture penetrates samples dominate by diffusion and adsorption in a diffusion-like behavior, whereas in the high relative humidity (RH>0.6) water vapor first condensate at the inlet and then move into rocks in an imbibition-like behavior. In this study, following the same experimental setup and procedure as Hu et al. (2001), the relative humidity in the chamber was measured to be above 94%. Even though the opening of the chamber and placing samples into the chamber will decrease the relative humidity, the emplacement of additional water beakers will increase the relative humidity to a high level. Therefore, the whole water vapor sorption process is assumed to happen in a high relative humidity dominated by capillary condensation with associated diffusion and adsorption processed at the beginning of water vapor sorption tests. Figs. 7-8 show the water vapor sorption behavior on a log-log scale. At the beginning of the test, the slopes of all samples are as high as 0.948 to 1.999, then gradually decrease. In these two regions, the combined effect of diffusion, adsorption, and capillary condensation makes the slope high. After several hours, the relative humidity reaches its equilibrium and the slope reaches around 0.5, whereas the slopes of Barnett Shale, Eagle Ford Dolomite, Barnett Shale, Woodford Shale B, and Woodford Green Shale still show higher slopes (0.607 to 0.802). The third imbibition slope of Austin Chalk and Woodford Shale A follows the theory and models of Vincent et al. (2017) and Cihan et al. (2019) that the capillary condensation will lead to an imbibition-like behavior. However, Eagle Ford Dolomite, Barnett Shale, Woodford Shale B, and Woodford Green Shale do not follow their predication. The reason for a higher slope (>0.5) is

probably related water vapor molecules cohesion is less than water molecules in liquid phase; the vapor molecules can move freely and sobbed by pores by different means.

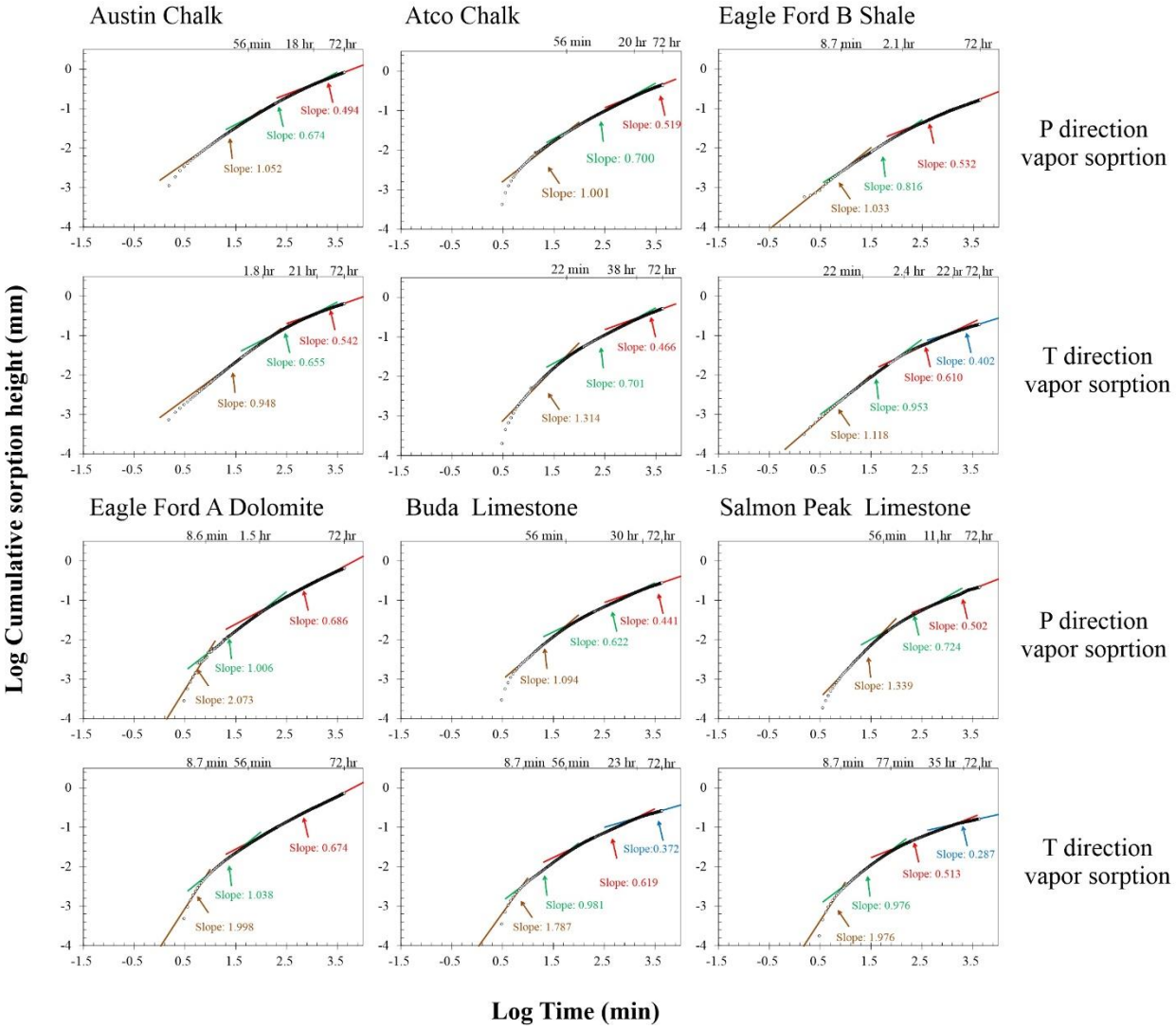

Figure 7. Log cumulative sorption height vs. log time of water vapor sorption on P and T directions of six rock samples.

Conclusions

Using water spontaneous imbibition, this work reports pore connectivity of various sedimentary rocks in the water uptake testing directions at either transverse or parallel to the bedding planes.

Austin Chalk, Eagle Ford B Shale, Eagle Ford A Dolomite, Buda Limestone, Woodbine Sandstone, Paluxy Sandstone, Woodford Shale A, and Woodford Shale B have various pore

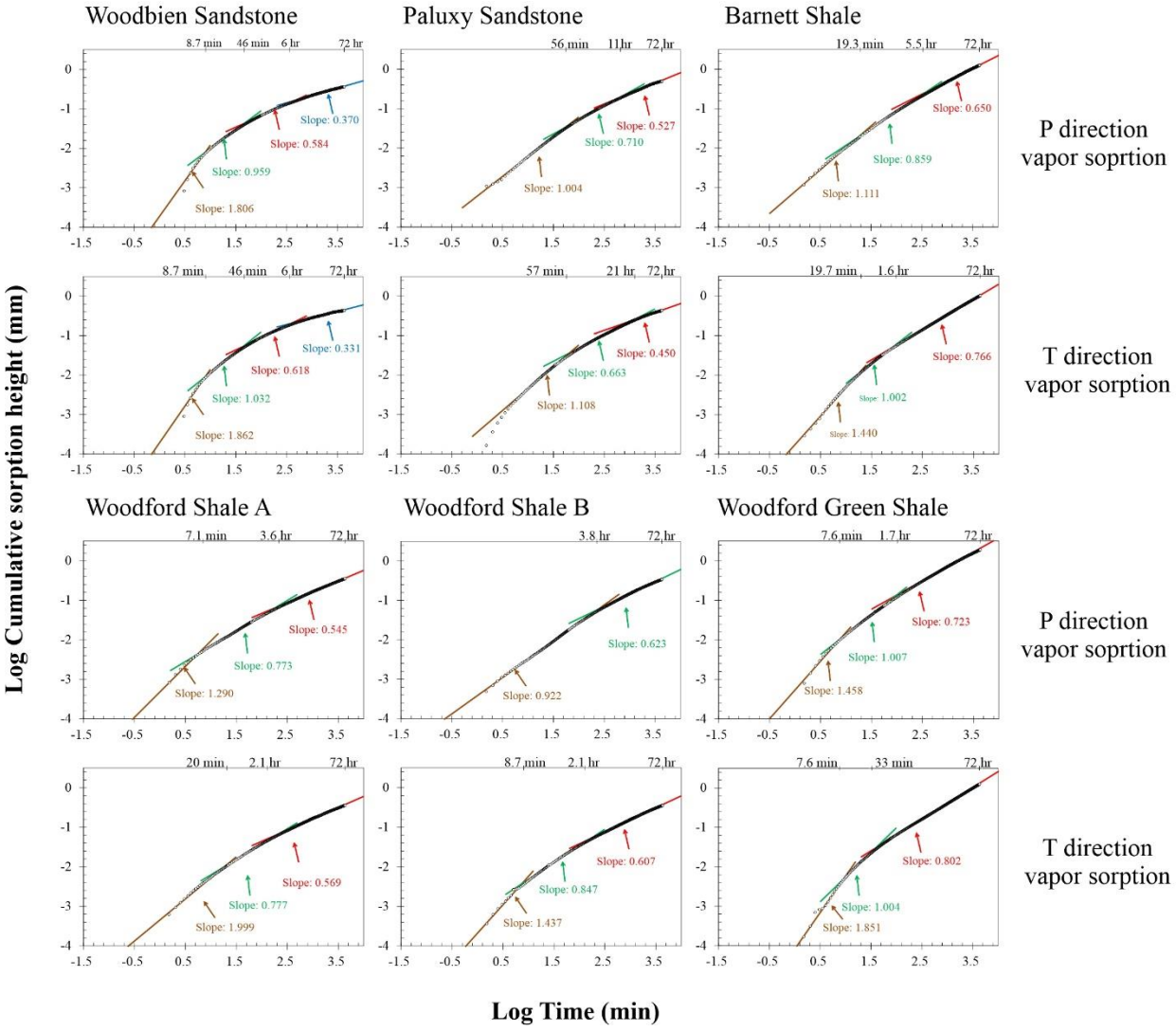

Figure 8. Log cumulative sorption height vs. log time of water vapor sorption on P and T directions of six rock samples.

connectivity from high to low, showing no pore connectivity differences in direction of parallel and transverse to the bedding plane. Atco Chalk, Salmon Peak Limestone, Barnett Shale, Woodford Shale B, and Woodford Green Shale show higher pore connectivity in the direction

parallel to the bedding plane than the transverse test. The vapor sorption in the low pore connectivity rock can contribute to a significant amount of water uptake, however, for rocks with the intermediate and high pore connectivity, it only contributes a limited amount of water uptake. Porosity, permeability, tortuosity, pore-throat size distribution, mineral composition, and wettability are determined by multiple and complementary approaches, to investigate the influence of pore structure, wettability, and clay minerals on spontaneous imbibition; the pore connectivity plays a more important role in impacting fluid flow than other factors.

Acknowledgments

We thank the financial support from the Nuclear Energy University Program managed by the Office of Nuclear Energy at U.S. Department of Energy (award number DE-NE0008797) and the AAPG Grants-in-Aid program (John H. and Colleen Silcox Named Grant in 2021).

References

Cai, J., Perfect, E., Cheng, C., Hu, X., 2014. Generalized modeling of spontaneous imbibition based on Hagen-Poiseuille flow in tortuous capillaries with variably shaped apertures. Langmuir, 30, 5142-5151.

Cant, J. L., Sitratovich, P, A., Colem J. W., Villeneuve, M. C., Kennedy, B. M., 2018. Matrix permeability of reservoir rocks, Ngatamariki geothermal field, Taupo Volcanic Zone, New Zealand. Geothermal Energy, 6, 2, 1-28.

Cihan, A., Tokunaga, T. K., Birkholzer, J. T., 2019. Adsorption and capillary condensation-induced imbibition in nanoporous media. Langmuir, 35, 9611-9621.

Craig, F. F. Jr., 1971. The reservoir engineering aspect of waterflooding. Society of Petroleum, Richardson, TX.

Dehghanpour, H., Zubair, H. A., Chhabra, A., Ullah, A., 2012. Liquid intake of organic shale. Energy & Fuels, 26, 5750-5758.

Feng, X., Zeng, J., Zhan, H., Hu, Q., Ma, Z., Feng, S., 2020. Resolution effect on image-based conventional and tight sandstone pore space reconstructions: Origins and strategies. Journal of Hydrology, 586, 124856.

Gao, Z., and Hu, Q., 2013. Estimating permeability using median pore-throat radius obtained from mercury intrusion porosimetry. Journal of Geophysics and Engineering, 10, 025014.

Gao, Z., Hu, Q., 2016. Wettability of Mississippian Barnett Shale samples at different depths: Investigations from directional spontaneous imbibition. AAPG Bulletin, 100, 1, 101-114.

Gruszkiewicz, M. S., Horita, J., Simonson, J. M., Mesmer, R. E., Hulen, J. B., 2001. Water adsorption at high temperature on core samples from the Geyser geothermal field, California, USA. Geothermics, 30, 269-302.

Hu, Q. M., Persoff, P., Wang, J. S. Y., 2001. Laboratory measurement of water imbibition into low-permeability welded tuff. Journal of Hydrology, 242, 64-78.

Hu, Q., Ewing, R. P., Dultz, S., 2012. Low pore connectivity in natural rock. Journal of Contaminant Hydrology, 133, 76-83.

Hu, Q., Ewing, R. P., Rowe, H. D., 2015. Low nanopore connectivity limits gas production in Barnett formation. Journal of Geophysical Research: Solid Earth, 120, 8073-8087.

Hu, Q., Zhang, Y., Meng, X., Li, Z., Xie, Z., Li, M., 2017. Characterization of multiple micro-nano pore networks in shale oil reservoirs of Paleogene Shahejie Formation in Dongying Sag of Bohai Bay Basin, East China. Petroleum Exploration and Development, 44(5): 720–730.

Hu, Q., 2018. Quantifying Effective Porosity of Oil and Gas Reservoirs. AAPG Search and Discovery Article #70376, 5 pages. DOI:10.1306/70376Hu2018.

Hu, Q., Quintero, R. P., El-Sobky, H., Kang, J., Zhang, T., 2020. Coupled nano-petrophysical and organic-geochemical study of the Wolfberry Plan in Howard County, Texas U.S.A. Marine and Petroleum Geology, 122, 104663.

Hu, Q., Wang, J. S. Y., 2003. Aqueous-phase diffusion in unsaturated geologic media: A review. Critical Review in Environmental Science and Technology, 33, 3, 275-297.

Jiang, Z., van Dijke, M. I. J., Geiger, S., Kronbauer, D., Mantovani, I., Fernandes, C. P., 2013. Impact of the spatial correlation of microporosity on fluid flow in carbonate rocks. Proceedings of

the SPE Reservoir Characterization and Simulation Conference and Exhibition, Abu Dhabi, UAE, September 16-18, paper number: SPE 166001

Katz, A. J., Thompson, A. H., 1986. Quantitative predication of permeability in porous rock. Physical Review B: Condensed Matter and Materials Physics, 34, 11, 8179-8181.

Katz, A. J., Thompson, A. H. 1987. Prediction of rock electrical conductivity from mercury injection measurements. Journal of Geophysical Research, 92, B1, 599-607.

Kibria, M. G., Hu, Q., Liu, H., Zhang, Y., Kang, J., 2018. Pore structure, wettability, and spontaneous imbibition of Woodford Shale, Permian Basin, West Texas. Marine and Petroleum Geology, 91, 735-748.

Klaver, J., Desbois, G., Littke, R., Urai, J. L., 2016. BIB-SEM pore characterization of mature and post mature Posidonia Shale samples from the Hils area, Germany. International Journal of Coal Geology, 158, 78-89.

Lai J., Wang, G., Wang, Z., Chen, J., Pang, X., Wang, S., Zhou, Z., He, Z., Qin, Z., Fan, X., 2018. A review on pore structure characterization in tight sandstones. Earth-Science Reviews, 177, 436-457.

Liu, H., Lai, B., Chen, J., 2015. Unconventional spontaneous imbibition into shale matrix: Theory and a methodology to determine relevant parameters. Transport in Porous Media, 111, 1, 41-57.

Loucks, R. G., Reed, R. M, Ruppel, S. C., Hammes, U., 2012. Spectrum of pore types and networks in mudrocks and a description classification for matrix-related mudrock pores. AAPG Bulletin, 96, 6, 107-1098.

Loucks, R. G., Reed, R., 2016. Natural microfractures in unconventional shale-oil and shale gas systems: Real, hypothetical, or wrongly defined? Gulf Coast Association of Geological Societies Journal, 5, 64-72.

Mazzullo, S. J., 2004. Overview of porosity evolution in carbonate reservoirs. Kansas Geological Society Bulletin, 79, 1-2, 1-19.

Moore, C. H., Druckman, Y., 1981. Burial diagenesis and porosity evolution, Upper Jurassic Smackover, Arkansas and Louisiana. AAPG Bulletin, 65, 4, 597-628.

Mostaghimi, P., Blunt, M. J., Bijeljic, B., 2013. Computations of absolute permeability on Micro-CT images. Mathematical Geosciences, 45, 103-125.

Ning, X., Ewing, R., Hu, Q., Wang, Q., Zhang, X., 2022. A new model for simulating the imbibition of a wetting-phase fluid in a matrix-fracture dual connectivity system. Geofluids, 2022, 7408123.

Pan, Z., Ma, Y., Connell, L. D., Down, D. I., Camilleri, M., 2015. Measuring anisotropic permeability using a cubic shale sample in a triaxial cell. Journal of Natural Gas Science and Engineering, 26, 336-344.

Seyyedi, M., Mahmud, H. K. B., Berrall, M., Giwelli, A., Esteban, L., Ghasemiziarani, M., Clennell, B., 2020. Pore structure changes occur during CO_2 injection into carbonate reservoirs. Scientific Reports, 10, 3624.

Singh, H., 2016. A critical review of water uptake by shales. Journal of Natural Gas Science and Engineering, 34, 751-766.

Shang, S., Horne, R. N., Ramey, Jr. H. J., 1995. Water vapor adsorption on geothermal reservoir rocks. Geothermics, 24, 4, 523-540.

Stavropoulou, E., Ando, E., Tengattini, A., Briffaut, M., Dufour, F., Atkins, D., Armand, G., 2019. Liquid water uptake in unconfined Callovo Oxfordian clay-rock studied with neutron and X-ray imaging. Acta Geotechnica, 14, 19-33.

Sun, M., Zhang, L., Hu, Q., Pan, Z., Yu, B., Sun, L., Bai, L., Fu, H., Zhang, Y., Zhang, C., Cheng, G., 2019. Multiscale connectivity characterization of marine shales in southern China by fluid intrusion, small-angle neutron scattering (SANS), and FIB-SEM. Marine and Petroleum Geology, 112, 103101.

Tokunaga, T. K., Shen, W., Wan, J., Kim, Y., Cihan, A., Zhang, Y., Finsterle, S., 2017. Water saturation relations and their diffusion-limited equilibration in gas shale: Implications for gas flow in unconventional reservoirs. Water Resources Research, 53, 11, 9757-9770.

Treiber, L. E., Archer, D. L., Owens, W. W., Aune, M., 1972. A Laboratory evaluation of the wettability of fifty oil-producing reservoirs. Proceedings of the SPE annual Fall Meeting, New Orleans, LA, Oct 3-6, paper number: 3526.

Vincent, O., Marguet, B., Stroock, A. D., 2017. Imbibition triggered by capillary condensation in nanopores. Langmuir, 33, 1655-1661.

Wang, J., Jiang, F., Zhang, C., Song, Z., Mo, W., 2021a. Study on the pore structure and fractal dimension of tight sandstone in coal measures. Energy & Fuels, 35, 3887-3898.

Wang, Q., Hu, Q., Larsen, C., Zhao, C., Sun, M., Zhang, Y., Zhang, T., 2021b. Microfracture-pore structure characterization and water-rock interaction in three lithofacies of the Lower Eagle Ford Formation. Engineering Geology, 292, 106276.

Wang, Q., Hu, Q., Ning, X., Ilavsky, J., Kuzmenko, I., Tom, T., 2021c. Spatial heterogeneity analyses of pore structure and mineral composition of Barnett Shale using X-ray scattering techniques. Marine and Petroleum Geology, 134, 105354.

Wang, Q., Zhou, W., Hu, Q., Xu, H., Meendsen, F., Shu, Y., Qiao, H., 2021d. Pore geometry characteristics and fluid-rock interaction in the Haynesville Shale, East Texas, United States. Energy & Fuels, 35, 237-250.

Wang, S., Javadpour, F., Feng, Q., 2016. Confinement correction to mercury intrusion capillary pressure of shale nanopores, Scientific Reports, 6, 20160.

Yang, R., Jia, A., He, S., Hu, Q., Dong, T., Hou, Y., Yan, J., 2020. Water adsorption characteristics of organic-rich Wufeng and Longmaxi Shales, Sichuan Basin (China). Journal of Petroleum Science and Engineering, 193, 107387.

Yang, R., Jia, A., He, S., Hu, Q., Sun, M., Dong, T., Hou, Y., Zhou, S., 2021. Experimental investigation of water vapor adsorption isotherm on gas-producing Longmaxi shale: Mathematical modeling and implication for water distribution in shale reservoirs. Chemical Engineering Journal, 406, 125982.

Yang, R., Hu, Q., He, S., Hao, F., Guo, X., Yi, J., Sun, M., 2019a. Wettability and connectivity of overmature shales in the Fuling gas field, Sichuan Basin (China). AAPG Bulletin, 103, 3, 653, 689.

Yang, R., Hu, Q., Yi, J., Zhang, B., He, S., Guo, X., Hou, Y., Dong, T., 2019b. The effect of mineral composition, TOC content and pore structure on spontaneous imbibition in Lower Jurassic Dongyuemiao shale reservoirs. Marine and Petroleum Geology, 109, 268-278.

Zhang, Y., Hu, Q., Barber, T. J., Bleuel, M., Anovitz, L. M., Littrell, K., 2020. Quantifying fluid-wettability effective pore space in the Utica and Bakken oil shale formations. Geophysical Research Letters, 47, 14, e2020GL087896.

Zolfaghari, A., Dehghanpour, H., Holyk, J., 2017a. Water sorption behavior of gas shale: I. Role of clay. International Journal of Coal Geology, 179, 130-138.

Zolfaghari, A., Dehghanpour, H., Xu, M., 2017b. Water sorption behavior of gas shales: II. Pore size distribution. International Journal of Coal Geology, 179, 187-195.

CHAPTER V

CONCLUSIONS

This dissertation presents a systematic study of multi-scale and multi-approach investigations of petrophysical characterization and fluid flow of several different natural rocks. Based on the results obtained from Chapters II to IV, the following key points can be summarized:

(1) Results from Chapter II show that the microfracture-pore system controls the porosity. Pore diameter, pore-throat size, and pore shape which are determined by MIP and NP can be validated by petrographic microscopy and SEM. Microfractures are observed from both petrographic microscopy and SEM and are classified to seven categories. The mechanisms of microfracture formation are discussed. The sporadic microfractures will not significantly contribute to the fluid flow and can only be considered as a type of pores. Only when the microfractures are observed as networked ones, they might serve as high-speed pathways for fast fluid flow.

(2) Chapter III presents an application of using μ-XRF and (U)SAXS to investigate the areal heterogeneity of pore structure, mineral composition, and sedimentary textures in a dm-sized outcrop Eagle Ford Shale sample. The sedimentary textures which cannot be observed by naked eyes can be mapped out with μ-XRF, and the porosity between different laminations can be investigated and quantified by (U)SAXS. In the dm-scale, the porosity in this sample is directly related to mineral composition.

(3) In Chapter IV, the MIP method determines the major pore-throat diameter of sandstone, carbonate rocks, and shale ranges from tens μm to several nm. Based on the results of spontaneous water imbibition the pore connectivity of various natural are determine ranges from high pore connectivity to low pore connectivity. In the direction of parallel and transverse to the

bedding plane, the pore connectivity can vary from intermediate pore connectivity to low pore connectivity and high pore connectivity pore connectivity to intermediate pore connectivity. According to vapor sorption tests, the results indicate that water vapor significantly contribute to water uptake in low pore connectivity as high as 65.6%. Discussed with the result of MIP, contact angle, and XRD, the pore structure, wettability, and mineral compositions are found to jointly contribute to the fluid flow. However, pore connectivity is the most important influencing factor that controls the fluid flow.

Overall, the comprehensive studies of this dissertation showcase a series of methods such as MIP, WIP, (U)SAXS, and NP to investigate the pore structure. Both SP and WVP were used to investigate the fluid flow and water-rock interaction. Associated with XRD, WAXS, TOC, pyrolysis petrophysical microscopy, SEM, and μ-XRF techniques, the influencing factors of pore structure and fluid flow such as mineral composition, organic richness, organic matter maturity, pore types, and sedimentary textures are illustrated for these natural rocks.

Biographical Information

Qiming Wang is from Qianjiang, Hubei, China and entered the Yangtze University (YU) in 2012 as a BS student majoring in the petroleum geology. After two and half years at Yangtze University, he transferred to the Missouri University of Science and Technology (MST). After another two and half years majoring in geology & geophysics, he received Bachelor of Science from MST and Bachelor of Engineering from YU. In 2017, he joined the University of Texas at Arlington as a master's student majoring in geosciences and became a Ph.D. student in 2019 with a major in earth and environmental sciences. His research focuses on microfracture-pore structure characterization and fluid flow in natural rocks, with a range of complementary and integrated methods.